LBL--26101

DE89 003038

Beta-Delayed Proton Emission in Neutron-Deficient Lanthanide Isotopes.

by

Phillip Alan Wilmarth

Ph.D. Thesis

(September 30, 1988)

Department of Chemistry
University of California, Berkeley
and
Nuclear Science Division
Lawrence Berkeley Laboratory
1 Cyclotron Road
Berkeley, CA 94720

This work was supported by the Director, Office of Energy Research, Division of Nuclear Physics of the Office of High Energy and Nuclear Physics of the U.S. Department of Energy under Contract No. DE-AC03-76SF00098.

Beta-Delayed Proton Emission in Neutron-Deficient Lanthanide Isotopes

Phillip Alan Wilmarth

ABSTRACT

Forty-two β-delayed proton precursors with $56 \leq Z \leq 71$ and $63 \leq N \leq 83$ were produced in heavy-ion reactions at the Lawrence Berkeley Laboratory SuperHILAC and their radioactive decay properties studied at the on-line mass separation facility OASIS. Twenty-five isotopes and eight delayed proton branches were identified for the first time. Delayed proton energy spectra and proton coincident γ-ray and x-ray spectra were measured for all precursors. In a few cases, proton branching ratios were also determined. The precursor mass numbers were determined by the separator, while the proton coincident x-ray energies provided unambiguous Z identifications. The proton coincident γ-ray intensities were used to extract final state branching ratios. Proton emission from ground and isomeric states was observed in many cases. The majority of the delayed proton spectra exhibited the smooth bell-shaped distribution expected for heavy mass precursors. The experimental results were compared to statistical model calculations using standard parameter sets. Calculations using Nilsson model/RPA β-strength functions were found to reproduce the spectral shapes and branching ratios better than calculations using either constant or gross theory β-strength functions. Precursor half-life predictions from the Nilsson model/RPA β-strength functions were also in better agreement with the measured half-lives than were gross theory predictions. The ratios of positron coincident proton intensities to total proton intensities were used to determine Q_{EC}-B_p values for several precursors near N=82. The statistical model calculations were not able to reproduce the experimental results for N=81 precursors, which decay to N=82 closed shell proton emitters; instead, pronounced structure in the delayed

proton spectra of ^{147g}Dy, ^{149g}Er and ^{151g}Yb could be explained by shell model configurations of the emitting states which have strongly hindered γ-decay channels resulting in enhanced proton emission from these states. The odd-odd N=81 precursors ^{148}Ho, ^{150}Tm, and ^{152}Lu had proton branching ratios a factor of ~10 larger than predicted and the calculations did not reproduce the spectral shapes. The branching ratio discrepancies could be resolved by reducing the level densities in the emitters or by decreasing the γ widths.

ACKNOWLEDGEMENTS

This work was supported by the Director, Office of Energy Research, Division of Nuclear Physics of the Office of High Energy and Nuclear Physics of the U.S. Department of Energy under Contract No. DE-AC03-76SF00098. I would also like to acknowledge the support of the Nuclear Science Division of Lawrence Berkeley Laboratory and the Chemistry Department of the University of California at Berkeley.

This thesis is the culmination of twenty-three years of education and when it comes time to thank the people that have helped along the way, I am sure I will forget some names. So if you are reading this and notice that I forgot to mention your name, please accept my apologies and my thanks. Now I would like to thank those whose names I did remember.

I would like to thank Dr. Seaborg for giving me the opportunity to do this work and providing the inspiration to attempt a career in nuclear physics. This thesis would not have been possible without the supervision, guidance, and support of Mike Nitschke. If I know anything about nuclear physics, it has been learned from working with Mike. I would like to thank my co-workers: Kari, Rick, Bob C., Adnan, Ken, Jacob, Peter, and Wolf. Mike and the other members of the OASIS group (past and present) have made the last five or six years both productive and enjoyable. Thanks to K. Takahashi, P. Möller, and D. Schardt for making some very useful computer programs available.

The experiments performed in this thesis would not have been possible without the outstanding technical support of Leon Archambault, Al Wydler and the staff and crew of the SuperHILAC. I can hardly recall an experiment that failed from equipment failure or poor accelerator performance and the successes can be counted in Tables 4.1 and 5.1. I would also like to thank Rich, Dick, Bill, Bob B., Al G., Saburo, Matt, Pat, Ken G., Ken M., and Bob W. for making LBL an even more pleasant place to work.

I would like to thank all of the professors and teachers that have helped me to get this far. In particular, Dr Payton and Dr. Bowles at Willamette University for providing some important education outside of the classroom. Many friends have made the last fifteen or so years pass so quickly (maybe too quickly): Pat, Brian, Clyde, Ron, Roger, Mike, Chris, Allen, Bob, Adrienne, and Beth. I don't know whether I should thank you or blame you.

I should thank each and every member of my family for the support I have received over the years, but there are too many of you. The risk of forgetting someone's name is too great, so I will give all of you a collective thank-you.

Last, but definitely not least, I owe special thanks to Janis for being there for nearly all of those "memorable" graduate years. Yes, I have finally finished it. Stretch, Wilbur, Spotty, Mombo, and Puffy have also helped to make the last few years a little more fun.

This thesis was prepared on an Apple Macintosh™ computer and printed on an Apple Laserwriter™. All text and tables were generated using Microsoft Word™. The figures were created using MacDraw™ with the histograms in chapters 4, 5, and 6 first generated on a Vax™ mainframe, then captured with VersaTerm™ 4014 emulation software, and pasted into MacDraw™.

TABLE OF CONTENTS

1. INTRODUCTION

Nuclei far from stability provide stringent tests of the predictive capabilities of present nuclear structure theories. An understanding of fundamental processes such as nucleosynthesis [Tru84, Mat85] and stellar evolution requires accurate predictions of Q values, β-decay half-lives and strength functions, branching ratios, and reaction rates. The five conference proceedings [For66, CRN70, CRN76, CRN81, Tow87] dedicated to nuclei far from stability contain numerous examples of the nuclear structure information that has been learned from studies of such nuclei. The limits of particle stability beyond which nuclei become unbound with respect to proton or neutron emission are known as the the proton and neutron drip lines, respectively. There are approximately 8000 nuclei predicted to lie within the confines of these drip lines yet only about 3000 have been observed so far. Because of the repulsive Coulomb force, the proton drip line lies closer to the line of β stability than does the neutron drip line. Using fusion reactions between neutron-deficient targets and projectiles, heavier nuclei near the proton drip line can be produced in the laboratory but nuclei near the neutron drip line, due to the large neutron to proton ratios, may never be synthesized outside of stellar environments (with the exception of the lightest elements). Nuclei near the drip lines may exhibit properties not found in nuclei closer to stability such as decay modes involving particle emission.

The present investigation is concerned with nuclei in the vicinity of the proton drip line where, due to small proton binding energies, modes of radioactivity involving proton emission are observed. In an early review article [Gol66], three modes of proton emission were discussed: β-delayed proton emission, direct proton emission, and direct two proton emission. Delayed proton emission was first discovered in the early 60's [Kar63, Bar63] and the number of precursors tabulated in review articles about delayed proton emission [Har72, Kar74, Har74, Cer77] has increased steadily to nearly 100 in the most recent review [Har87]. Direct proton emission was first observed in the decay of ^{53m}Co in 1970 [Jac70, Cer70] and five additional proton decaying nuclei have been identified [Fae84, Hof84] more recently. Beta-delayed two proton emission was discovered in 1983 [Cab83, Mol87] and the search for direct two proton emission is still in progress.

Beta-delayed proton emission is a decay process that can occur when the β decay energy Q_{EC} of the parent nucleus (the precursor) exceeds the proton binding energy B_p in the β-decay daughter nucleus (the emitter). If levels are populated by β decay at an excitation energy that is greater than the proton binding energy, then it becomes energetically possible for these levels to de-excite by proton emission. The conditions necessary for delayed proton emission, namely large Q_{EC}'s and small B_p's, are characteristic of nuclei near the proton drip line. In fact, delayed proton emission is expected to be a common decay mode in nearly all nuclei near the proton drip line. Delayed proton emission provides a very sensitive signal to identify isotopes far from stability since the increasing branching ratios for proton emission and large detection efficiency for charged particles compensate for the decreasing half-lives and production cross sections. For the most neutron-deficient nuclei, data from delayed proton decay are frequently all that is known. In addition to precursor half-life determinations, delayed proton emission is a sensitive method to study the β-decay process in nuclei with large Q_{EC} values and the properties of proton emitting levels.

In light delayed proton emitters, the spacing of levels in the emitter is typically greater than the particle detector resolution and the spectrum of the delayed protons consists of resolved peaks corresponding to proton transitions from individual states in the emitter to levels in the proton decay daughter. The energies and intensities of these peaks yield direct information about the preceding β-decay process and the level structure of the emitter at high excitation energies. The partial proton width Γ_p is usually much larger than the partial γ width Γ_γ since the proton emitting levels are typically at excitation energies well above the Coulomb barrier. In precursors where $Z<N$, the superallowed Fermi transition to the isobaric analog state often dominates the proton spectrum and delayed proton branches can approach 100%. In many of these cases it has been possible to determine the isospin purity of excited levels and perform precise mass measurements using the isobaric multiplet mass formula. In some medium mass emitters ($40 \leq A \leq 100$) it has been possible to measure the lifetimes of proton emitting levels by observing K x ray intensity ratios following electron capture in coincidence with protons [Har76].

Delayed proton emitters with $Z>50$, in contrast to the lighter emitters, have level spacing -- at excitation energies sufficient for proton emission -- that are typically less than the detector resolution. The high level density and absence of a superallowed branch result in a proton energy spectrum that is no longer composed of discrete peaks but instead becomes a bell-shaped distribution and proton branches seldom exceed a few percent. The proton spectrum is composed of many unresolved transitions and contains information about the average properties of the proton emitting levels. A study of emitters with $Z>50$ should yield information about β-strength functions, γ-strength functions, and level densities at high excitation energies [Kar73, Kar74, Kar75, Jon76, Har81]. The Coulomb barriers for proton emission are often larger than Q_{EC} so Γ_γ will typically be larger than Γ_p for all proton emitting levels. Proton emission in heavy precursors is, therefore, much more sensitive to Γ_γ than in light emitters. Models of sub-barrier proton penetrability can be tested also. Since individual proton transitions cannot be resolved for heavy precursors, it may be worthwhile studying many emitters in a given region and looking for systematic trends rather than detailed studies of individual emitters. A systematic study of delayed proton emitters in the neutron-deficient lanthanides was undertaken with this goal in mind.

Neutron-deficient nuclei with $50 \leq Z \leq 71$ and $50 \leq N \leq 84$ exhibit three main decay modes: β decay, direct particle (α or proton) emission, and β-delayed particle (α or proton) emission. Beta decay (electron capture or positron emission) is the most common decay mode with Q_{EC} values around 10 MeV and half-lives on the order of a few seconds in the vicinity of the proton drip line. Although difficulties associated with small cross sections and short half-lives can be overcome with current techniques, β decays with such large Q values are quite complicated and little detailed spectroscopic information is available for the nuclei near the proton drip line. Some nuclei near Z=64 have been well studied because of the interest in the Z=64 subshell closure. The nuclei midway between the Z=50 and N=82 shells are highly deformed and a mapping of the rotational levels of even-even nuclei over a large part of this region has recently been completed [Lis85]. Also the search for superdeformation in nuclei near ^{134}Nd has focused considerable attention on the spectroscopy of high-spin states in this region [Wad87a, Bec87].

There exists an island of α emission with $52 \leq Z \leq 55$ and $54 \leq N \leq 60$ [Mac65, Kar67, Kir77, Sch79, Sch81] due to the influence of the Z=50 shell closure (and the lower Coulomb barriers). Alpha emission in nuclei with $Z \geq 60$ and $N \geq 84$, due in part to the N=82 shell closure, has been well known for many years. Direct proton emission has been observed for ^{109}I and ^{113}Cs [Fae84], and for ^{147m,g}Tm, ^{151m}Lu, and ^{150}Lu [Hof84]. A comprehensive review of direct proton emission can be found in [Hof87].

The large Q_{EC} and small B_p values near the proton drip line in this region result in many nuclei with known delayed particle branches. In addition to delayed proton emission (observed in all elements from Z=52 to Z=71) which is the subject of this thesis, delayed α emission has been observed in a study of delayed particle emission in nuclei near Z=N=50 [Tid85] where the α binding energies are low.

There is preliminary evidence [Vie88b] that delayed α emission also occurs near N=82.

Using compound nucleus reactions between neutron-deficient projectiles and targets, 42 delayed proton precursors with $56 \leq Z \leq 71$ have been produced at the On-line Apparatus for SuperHILAC Isotope Separation (OASIS) facility [Nit83a] at the Lawrence Berkeley Laboratory SuperHILAC. Because of the broad distribution of products from heavy-ion reactions and the short half-lives encountered, on-line mass separation was required (for an excellent review of mass separator studies of nuclei far from stability, see [Han79]). Of the 42 delayed proton precursors, 25 were identified for the first time and 8 new delayed proton branches were also measured. The region of the chart of the nuclides studied is shown in Fig. 1.1.

A description of the mass separator and the experimental setup is given in chapter 2. A more complete discussion of the delayed proton emission process for heavy mass precursors and of the statistical model is presented in chapter 3. The results of the measurements are presented in chapters 4 (even mass number precursors), 5 (odd mass number precursors). Conclusions from this study will be discussed in chapter 6.

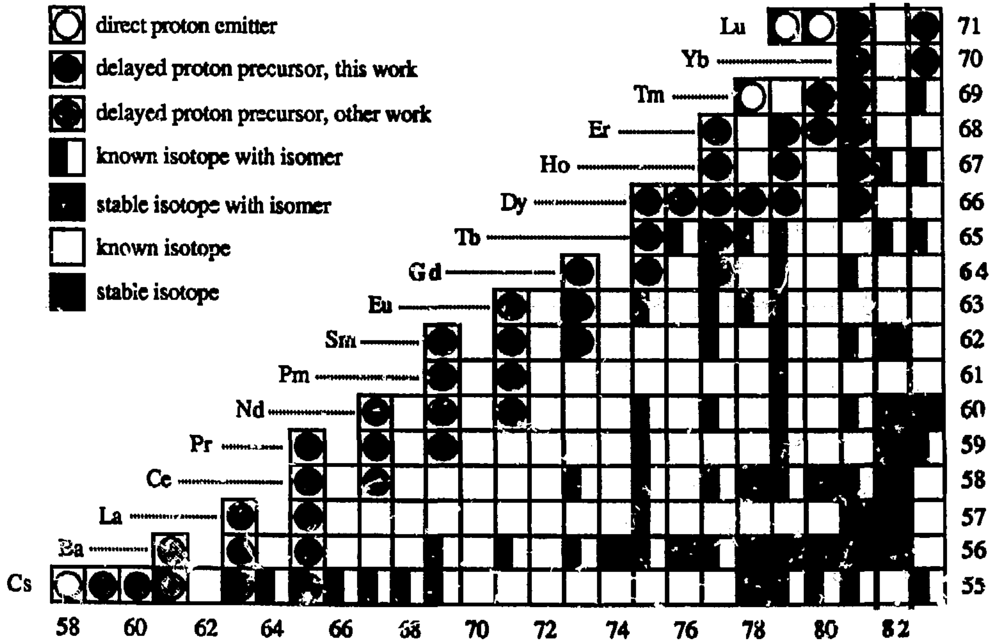

Figure 1.1. Region of the chart of the nuclides showing the delayed proton precursors produced in this study.

2. EXPERIMENTAL

2.1. INTRODUCTION

Highly neutron-deficient lanthanide isotopes were produced as evaporation residues in reactions of neutron-deficient heavy-ion projectiles (such as ^{40}Ca or ^{58}Ni) and neutron-deficient targets (such as ^{92}Mo or ^{96}Ru). The broad distribution of products from such reactions required chemical or mass separation to improve the sensitivity for detecting the isotopes of interest. The half-lives for many of the nuclei studied were a few seconds or less making chemical separations impossible. Lanthanide elements could be surface ionized with reasonable efficiencies due to their low first ionization potentials and, therefore, studied using mass separation. Because of their similar chemical properties and thus similar ionization potentials, many different lanthanide elements could be studied in the same experiment.

Using Q_{EC} and B_p values from current mass formula such as [Lir76], it was possible to predict which lanthanide isotopes may have delayed proton branches. Selection of the optimum target/projectile combinations and incident beam energies for the production of these isotopes was based on cross section calculations from [Win72]. The choices for target and projectile were based on beams that the SuperHILAC could produce with sufficient intensities and targets that could withstand these high beam intensities (up to ~200 pnA). The SuperHILAC beams which were used are summarized in Table 2.1 and the target materials (physical forms, thicknesses, purities, etc.) are listed in Table 2.2. In most experiments, an enriched molybdenum metal foil served as the target with the beam varied to produce the nuclei of interest. In certain cases, gas-cooled targets [Nit76, Mol81] of ruthenium or other materials were employed. The incident beam energy in all experiments had a center of target energy matching the calculated excitation function peak energy to optimize the production of the isotope of most interest.

2.2. THE SEPARATOR

The OASIS mass separator [Nit83a] on-line at the Lawrence Berkeley Laboratory SuperHILAC is shown schematically in the lower half of Fig. 2.1. In addition to the usual components, the OASIS beamline had a "wobbler" (a three phase motor with the beam replacing the rotor) to move the beam spot uniformly over the target surface. This allowed higher beam intensities and was crucial when using fragile targets. Located between the collimator and target was an RF pickup electrode to measure the beam intensity. The microstructure of the SuperHILAC beam induced an RF voltage in a pick-up electrode which was proportional to the beam intensity. The electrode was calibrated against a Faraday cup at least once during each experiment to avoid errors caused by the varying microstructure of the SuperHILAC beam from experiment to experiment. In many experiments, a beam intensity limiting circuit was used to prevent fluctuations in beam intensity from damaging the target thereby allowing a higher average beam intensity on target.

The separator used an integrated target/ion source combination. Surface ionization was used for all elements in the lanthanide region and a typical surface ionization source with an N_2 gas cooled target is shown in Fig. 2.2. In experiments using free standing Mo foils, no target cooling was needed and the Havar foil and cooling gas would not be present. The target was followed by two heat shields (carbon foils, ~40 $\mu g/cm^2$) and a bundle of thin-walled Ta capillary tubes (22.23 mm in length by 1.14 mm outside diameter, wall thickness of 0.076 mm). After traversing the heat shields and capillary tubes, the recoiling products entered the ion source and stopped in a suitable catcher material (usually the Ta anode endplate). The source was heated to very high temperatures near the melting point of Ta (~3000 C) by electron bombardment (EB) resulting in fast diffusion of the recoils from the catcher, short hold-up times inside the source, and high ionization efficiencies. After diffusing out of the catcher, the lanthanide atoms were surface ionized in collisions with the walls of the ion source. The capillary tubes prevented the atoms from diffusing back towards the target and getting trapped in cooler regions of the ion source, while the compound nucleus reaction recoils from the target entered the catcher/ionization region nearly unimpeded due to their small angular divergence. The coaxial construction of the ion source resulted in tight mechanical tolerances at high temperatures. All insulators in the hot sections of the source were replaced by narrow gaps of about 0.25 mm that acted as "molecular flow barriers". This enabled operation of the source at temperatures greater than 2500 C, a temperature where most insulating materials start to become conductive and break down mechanically. Typical ion sources lasted ~24 hours before most of the Ta anode (and catcher) had been evaporated due to the strong local heating caused by the EB and the stopping of the SuperHILAC beam. This would cause a noticeable drop in ion source output over a relatively short time span. A typical ion source change and minor readjustment of the ion optics required 1-2 hours. The ion source region was pumped by a baffled 250 mm, 7000 l/s diffusion pump.

After being ionized, the recoils were extracted axially and accelerated to 50 keV. An einzel lens and an electrostatic quadrupole triplet focused the ion beam onto the entrance slit of the magnetic spectrometer. The main analyzing magnet had a sector angle of 180°, a mean radius of curvature of 0.66 m, a field index of 0.5, and was typically operated at 50% of its design field. With object and image slit widths of 1.5 mm and no corrective coils on the pole faces, a mass resolution of about 880 could be obtained routinely. Located at the 135° position of the magnet were two 16° wide, wedge-shaped pole pieces to create a region of sufficiently homogeneous magnetic field to operate an NMR probe for mass measurements. A Hall probe was located next to the NMR probe to automatically tune the NMR probe as the magnetic field was changed. For an ion energy of 50 keV, masses from 45 to 380 u could be determined with a precision of ± 0.001 u from the NMR frequency and the accelerating voltage measured with a 6 1/2 digit DVM. Mass calibrations were usually accomplished by introducing a small amount of a suitable rare earth oxide directly into the ion source. This provided a stable mass marker at the desired mass number or, at worst, only a few mass units away from the desired mass. Corrections for mass defects within an isobaric chain, calculated from [Lir76], were applied in many cases. A second 250 mm, 2000 l/s diffusion pump was located at the entrance to the magnet and a small 150 l/s turbo pump was connected to a port at the 90° position of the magnet. The pressure in the separator was maintained in the 10^{-6} torr range to minimize beam losses due to scattering.

Surrounding the focal plane of the spectrometer was a detector box located 1.5 m (line of sight) from the target region; vacuum was maintained by a cryopump with speeds of 1500 l/s for air and 4000 l/s for water. Due to the high background of neutrons and γ rays from the target, only charged particle spectroscopy could be performed here. In order to detect x rays and γ rays, the radioactive products had to be transported to a lower background counting location. A suitable room was located 4 m directly above the cave. The ion beam exiting the separator was deflected 90° vertically *via* an electrostatic mirror operated at about 80% of the accelerating potential and transported to a fast-cycling tape system for collection and counting. The transfer line from the spectrometer to the tape system consisted of two electrostatic quadrupole triplets at either end of the transfer line, two (270 and 500 l/s) turbomolecular pumps to maintain high vacuum and Faraday cups at the midpoint and collection points to aid in tuning the beam optics. The counting area was shielded from the cave radiation by the 46 cm concrete roof blocks of the cave, large quantities of polyethylene for neutron thermalization located between the cave roof blocks and the mezzanine floor, 15 cm of additional concrete, and ~10 cm of lead near the detectors.

The separator was controlled by a PDP 11/10 minicomputer which monitored all important parameters. The ion source parameters (arc, electron bombardment, and filament current and voltage), accelerating potential, magnetic field (NMR and Hall probes), and vacuum gauges were all continuously monitored. Two different computer controlled stabilization modes were possible; the accelerating potential could be stabilized at 50 keV and the magnet manually tuned to the desired mass, or the accelerating potential could be varied to keep the computer calculated mass at a constant value. The two modes are called voltage stabilization and mass stabilization, respectively. The usual mode of operation was mass stabilization. Optical isolation from the separator prevented high voltage sparks from damaging the computer.

A number of significant improvements in ion source design have occurred since [Nit83a] was published. The source now uses a slit geometry for ion extraction which has improved the yield by at least 50%. Older ion source designs used a W liner to increase the surface ionization yield compared to Ta but mechanical problems at the high operating temperatures negated any increased yields. The high temperature region of the ion source is now constructed entirely of Ta and Mo components. As previously mentioned, the bundle of capillary tubes inside the ion source keeps the thermalized recoils in the high temperature region of the source after they have diffused out of the catcher, based on the principle of molecular flow restriction. This technique avoided the problems associated with a thin entrance window close to the hot ion source while allowing very low energy recoils to enter the source. However, the finite wall thickness (~0.09 mm) of the capillary tubes stops a small fraction of the recoils (and the beam) so the use of very thin walled capillary tubes (~0.045 mm wall thickness) improved the transmission from the target to the catcher in later experiments. For fragile targets which can't handle as much beam intensity or for more exotic beams which have a lower intensity, the same effective yield can be obtained with about 25% less beam current using the thinner capillaries.

2.3. THE TAPE SYSTEM

A fast-cycling tape system was located inside the shielded room above the separator (see Fig. 2.1). As stated above, this reduced the high background of fast neutrons and γ rays present near the target by several orders of magnitude. Long-lived activities, usually of little interest, were removed from the detection position simply by moving the tape, and many detectors could be placed in close geometry to the collected products (both sides of the thin tape were accessible). The mass separated products, after the ~30 μs flight time through the transfer line, were implanted directly into the tape and periodically moved inside an array of detectors.

The tape system consisted of an IBM 729 tape drive modified so that the tape ran through an evacuated detector chamber where the activity was collected and counted. The magnetic tape from the supply reel was guided through a differentially-pumped vacuum feed-through into the detector chamber. The vacuum of $\sim 10^{-6}$ torr in the detector chamber was maintained by a 500 l/s turbo pump attached to the top of the chamber. The tape from the chamber went through a second vacuum feed-through and was spooled onto the take-up reel. Magnetic computer tape with a conductivity of 1-10 KΩ per square (Scotch 700) was used to prevent electrostatic charge build-up at the collection point; the spot size of the collected activity was typically less than 6 mm in diameter. The distance from the collection point to the counting position between the detectors was 17.5 cm and the travel time, at a tape speed of 2.86 m/s, was 65 ms.

The tape movement was controlled by an Intel 8085 microprocessor. The tape usually ran in a stepping mode where the activity was collected for a fixed period of time and then moved to the detectors to be counted while the next sample was being collected. The counting intervals were selected based on the known or predicted [Tak73] half-lives of the activities of interest. The measured half-lives were obtained by resetting and starting a digital timer when the tape was advanced and time-tagging each decay event as it occurred during the counting interval. The shortest activities that could be studied were on the order of 0.1 s. In studies of short-lived isotopes where the counting interval was a few seconds or less, the tape could be automatically rewound after ~4000 advances and counting continued without intervention. The time between tape advances was quartz controlled and could be internally timed by the control computer or externally strobed. A tape positioning accuracy of ± 1 mm was possible at the fastest tape advance speeds and reduction gearing was available to produce slower tape speeds and improved positioning when necessary. The tape controller inhibited all counting during the actual tape movement plus ~10 ms settling time.

2.4. DETECTORS AND ELECTRONICS

The β-decay process of neutron-deficient lanthanides produces positrons, x rays, γ rays, conversion electrons, and delayed particles in many cases. Proton or α particles (direct or β-delayed) along with any coincident photons or positrons were of primary importance. However, singles data for the determination of absolute x-ray and γ-ray intensities in addition to βγ, γγ, and Xγ coincidence information are also required to complement the particle data. The detectors used in this study have evolved from the rather modest configuration used in the first experiments in 1983 to the current configuration described below. The three main configurations used since 1983, along with the dates each was used, are shown in Fig. 2.3. Only the present configuration will be described in detail since the others were earlier subsets. Unfortunately, conversion electron spectroscopy (a great aid in assigning γ-ray multipolarities) was not possible with any of the detector arrangements.

Facing the collection side of the tape was a three element telescope capable of detecting protons, α's, positrons, or photons. Closest to the tape was a 10.4 μm thick fully-depleted silicon transmission detector. The middle element was a 718 μm thick fully-depleted silicon detector followed by a high purity germanium (HPGe) detector. The silicon detectors were operated at room temperature and separated from the HPGe detector by a 50 μm Be window. The first two elements of the telescope detected and identified protons ($0.7 < E < 8.0$ MeV) and α's ($2.0 < E < 8.0$ MeV) using a standard particle ID formula, $PI = (\Delta E + E)^{1.73} - (E)^{1.73}$. This formula gives different values for β's, α's, and protons and the values for a given type of particle are essentially independent of particle energy. The 10.4 μm detector thickness was selected to provide a very clean separation between positrons, protons and α particles. The identification of ^{149}Er delayed protons from the background of positrons and α particles is shown in Fig. 2.4. The 718 μm detector was used with the HPGe detector as a telescope for β particles ($0.2 < E < 10.0$ MeV). The HPGe detector also measured γ rays and x rays ($5 < E < 500$ keV). The pulsed optical preamplifier signal from the HPGe was electronically split and sent to two separate amplifiers, one for β-particle detection (low gain) and one for low-energy photons (high gain). Similarly, the signal from the 718 μm detector was split into low gain for proton and α energies and high gain for β-particle energy losses ($20 \leq E \leq 2500$ keV).

A large (52% relative efficiency) n-type coaxial germanium detector faced the backside of the tape. A thin (1mm Pilot F) plastic scintillator coupled to a PMT was located directly in front of the germanium detector. The scintillator was used to detect positrons coincident with protons or, in anticoincidence, to reduce the high-energy positron background in the germanium detector, thus improving the signal to noise ratio for high-energy γ rays. The signal from the preamp of the Ge detector was split into a high gain channel for x rays ($5 < E < 250$ keV) and a low gain channel for γ rays ($50 < E < 5000$ keV).

A second n-type germanium detector (24% relative efficiency) was located about 50 mm to one side of the source at 90° to the other detectors. Photons with energies from ~100 to 2500 keV could be detected for $\gamma\gamma$ coincidence information. Table 2.3 lists the detector sizes, resolutions, etc. for the current detector configuration. The absolute efficiency curves for the three Ge detectors are shown in Fig. 2.5.

The detectors were surrounded by at least 5 cm of lead to shield against background room radiation and also to shield the detectors from the activity being collected on the tape a few centimeters below the detectors and from the previous activity present on the tape ~15 cm above the detectors. The background of α particles and delayed protons was on the order of one event per day and the coincident event rate for all combinations of pairs of germanium detectors was typically about one per second. Background lines from ^{40}K, the Th and U daughters in the lead, and some neutron capture γ rays from Ge and Al caused no difficulties in the analysis of the singles data. Energy calibrations of all germanium detectors were performed before and after each experiment using standard γ sources and the silicon detectors were calibrated with a precision pulser. This pulser was periodically calibrated using standard α sources and its long term stability was very good. Absolute detector efficiencies were determined about once per year using special thin sources attached to the computer tape and moved into the actual counting position. There were little, if any, changes in detector efficiencies with time.

Conventional fast/slow electronics, shown schematically in Fig. 2.6, were used. The fast timing signals from each detector, after going through appropriate shaping amplifiers and constant fraction descriminators, were used to generate timing information between all detectors pairs of interest. The fast timing signals were also used to define events of interest. A typical event consisted of pairwise coincidences (~2 μs overlap) between the germanium detectors (each pair was individually selectable and more than one pair could be logically combined) logically ORed with a coincidence between the 10.4 and 718 μm detectors. Each detector had an externally strobed pulser to help set up and test the coincident logic. High quality linear electronic components were used for all energy signals resulting in good resolution and stability. The detectors, detector chamber, and electronics were electrically isolated from the separator and the SuperHILAC to prevent ground loops. All preamplifier cables were run from the detectors to the main amplifiers inside a heavy copper pipe to prevent noise pickup.

2.5. DATA ACQUISITION AND REDUCTION

After appropriate amplification, the analog signals from the detectors were converted to digital information and stored as histogram and event-mode data. Multiparameter even-by-event data associated with $\beta\gamma$, Xγ, and $\gamma\gamma$ coincidences and charged particle related data were recorded in all experiments. But the importance of absolute γ-ray and x-ray intensities in level scheme construction and in proton or α particle branching ratio determinations was realized and singles data (collected as histograms) were routinely acquired after the addition of the 52% n-type Ge detector.

In the singles measurements, the tape cycle was typically split into eight equal time intervals and histograms were collected for each interval. Figure 2.7 shows an 8-s tape cycle [Fig. 2.7(a)] divided into 1-s intervals [Fig. 2.7(b)] for the singles data. Thus, half-life information in addition to intensity information was obtained. Both the singles and multiparameter data collection were interrupted during the tape movement and during the 5 ms wide SuperHILAC beam pulses [Fig. 2.7(c)]. The beam blanking was usually a few ms wider then the SuperHILAC pulses to allow for neutron thermalization and reduce the background from slow neutron capture processes. The 52% detector was connected to an 8 by 8192 channel histogramming memory. This memory was located in CAMAC, readout by a ModComp computer, and its contents saved on magnetic tape. Singles information from the x-ray region of the HPGe detector was also recorded in a multispectrum mode (8x512 channels), while the 24% detector generated a single 2048 channel spectrum. The HPGe and 24% detector were connected to multichannel analyzers which were interfaced to an Apple Macintosh personal computer for permanent storage of spectra. The acquisition hardware used in the singles measurements is shown in Fig. 2.6.

The multiparameter event-mode data were written to magnetic tape by a ModComp Classic computer using appropriate data acquisition software. The ModComp computer could be interfaced to the experiment in two ways, using an

LBL multiplexer/ADC combination (32 parameters per event maximum) or *via* CAMAC. For the earlier experiments reported here, the multiplexer/ADC was used but the quality of the system for high resolution data needed in γ-ray spectroscopy was not adequate so a transition to CAMAC was made. A simplified version of the CAMAC system is shown in the lower part of Fig. 2.6. About 20 parameters were recorded for each event. There were typically 4 high resolution (13 bit) ADCs for the x-ray and γ-ray detectors, 5 lower resolution (11 bits) ADCs for particle data, 8 TAC signals, 3 scalers (relative lab time, half-life time tagging [Fig. 2.7(d)], and beam intensity), and a tag word to separate one event from the next. The CHAOS data acquisition software [Map79] was used until the number of parameters per event and the event rates exceeded the capabilities of this software. In experiments since January 1987, the CDAS software package [Bel86], originally developed for the HERA facility at Lawrence Berkeley Laboratory, was used during data acquisition. This software ran much faster than CHAOS but was less flexible for interactive monitoring.

After acquisition, the methods for data reduction and analysis depended on the type of data. The majority of the multiparameter data on magnetic tape was βγ and γγ coincident events with only about one in 10^4 events associated with a β-delayed proton decay. This low concentration of particle related events to other events makes a form of data reduction called filtering especially appropriate. The original data tapes were scanned for events of interest (using very general criteria) which were written to a new event tape. This new tape had only a few thousand events instead of the few million events typically recorded during an experiment. The sorting programs could analyze the highly compressed data much more quickly and many different sorts of the same data in a short period of time were possible. A Fortran program was written to filter proton or α related events from the βγ data using either a simple coincidence requirement between telescope elements or using the standard particle identification technique described above.

The large volume of βγ and γγ coincident data required a fast sorting program with space for up to about 300 spectra and the EVA software package [Bel87a] was used almost exclusively. After the histograms were generated, peak fitting was done interactively using the computer program SUSIE [Bel87b]. There were two main methods to assign the large number of unknown γ rays associated with β decay of large Q_{EC} nuclei, by grouping γ rays with similar half-lives or by x-ray coincidences (from electron capture). The multiparameter data gave both types of information whereas the time resolved singles data gave only half-life and intensity information.

The singles spectra were analyzed with a Vax version of SAMPO [Rou69], a γ-ray peak fitting program, to obtain reliable peak areas and centroids. The SAMPO program was particularly useful in resolving γ-ray multiplets often present in the singles data. The spectra were originally recorded on magnetic tape or on a floppy disc and had to be transferred to the Vaxes before they could be analyzed. A Fortran program to read magnetic tapes written by the ModComps was developed. The data on floppies were sent to the Vax *via* the file transfer program Kermit and then converted to a format that could be read by SAMPO.

Table 2.1 SuperHILAC beams used in this work.

Beam	Injector	Intensity (μA)[a]	Intensity (pnA)[b]
$^{36}Ar^{c}$	Adam	~3[d]	200
^{40}Ca	Adam	~4[d]	300
^{46}Ti	Abel	~2	150
^{52}Cr	Abel	~3[d]	150
^{54}Fe	Abel	~1	100
^{56}Fe	Abel	~3[d]	200
^{58}Ni	Abel	~4[d]	200
^{64}Zn	Abel	~2	100

[a] electrical current.
[b] particle current.
[c] isotopically enriched source.
[d] limited by target stability.

Table 2.2 Properties of targets used in this work. Target diameter was 6mm for all experiments.

Target	Thickness (mg/cm^2)	Enrichment (%)	Form	Backing
^{58}Ni	2.0	≥95	metal	HAVAR
^{93}Nb	2.0	≥95	metal	self supporting
^{92}Mo	2.0	≥95	metal	self supporting
^{94}Mo	2.0	≥95	metal	self supporting
^{96}Ru	0.6	≥95	metal	beryllium
^{96}Ru	0.8	≥95	metal	carbon
^{96}Ru	1.5	≥95	metal	HAVAR

Table 2.3 Selected properties for each of the detectors at OASIS.

Detector	Material	Diameter (mm)	Thickness (mm)	Resolution (keV)	Efficiency
ΔE_p	Si	8.0	0.0104	~50[a]	0.127[a]
E_p	Si	16.0	0.718	15[a]	0.127[a]
x ray	HPGe	36.0	12.5	0.69[b]	0.128[c]
ΔE_β	Pilot F	38.2	1.0	n.a.	0.400
γ ray (52%)	n-Ge	64.9	57.8	2.5[d]	0.230[b]
γ ray (24%)	n-Ge	51.6	55.3	2.0[d]	0.011[b]

[a] for 5.8 MeV ^{241}Am α particles.
[b] for the 122 keV ^{57}Co line.
[c] for the 59.5 keV ^{241}Am line.
[d] for the 1332 keV ^{60}Co line.

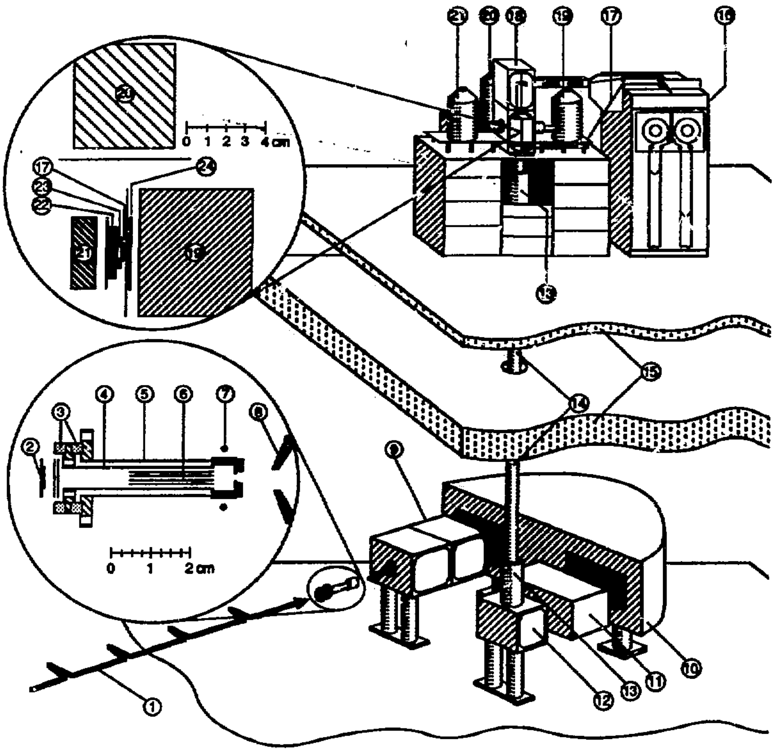

1. SuperHILAC BEAM
2. TARGET
3. INSULATORS (BeO)
4. ION SOURCE ANODE (Ta)
5. ION SOURCE CATHODE (Ta)
6. CAPILLARY TUBES (Ta)
7. EB FILAMENT (Ta)
8. EXTRACTION ELECTRODE
9. EXTRACTION AND FOCUSING
10. ANALYZING MAGNET
11. FOCAL PLANE DETECTOR BOX
12. ELECTROSTATIC MIRROR
13. ELECTROSTATIC QUADRUPOLE
14. TRANSFER LINE
15. CONCRETE SHIELDING
16. TAPE DRIVE (IBM 729)
17. MAGNETIC TAPE
18. DETECTOR BOX
19. N-TYPE Ge DETECTOR (52%)
20. N-TYPE Ge DETECTOR (24%)
21. HPGe DETECTOR
22. 718 μm Si DETECTOR
23. 10.4 μm Si DETECTOR
24. 1mm PILOT F SCINTILLATOR

Figure 2.1. Simplified representation of the OASIS mass separator online at the Lawrence Berkeley Laboratory SuperHILAC. The separator and tape system are approximately to scale. The major components are labeled.

OASIS Ion Source

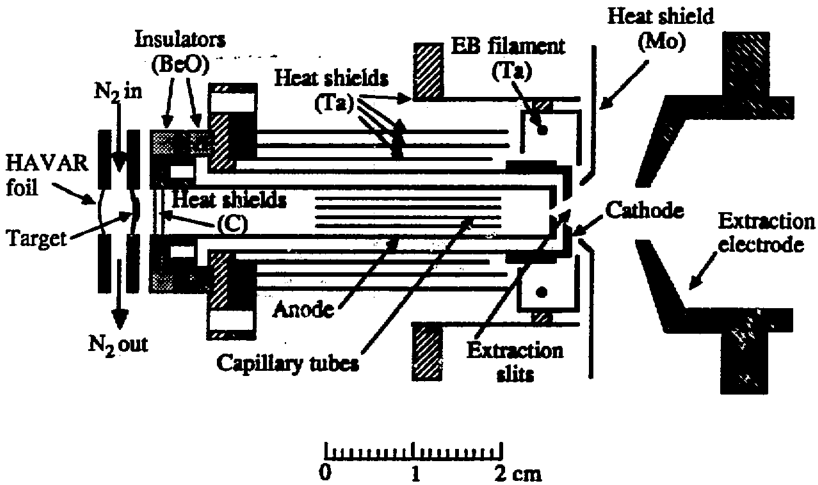

Figure 2.2. Typical OASIS surface ionization source shown with a gas cooled target.

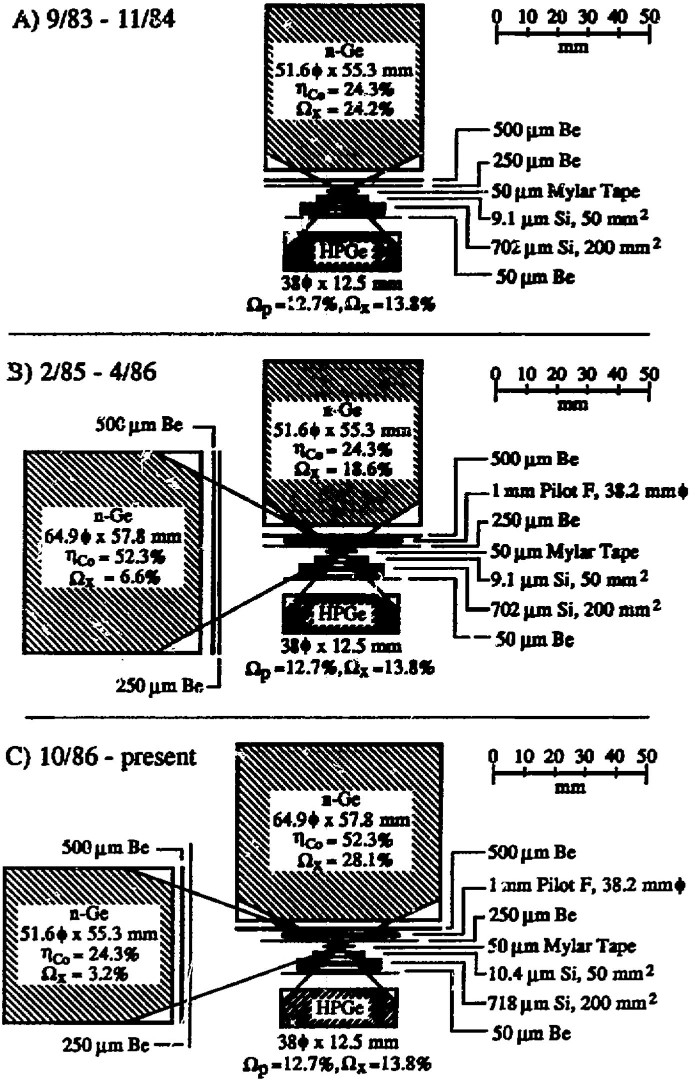

Figure 2.3. Detector configurations used at OASIS. The dates that each configuration was in use are in the upper left corners of the three drawings. The effective solid angles corresponding to the maximums in the efficiency curves are represented by solid lines from the source to the detectors.

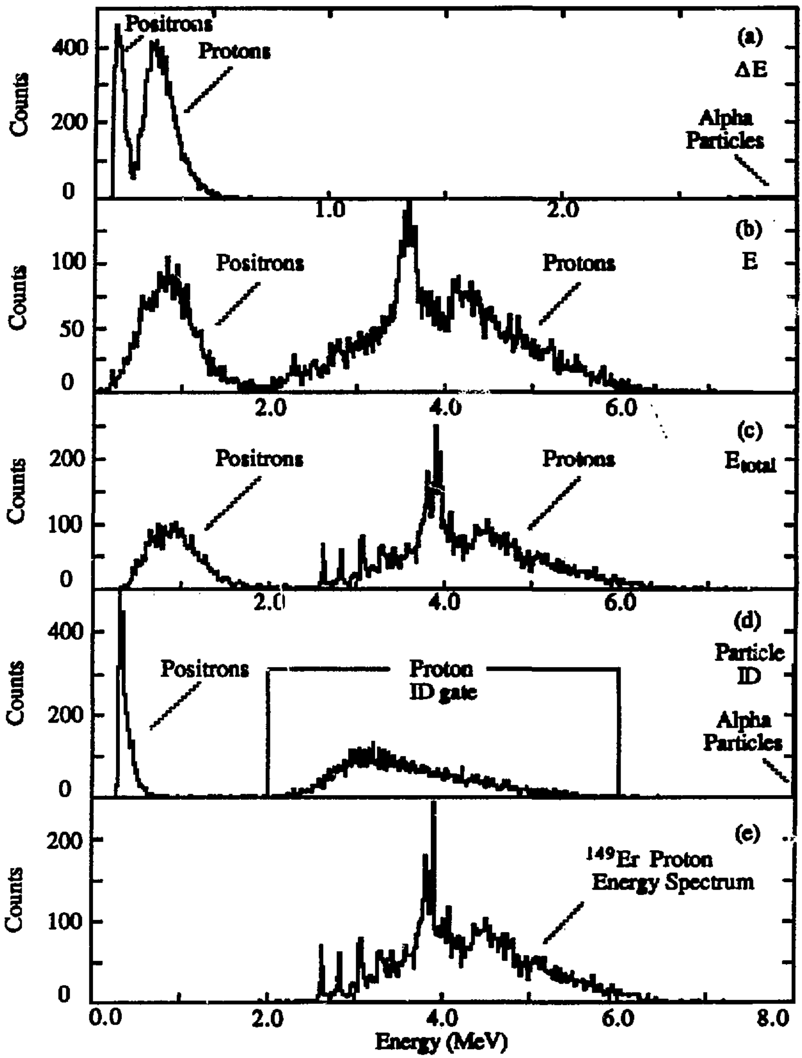

Figure 2.4. Separation of beta particles, protons, and alphas obtained using the particle telescope is shown for ^{149}Er; (a) the 13.8 μm detector spectrum, (b) the 718 μm detector spectrum, (c) sum of (a) and (b) after gain matching, (d) the particle ID distribution (alphas are off scale to the right), and (e) the spectrum from (c) subject to the proton gate shown in (d). The spectrum in (e) has a proton resolution of 35 keV. These spectra are from filtered data (see text). The positron peaks would be ~10^3 larger in the "raw" data.

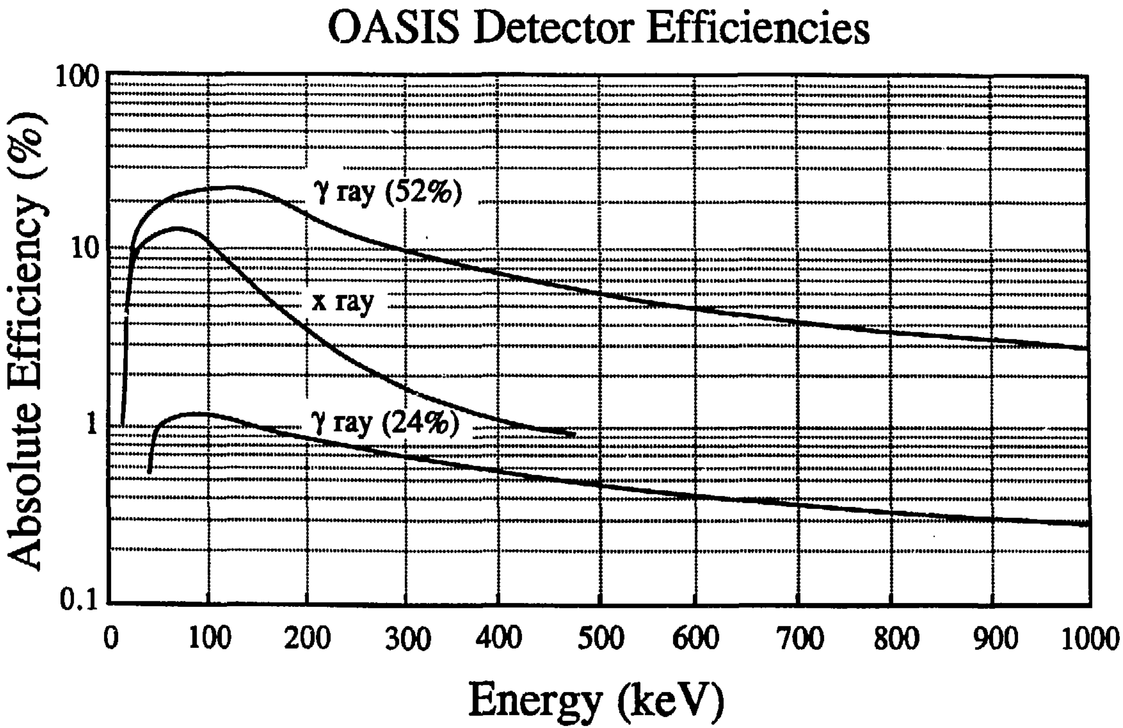

Figure 2.5. Absolute efficiency curves from 22 to 1000 keV in the current counting geometry for the three germanium detectors used in OASIS experiments.

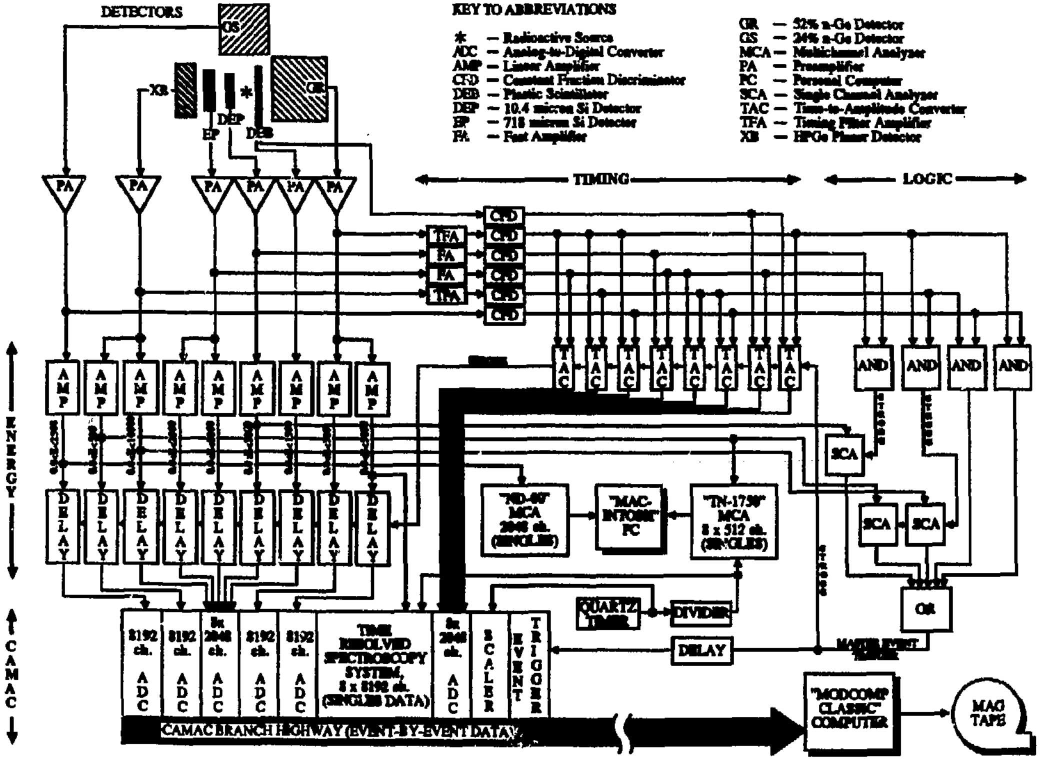

Figure 2.6. Simplified block diagram of the components for the linear, fast timing, and event definition electronics used at OASIS. The data acquisition hardware for both event-by-event and singles data is also shown.

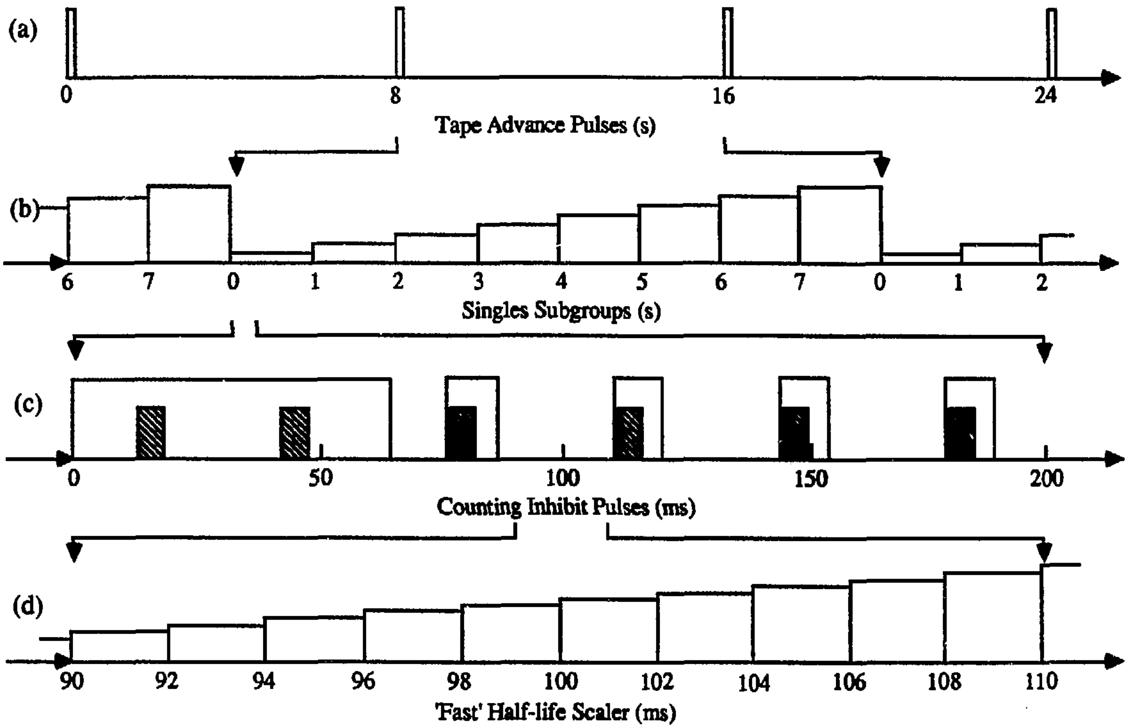

Figure 2.7. Diagram of the various counting and timing intervals used in OASIS experiments; (a) tape advance pulses for an 8-s counting interval, (b) the subgroups (typically 8) for singles data, (c) counting inhibit pulses during tape movement and during SuperHILAC beam pulses (the shaded rectangles), and (d) the scaler for time-tagging of events.

3. BETA-DELAYED PROTON EMISSION

3.1. GENERAL

The β-delayed proton emission process for a generalized heavy mass precursor is shown schematically in Fig. 3.1(a). The precursor (Z, N) must have an electron capture Q value Q_{EC} that exceeds the proton binding energy B_p in the emitter (Z-1, N+1). The precursor, with spin and parity J^π, will β decay predominantly by allowed Gamow-Teller GT transitions to levels with spin and parity $(J-1, J, J+1)^\pi$ in the emitter at an excitation energy E^*. If E^* is less than B_p, only γ-ray emission is possible, but, if E^* is larger than B_p, the level can de-excite by γ-ray or proton emission. The emitted protons may leave the daughter nucleus (Z-2, N+1) in the ground or in excited states (at an energy E_f relative to the daughter nucleus ground state, which will subsequently decay by γ-ray emission or internal conversion). For nuclei with Z~60, the Coulomb barrier for protons is around 10 MeV and the emitted protons must tunnel through this barrier. Because of the Coulomb barrier there is a threshold energy $\Theta_p=E^*-B_p$ of about 2 MeV before proton emission starts to compete with γ-ray emission. A good estimate of this threshold is when calculated values of Γ_p/Γ_γ in the emitter are greater than 10^{-4} [Nit88]. Before proton branches P_p, defined as the number of protons per β decay, are large enough to be experimentally observable, $Q_{EC}-B_p$ needs to be 1 to 2 MeV larger than Θ_p. The energetics for delayed proton decay of ^{123}Ce with Q_{EC} and B_p values from [Lir76] along with the measured proton spectrum are shown in Fig. 3.1(b).

The effects of pairing in the nucleus strongly influence the energetics for delayed proton emission. The criterion of $Q_{EC}-B_p-\Theta_p \geq 0$ MeV can be satisfied by any sufficiently neutron-deficient nucleus, be it even-even (ee), even-odd (eo), odd-even (oe), or odd-odd (oo) but the majority of known delayed proton precursors are even-odd or odd-odd. In general terms, this is easy to understand by considering Q_{EC} and B_p values for the four types of precursors as shown in Fig. 3.2. Since an even-odd precursor is the most favorable case, it will be used as a reference [Fig. 3.2(b)] with Q_{EC} and B_p, denoted by Q' and B', respectively. The minimum energy required to break a pair 2Δ is equal to about 2 MeV in this mass region, where Δ is the gap parameter ($\sim 12A^{-1/2}$ MeV). Assuming the nuclei are near each other on the mass surface, the approximate Q_{EC} values are: Q'-2Δ for an even-even precursor (a proton pair is broken) [Fig. 3.2(a)], Q' for an even-odd precursor (one proton pair broken and one neutron pair formed), Q' for an odd-even precursor (no pairs broken or formed) [Fig. 3.2(c)], and Q'+2Δ for an odd-odd precursor (one neutron pair formed) [Fig. 3.2(d)]. The proton binding energies are approximately B' for even-even or even-odd precursors (the emitter has an unpaired proton) and B'+2Δ for odd-even or odd-odd precursors (the emitter has to break a proton pair). The Q_{EC}-B_p values for even-odd or odd-odd precursors will be similar and, in general, about 2Δ larger than Q_{EC}-B_p values for neighboring even-even or odd-even precursors. Large Q_{EC}-B_p values and small B_p values favor delayed proton emission so the order from largest proton branch to smallest, for the hypothetical precursors in Fig. 3.2, would be even-odd, odd-odd, even-even, and odd-even. General features of the β-strength function discussed below also favor even-odd or odd-odd precursors. The energetics for a typical even-odd precursor ^{151}Yb and an odd-odd precursor ^{150}Tm are shown in Fig. 3.3.

In practice, the production cross sections are as important as the energetics in determining whether a given precursor can be experimentally observed. In Fig. 3.4 a region of the chart of the nuclides around ^{129}Nd is shown where each nuclide is assigned a "figure of merit" estimating the experimentally observable delayed proton intensity. This value is the product of the calculated [Win72] maximum cross section (using the best possible target/projectile combination) and the predicted proton branching ratio from statistical model calculations discussed below (assuming constant β-strength functions), normalized to 100 for ^{129}Nd. Other factors affecting the experimental yield of a particular isotope such as the diffusion rate of the different elements in the ion source, which affects short half-lives more strongly, or the different surface ionization efficiencies are not included.

3.2. MEASURABLE QUANTITIES

In order to extract information from the shape of the delayed proton spectrum which can be calculated in the framework of a statistical model discussed below, other relevant information about the precursor, emitter, and daughter nuclei need to be measured. A proton spectrum from an isolated precursor must be first obtained. For the relatively high Z precursors discussed here, most of the population of proton emitting levels occurs *via* electron capture. The characteristic K x rays following electron capture measured in coincidence with the delayed protons, therefore, uniquely identify the Z of the emitter and can be used to determine if there is more than one precursor present in a given isobaric chain. In cases where there is more than one precursor present, a different reaction (or projectile energy) or different counting intervals, if the half-lives are different, can be used to enhance one of the precursors. A more difficult situation is shown in Fig. 3.3 where both ^{151}Yb and ^{150}Tm have β-decaying isomers that also have delayed proton branches. In these cases, both the isomer and the ground state would give rise to K x rays with the same energy and would appear as a single precursor. Other information from such decays can be used to decide whether there is an isomer present but obtaining separate proton spectra from the isomer and the ground state is usually difficult.

The large fraction of β decays that occur via electron capture make possible a method of measuring the proton emitting level lifetimes known as the Particle X-ray Coincidence Technique (PXCT) [Har76]. This technique has been used in medium mass precursors (A~70) to test the level density, partial proton widths, and partial γ widths used in statistical model calculations. A K shell atomic vacancy is created approximately 80% of the time during electron capture for the range of elements discussed here. If the lifetime of the K vacancy is on the same order as the proton emitting level lifetime, then the K vacancy may be filled <u>before</u> the proton is ejected (Z-1 x rays are observed) or it may be filled <u>after</u> the proton has been ejected (Z-2 x rays are observed). Since the K vacancy lifetimes can be calculated precisely, a measurement of the (Z-1)/(Z-2) K x-ray intensity ratios can be used to determine the proton emitting level lifetimes. For the range of Z discussed here, the K vacancy filling is faster than the proton emission so only Z-1 x rays are expected. A second source of Z-2 energy x rays is the internal conversion of transitions from excited levels populated in the proton daughter nucleus. For many even-odd precursors studied here, the even-even proton daughters will have low-lying 2^+ levels and the subsequent E2 transitions will be converted (at Z~60, a 200 keV E2 transition will have a K conversion coefficient of 0.15) and produce Z-2 x rays. Knowledge of the final states populated in proton emission and the multipolarities of the transitions between them is, therefore, necessary before reliable PXCT results can be obtained.

The relative intensities of levels populated in the proton daughter nucleus (final state branches), from a measurement of γ-rays in coincidence with the delayed protons, can be used to determine or restrict the range of values for the precursor spin and parity. The experimental final state branches can be compared with the predicted branches from statistical model calculations for a series of precursor spins. Typically only one or two precursor spins will be consistent with the measured values. For even-odd precursors, the proton daughter is an even-even nucleus and the level energies, spins, and parities are often known from in-beam γ or from β-decay experiments. Final state branches have been measured for all even-odd precursors presented here. Corrections for detection efficiency, internal conversion, summing in the close counting geometries, and feedings from higher levels have been taken into account in extracting final state branches from the observed γ-ray intensities. For odd-odd precursors, the odd-even proton daughters are, in general, poorly studied and little is know about their low-lying level structure. Given the small number of proton events observed for most odd-odd precursors, it was impossible to measure final state branches in most cases.

The maximum proton decay energy that is observed (the endpoint of the proton spectrum) is related to the Q_{EC}-B_p value and in principle the proton spectrum can be used to determine this quantity in nuclei far from stability. Unfortunately, this requires very good statistics in the endpoint region. The Q_{EC}-B_p value is determined by calculating a proton spectrum with varying values for Q_{EC}-B_p until the best fit to the proton spectrum in the endpoint region is obtained. An example of this type of analysis can be found in [Jon76]. A more general method to determine Q_{EC}-B_p is to measure the electron capture to positron ratio of the proton emitting levels as a function of proton energy. The EC/β^+ ratio over a small proton energy interval determines the average β-decay energy to the proton emitting levels and when added to the average proton energy in the interval gives Q_{EC}-B_p. The EC/β^+ ratio is usually determined by counting protons in coincidence with positrons or 511 keV annihilation radiation and comparing to the total number of protons. Since a coincidence measurement is required, this technique is again limited to cases where the proton rate is high. When more than one final state in the proton daughter is fed, there are additional complications and the accuracy to which the final state branches are known will contribute to the uncertainty in Q_{EC}-B_p. Examples of this technique can be found in [Hor72a, Kar74, Tid85, Har87]. Both methods require that the β-strength function vary slowly with energy over the proton emitting region before reliable Q_{EC}-B_p values can be obtained. The number of protons observed for most of the precursors presented here was not sufficient for precise Q_{EC}-B_p determinations.

A very important quantity that can be measured is the proton branching ratio, P_p. The requires a measurement of the total proton intensity and total β-decay intensity for a particular precursor under identical experimental conditions. The total β-decay intensity is the sum of the positron intensity and the electron capture intensity. Since practically all isotopes in an isobaric chain will give rise to positrons, multicomponent decay analysis of the positrons must be used to get the fraction associated with a particular isotope. Limitations in such an analysis are that the half-lives of the isotopes in an isobaric chain must be sufficiently different and the β intensity of the isotope of interest must be a significant fraction of the total β intensity or the multicomponent analysis may fail. The electron capture intensity for each element can be determined from the intensities of the K x rays for each element in an isobaric chain. Although the K x rays can be clearly resolved and peak intensities accurately measured, the K x ray intensities may have contributions from internal conversion of transitions in the β-decay daughters. If these contributions are not known or cannot be measured, they will be a serious source of error. For precursors produced with large cross sections where detailed information on the precursor β decay is known or can be measured in the same experiment, reliable proton branching ratios can be determined. A very favorable case is a high-spin odd-odd precursor since the even-even β-decay daughter will not have any high spin levels at low excitation energies. Any levels populated in β decay will eventually decay through the 2^+ to 0^+ transition so the intensity of these γ-rays will equal the total β-decay intensity. Many of the odd-odd precursors presented here were produced in early experiments before γ-ray singles measurements were recorded so proton branching ratios could not be determined.

3.3. THE STATISTICAL MODEL

The density of states in a heavy mass emitter at excitation energies sufficient for proton emission is expected to be large enough for a compound nucleus or statistical model to apply. If there is no correlation between the preceding β decay and the subsequent level de-excitation (compound nucleus assumption), then delayed proton emission can be considered as a two step process: (i) β decay to an excited state in the emitter (ii) the de-excitation of this state *via* proton or γ-ray emission. The β intensity decreases rapidly as the excitation energy increases due to the decreasing available phase space whereas Γ_p/Γ_{tot} is zero below the proton emission threshold, increases rapidly with increasing proton energy above the threshold, and then changes more slowly as the proton energy approaches the Coulomb barrier. The product of these two factors gives the bell-shaped proton distribution characteristic of heavy precursors as shown in Fig. 3.5 for ^{123}Ce. The main features of a statistical description of delayed proton emission were first proposed in [Hor72b] with later refinements to include fluctuation phenomena [Kar73, Jon76] and improved prescriptions for quantities such as level densities and average radiation widths [Har81, Har82]. This model can predict the spectral shape, the proton branching ratio, and final state branches.

It is convenient to discuss the intensity distribution of the preceding β decay in terms of a β-strength function S_β [Han73] defined as a reciprocal *ft*-value calculated per MeV of final levels at excitation energy E^* in the emitter. The strength function contains the nuclear structure information while the kinematic effects are contained in the statistical rate function. Then the normalized total β intensity per MeV at excitation energy E^* in the emitter can be written as

$$I_\beta(E^*) = S_\beta(E^*)\, f(Z\text{-}1, Q_{EC}\text{-}E^*) \Big/ \int_0^{Q_{EC}} S_\beta(E)\, f(Z\text{-}1, Q_{EC}\text{-}E)\, dE\ , \qquad (3.1)$$

where $f = f_{\beta+} + f_{EC}$ is the sum of the statistical rate functions for β^+ and EC decay calculated according to [Gov71]. In order to evaluate eqn. 3.1, some assumption about the form of S_β must be made. The simplest form is S_β equal to a constant above a lower energy cutoff value. The cutoff values are chosen to be 60% of 0Δ, 2Δ, or 4Δ for even-even, odd-mass, and odd-odd precursors, respectively [Han73]. These cutoff values are multiples of the pairing energy since most of the protons that can β decay are in paired orbitals and most of the β strength, therefore, originates from the paired system. This form of S_β has been shown to be a reasonable approximation to measured electron capture strength functions using total absorption spectroscopy of neutron-deficient elements with $77 \le Z \le 86$ [Duk70].

Another form of S_β that may be used is from the gross theory of β decay [Tak73]. This model assumes the β-strength function can be represented by sums of single-particle strength functions. The single-particle strength functions are approximated with Gaussian or modified-Lorentz functions (several MeV wide) centered near the isobaric analog states. An appropriate single-particle model such as the Fermi-gas model is used to calculate level densities and the effects of the Pauli exclusion principle. Pairing effects are also incorporated in the model and calculations for both allowed and first-forbidden transitions are possible.

A more microscopic approach to allowed GT β-strength function calculations has recently become available [Kru84]. The Nilsson model, using the modified oscillator potential, is used to calculated the single-particle energy levels and wavefunctions used in the subsequent β-strength function calculation. The parameters of the potential are adjusted to reproduce the experimental single-particle levels for both spherical and deformed nuclei in the region of interest. The β-strength function calculation involves evaluating the GT β-decay operator between the Nilsson model generated initial and final state wavefunctions. Pairing is treated in the BCS approximation and a simple residual interaction is included by use of the Random Phase Approximation (RPA). The strength of the residual interaction is adjusted so that the calculation reproduces the experimental energies of the giant GT resonances for ^{208}Pb and ^{144}Sm. Further details of this model can be found in [Kru84]. The results from these calculations (discrete transition intensities from the β-decay parent to the calculated β-decay daughter levels) are smoothed with a Gaussian function before incorporation into the statistical model calculations. Figure 3.6 shows $I_\beta(E^*)$ for ^{123}Ce based on a constant S_β [Fig. 3.6(a)], a gross theory S_β [Fig. 3.6(b)], and a Nilsson/RPA calculated S_β [Fig. 3.6(c)].

The compound nucleus expression for the intensity of an individual proton transition I_p^{if} from a state i in the emitter to a state f in the proton daughter is given by

$$I_p^{if}(E_p) = \omega(J, J_i)\ I_\beta(E^*)\ \frac{\Gamma_p^{if}(E_p)}{\Gamma_\gamma^{i}(E^*) + \sum_{f'} \Gamma_p^{if'}(E_p')}, \tag{3.2}$$

where E_p is the energy of the emitted proton, $\Gamma_p^{if}(E_p)$ is partial proton width for a transition between initial state i and final state f, $\Gamma_\gamma^{i}(E^*)$ is the total γ width for state i, and the second term in the denominator is the sum over all final states of all open proton channels. The statistical weight factor for feeding of levels in the emitter with a spin J_i^π from a precursor with spin and parity J^π is approximated by

$$\omega(J, J_i) = (2J_i+1) / [3(2J+1)] . \tag{3.3}$$

The proton energy is related to the excitation energy E^* through the relationship

$$E^* = B_p + E_f + \frac{A}{A-1} E_p , \tag{3.4}$$

where B_p is the proton binding energy, E_f is the energy of state f in the daughter, and A is the emitter mass number. The proton partial width can be calculated in the optical model by means of the relationship

$$\Gamma_p^{if}(E_p) = [2\pi\rho_i(E^*)]^{-1} \sum_j T_{l,j}(E_p) , \tag{3.5}$$

where $\rho_i(E^*)$ is the density of levels with spin and parity J_i^{π}, $T_{l,j}(E_p)$ are the optical model transmission coefficients for protons of energy E_p and angular momentum l, and the sum extends over the partial waves permitted by the selection rules in spin and parity. The total γ width of state i, assuming E1 radiation dominates at high level densities, is given by [Bar73] as

$$\Gamma_\gamma^i(E^*) = \int_0^{E_{max}} E_\gamma^3 f_{E1}(E_\gamma) \sum_{j'=j-1}^{j'=j+1} \frac{\rho_{j'}(E^*-E_\gamma)}{\rho_j(E^*)} dE_\gamma , \qquad (3.6)$$

where ρ_j is the density of spin J states, f_{E1} is the strength function for E1 γ-decay; $f_{E1}(E_\gamma) = 8.7 \times 10^{-8}\, \sigma(E_\gamma) / E_\gamma$, and $\sigma(E_\gamma)$ is the photoabsorption cross section in mb [Har82].

Equation 3.2 is valid when individual proton transitions can be resolved, however, when the average spacing between levels in the emitter is less than the detector resolution, what is experimentally observed is a statistical average over many such transitions and the total proton intensity over a proton energy interval dE_p is

$$I_p(E_p)\, dEp = \sum_i \sum_f \omega(J, J_i) \langle I_\beta(E^*) \rangle \left\langle \frac{\Gamma_p^{if}(E_p)}{\Gamma_\gamma^i(E^*) + \sum_{f'} \Gamma_p^{if'}(E_p')} \right\rangle dE_p , \qquad (3.7)$$

where the sum is taken over all possible initial and final states that can give rise to a proton with energy in the interval E_p, E_p+dE_p and the brackets $\langle\,\rangle$ denote statistical averages of the enclosed quantities over the excitation energy associated with proton energies in the interval E_p, E_p+dE_p. The total proton intensity per β decay is

$$P_p = \int_0^{E_{p,max}} I_p(E_p)\, dE_p . \qquad (3.8)$$

The β intensity and the individual partial widths are proportional to the squares of nuclear matrix elements and are expected to have Porter-Thomas distributions about their means. The Porter-Thomas distribution is very skew and may give rise to significant fluctuations in the measured proton intensities. Attempts to extract quantities such as the level density from the magnitude of the fluctuations can be found in [Kar73, Jon76, Elm78].

A computer code that originated at CERN and GSI which calculates delayed proton spectra according to eqn. 3.7 was made available [Sch83] and calculations of spectral shapes, proton branching ratios, and final state feedings were performed with the input parameters discussed next. The precursor spin is considered as a variable unless known from previous experiments. The final state energies, spins, and parities are usually taken from the literature or from systematics. The different forms of S_β which could be used in the calculations were discussed above. Particle separation energies and β-decay Q values from the mass formula of [Lir76] were used based on comparisons with measured masses [Hau84] indicating that this model is better than other formulae at predicting masses in this region. In [Hor72b] the level density formula of [Gil65] and average radiation widths taken from [Cam57] were used but PXCT results [Har81, Har82] suggest that the back-shifted Fermi level densities [Dil73] and the the average radiation width based on photoabsorption cross sections, eqn. 3.6, give better agreement with experiment (for A~70 precursors) and have been used for the calculations presented here. Transmission coefficients can be calculated from the optical model with many different sets of parameters [Per63, Bec69, Joh70, Joh79]. The calculations presented here used the parameters from [Bec69]. In Fig. 3.7, the measured proton spectrum for ^{123}Ce is compared to statistical model calculations using a constant S_β [Fig. 3.7(a)], a gross theory S_β [Fig. 3.7(b)], and a Nilsson/RPA calculated S_β [Fig. 3.7(c)].

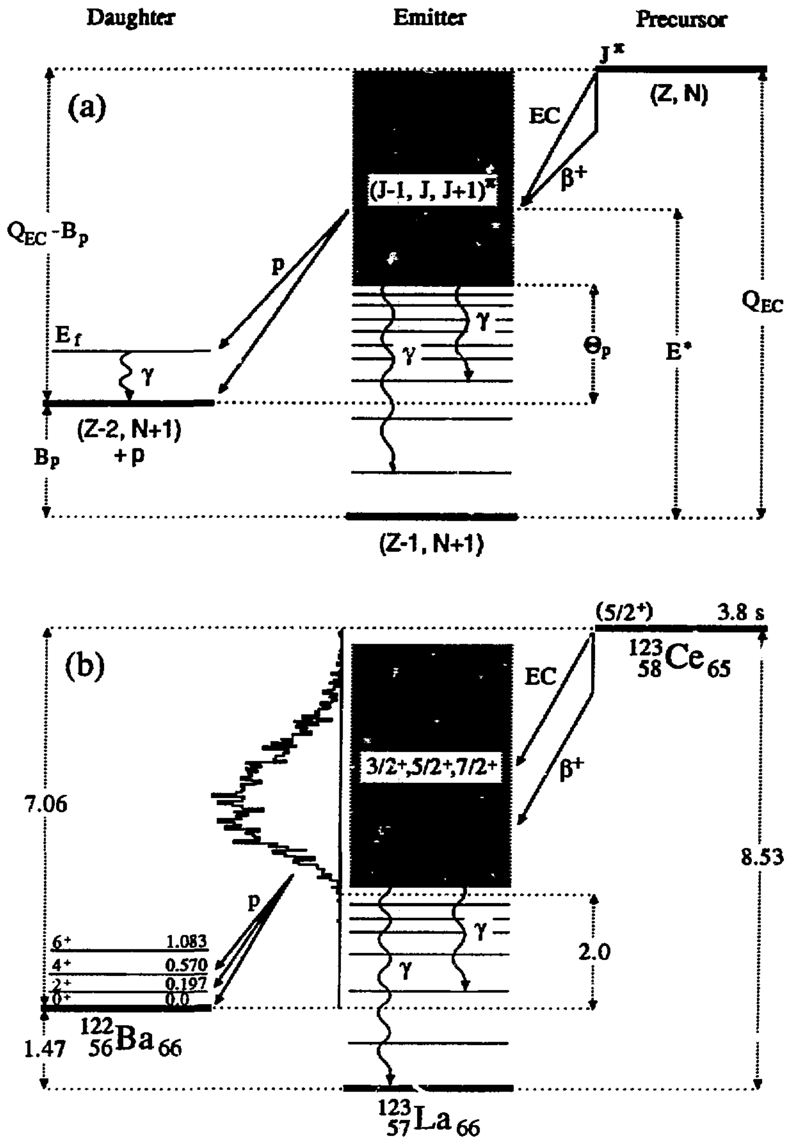

Figure 3.1. (a) Generic decay scheme for β-delayed proton emission from a single state at excitation energy E* and (b) delayed proton decay of ^{123}Ce. Notation and symbols are explained in the text. Energies are in MeV with Q values and separation energies from [Lir76].

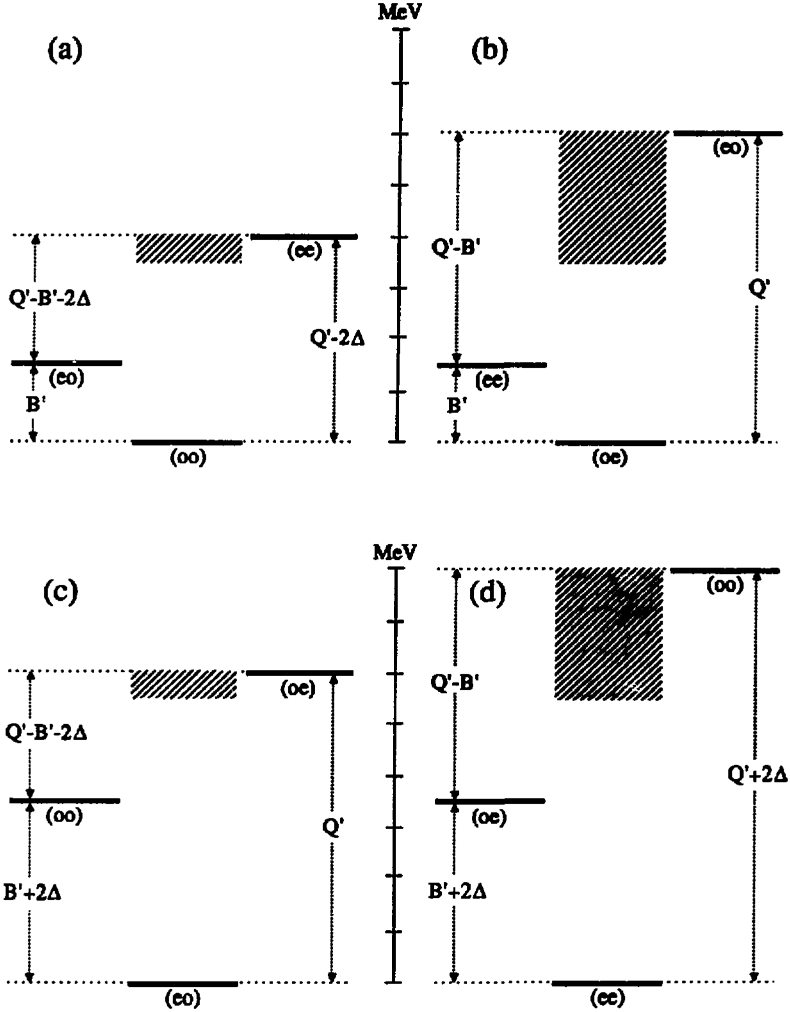

Figure 3.2. Effects of pairing on the energetics for delayed proton emission; (a) even-even precursor, (b) even-odd precursor, (c) odd-even precursor, and (d) odd-odd precursor. Electron capture Q values and proton binding energies are shown relative to the values for the even-odd precursor (denoted by Q' and B', respectively). Excitation energies greater than the proton emission threshold in each emitter are shaded. The energy required to break a pair 2Δ is about 2 MeV for A≈130 nuclei.

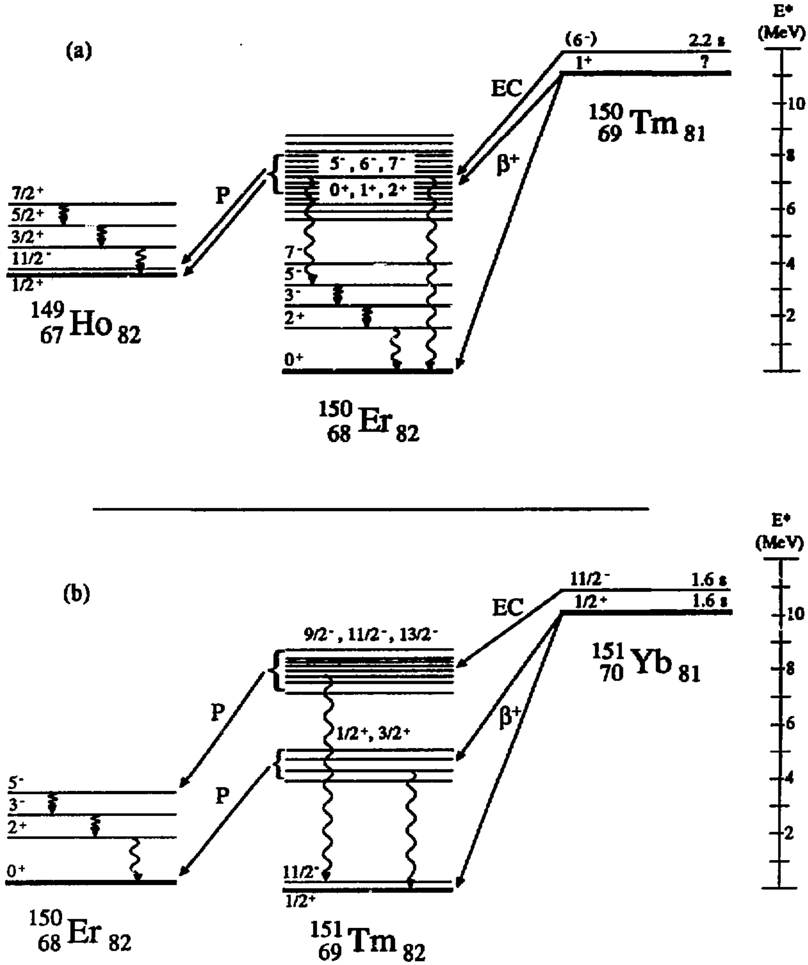

Figure 3.3. Schematic representation of delayed proton decay for (a) an odd-odd precursor and (b) for an even-odd precursor. Both precursors shown here have isomers with beta-delayed proton branches.

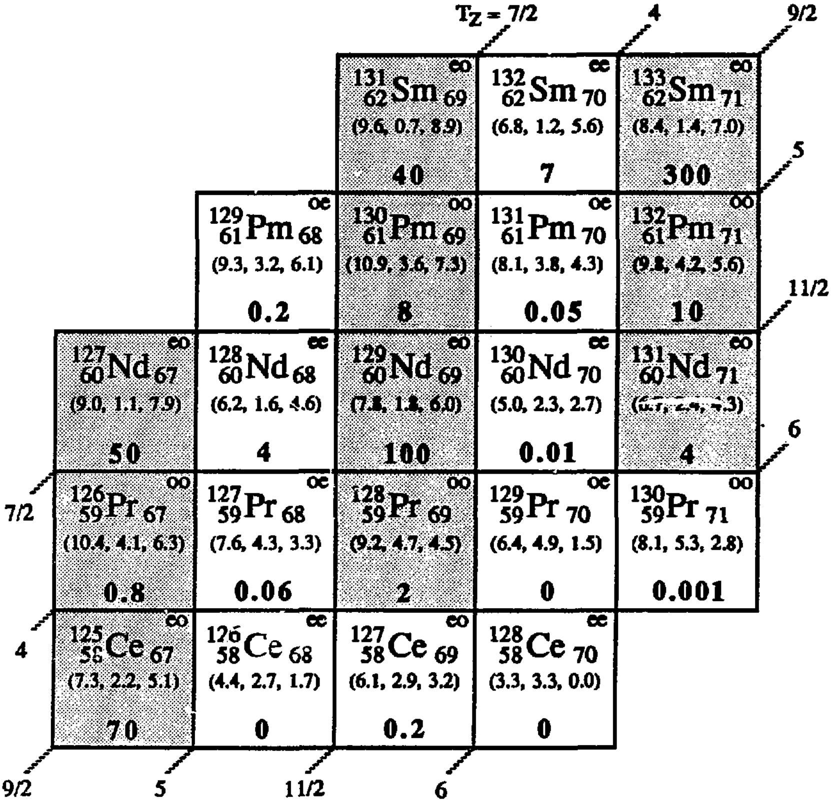

Figure 3.4. Region of the chart of nuclides around ^{129}Nd with a "figure of merit" assigned to each nuclide (shown in bold) estimating the relative intensity of delayed protons that would be experimentally observed. The "figure of merit" is the product of the maximum calculated cross section value and the calculated proton branching ratio normalized to the value for ^{129} Nd. The known delayed proton precursors are shaded. The Q_{EC} , B_p , and Q_{EC} -B_p values from [Lir76] are shown in parentheses for each nuclide.

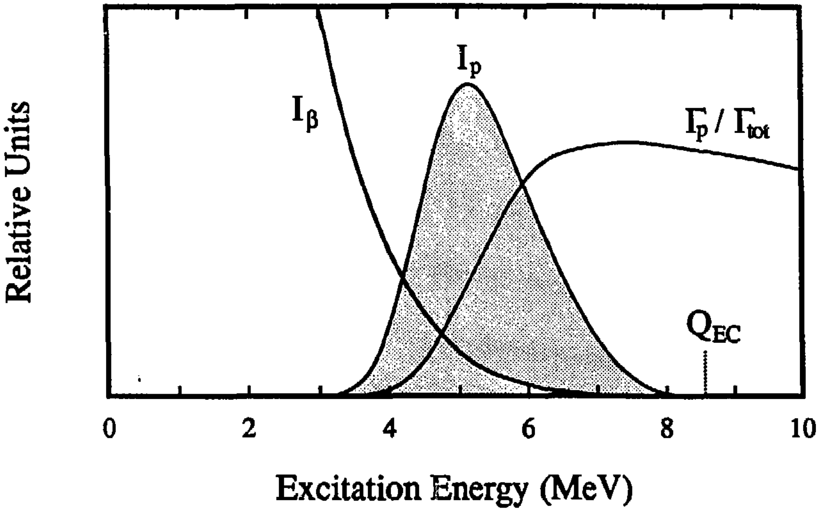

Figure 3.5. Beta intensity I_β (for a constant S_β) and a factor related to the competition between proton emission and gamma emission Γ_p / Γ_{tot} as a function of excitation energy in the emitter for ^{123}Ce. The product of the two factors (the shaded curve) represents the characteristic shape of delayed proton spectra from heavy mass precursors.

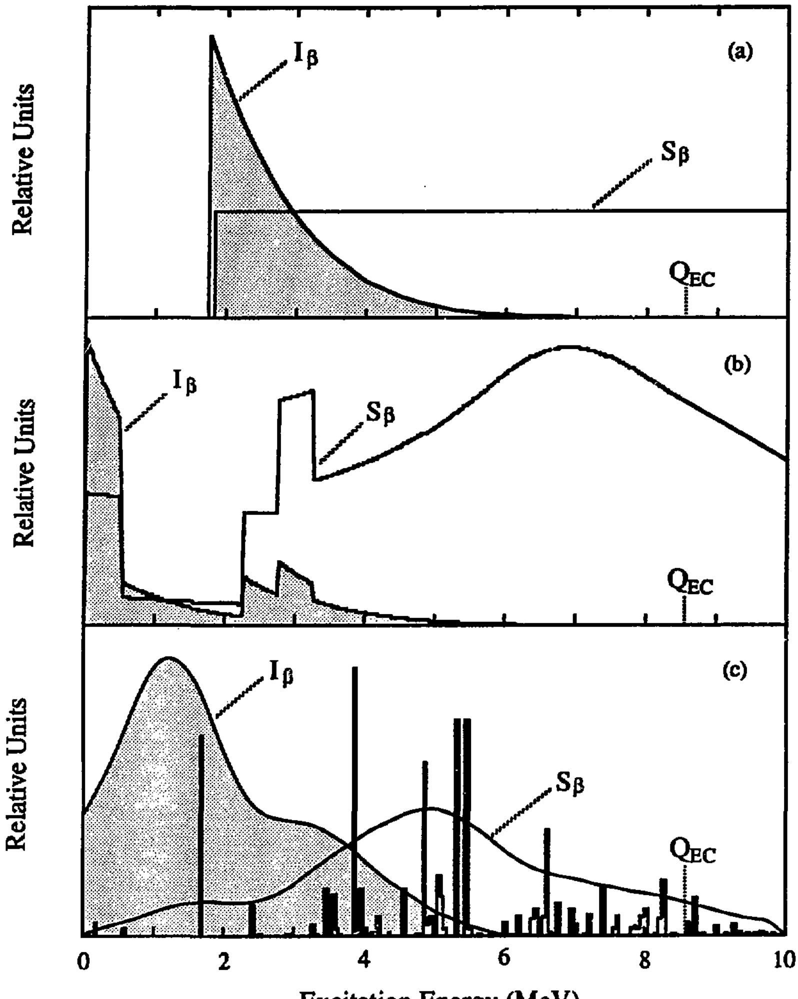

Figure 3.6. Beta-strength functions and total beta intensities for ^{123}Ce; (a) constant, (b) gross theory [Tak73], and (c) Nilsson/RPA calculated [Kru84]. The histogram in (c) is the calculation binned in 50 keV wide channels and the curve labeled S_β is the result of a Gaussian smoothing of the histogram with a sigma equal to 0.7 MeV.

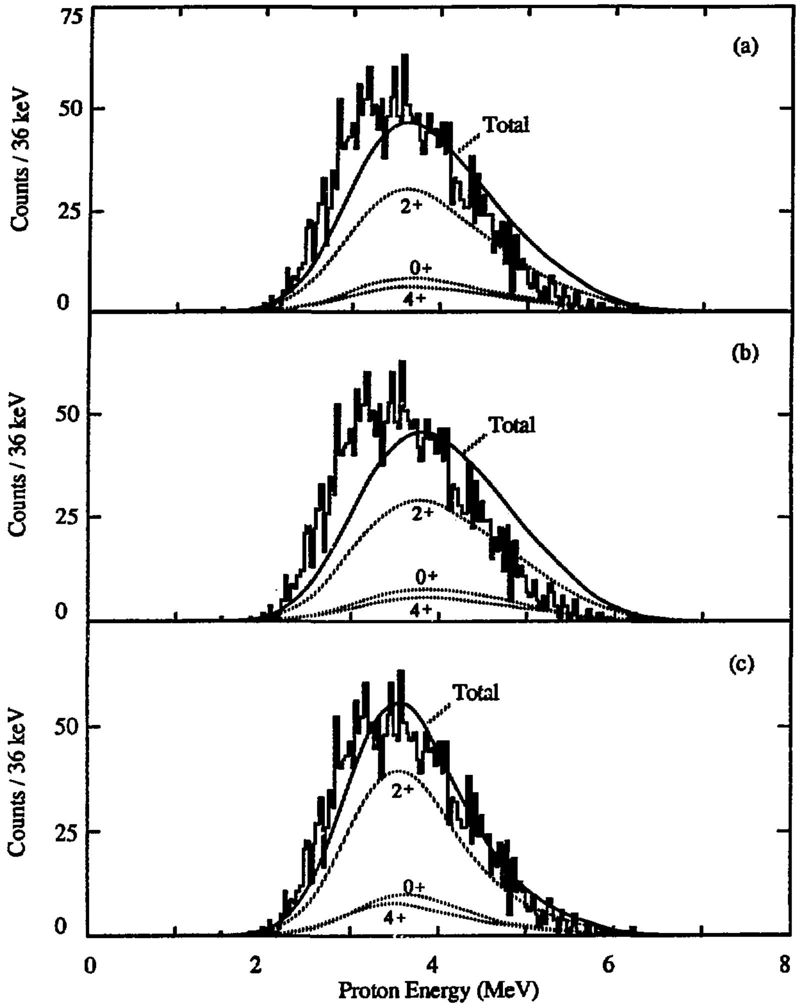

Figure 3.7. Comparison of calculated delayed proton spectra with experiment for ^{123}Ce. Calculations are for (a) constant, (b) gross theory, and (c) Nilsson/RPA calculated beta-strength functions. All calculations used Q values from [Lir76] and a precursor spin of 5/2$^+$. Also shown are the calculated contributions to the proton spectrum from decays to each of the final states in ^{122}Ba.

4. EVEN MASS PRECURSORS

4.1. GENERAL

Twenty precursors with even mass numbers have been studied; 17 of the precursors were odd-odd and 3 were even-even. In most cases the number of observed protons was a few hundred or less and half-lives and proton spectra were all that could be obtained. For two precursors, ^{148}Ho and ^{150}Tm, final state branching ratios were also measured. The reactions used to produce these precursors are summarized in Table 4.1. Also listed in Table 4.1 are the calculated cross sections, detector configurations, and dates when the bombardments were performed.

The measured half-lives of the delayed proton activities are given in Table 4.2. Information from the experiment that gave the best data for a given precursor is tabulated. For each precursor the date of the experiment (to correlate with entries in Table 4.1), counting intervals and the number of events observed at each counting interval is also given. The last two columns are predicted half-lives from the gross theory of β decay and values obtained from Nilsson/RPA β-strength function calculations. The gross theory values [Tak73, Tak88] were calculated using the modified Lorentz strength function with Q values from [Lir76]. The values in the last column were obtained by integrating the Nilsson/RPA calculated β-strength functions [Kru84] from 0 to Q_{EC} with an assumed Gamow-Teller quenching factor of 0.5 and Q values from [Lir76].

The delayed proton decay for each precursor is summarized in Table 4.3. The proton energy range is an estimate of the lowest and highest proton energies that were observed. The mean $\bar{x}$ and width $\bar{w}$ were calculated from the expressions:

$$\bar{x} = A^{-1} \Sigma x C_x \qquad \text{and} \qquad \bar{w} = 2.355 \sqrt{A^{-1} \Sigma C_x (x - \bar{x})^2} \;,$$

where the area A is the spectrum integral, C_x is the contents of channel x, and the sums are over all channels. Proton branching ratios and precursor spins are listed when known. The input parameters for statistical model calculations are given in Table 4.4. In many cases the precursor spin was not known and could only be estimated from systematics. In this region, 1^+ low-spin and 4^-, 5^-, or 6^- high-spin isomers are known in many odd-odd nuclei closer to stability and for the odd-odd precursors near N=82. Heavy-ion reactions are expected to strongly favor high-spin production, so spins of 5^- were assumed for precursors with Z<64 and spins of 6^- for precursors with Z>64.

The experimental results are presented in figures 4.1 though 4.18 which have a similar format. The top of each figure shows a delayed proton spectrum (the entries in Table 4.3 correspond to the spectra shown in the figures) plotted from 0 to 8 MeV at 36 keV per channel. Overlaying the measured proton spectrum are calculated proton spectra, normalized to the observed proton intensity, with the input parameters to the statistical model listed in Table 4.4. Each calculated proton spectrum is labeled with the respective β-strength function used in the calculation. Shown next is a representative proton coincident x-ray spectrum used for unambiguous Z indentifications. Due to the difficulty of gain shifting spectra with low statistics, data from different detectors or different experiments were not combined unless necessary . The measured x-ray energies are given in the figures while the literature values for each element are reproduced in Table 4.5. A decay curve of the delayed proton activity is shown for data corresponding to the counting interval listed in Table 4.2. In cases where final state feedings were observed, a proton coincident γ-ray spectrum is also shown.

4.2. DISCUSSION OF INDIVIDUAL PRECURSORS

Pertinent information for each precursor is given in Tables 4.1 to 4.4 and will not be repeated below. Half-lives for many of the precursors discussed here and in chapter 5 have been published in [Nit87] and complementary information from β-decay for some of the precursors is discussed in [Gil87] and [Tot87d].

^{120}La: This isotope was first reported in [Nit84] and is shown in Fig. 4.1.

^{122}La: The proton spectrum from an experiment using a dual telescope detector arrangement described in [Nit83b] is shown in Fig. 4.2(a) along with the calculated proton spectra. The results from a second experiment using the detector configuration listed in Table 4.1 are shown in Fig. 4.3. There were only 63 events observed in the second experiment and since the 10-s counting interval is about one half-life it was difficult to confirm the 8.7 s half-life from the first experiment. The decay curve in Fig. 4.3 was fitted with a fixed half-life of 8.7 s. Both experiments were first reported in [Nit84]. The Q_{EC} of 9.99 MeV from [Lir76] results in calculated half-lives that are too short and the calculated proton spectra do not match the measured spectrum in the endpoint region. Using a Q_{EC}=9.49 MeV resulted in a gross theory half-life of 7 s and an improved fit to the proton spectrum [Fig. 4.2(a)].

The β decay of ^{122}La has been studied in [Gen87] with a half-life of 8.5(6) s in agreement with the value listed in Table 4.2. The β-decay information suggests a possible precursor spin of 4 or 5.

^{124}Pr: The delayed proton data are shown in Fig. 4.4. Lanthanum K x rays and γ rays of 70, 113, and 166 keV were also observed in coincidence with the protons but the γ transitions cannot be uniquely placed since the level scheme of ^{123}La is not known. The β decay of ^{123}Ce was reported in [Gen87] and γ-rays of 66, 113, and 178 keV were observed but no level scheme for ^{123}La was given. Assuming any combination of M1 or E2 multipolarities for the above γ transitions, all La K x rays can be accounted for by internal conversion. The possibility that the La K x rays could originate from a weak delayed proton branch in ^{124}Ce can be excluded for the following reasons: (i) internal conversion can account for all La K x rays, (ii) statistical model calculations indicate that the proton branching ratio for ^{124}Ce should be about 10^3 times weaker than for ^{124}Pr (folding in cross section predictions, ^{124}Ce should still be 16 times weaker), and (iii) the decay of the proton activity gives, within the statistical uncertainty, no indication of a second, longer lived activity.

A weak 142 keV γ-ray decaying with a ~1 s half-life can be assigned to ^{124}Pr β decay and confirms the 2^+ to 0^+ transition in ^{124}Ce [Yin86].

^{126}Pr: This isotope was first identified in [Nit83a] from experiments completed prior to the construction of the tape system. The precursor Z assignment was based on systematics and predicted cross sections; no additional studies of this isotope have been performed. The proton spectrum is shown in Fig. 4.2(b). A recent β-decay study [Bér88] has reported a half-life of 3.0(4) s for ^{126}Pr, in excellent agreement with the value in Table 4.2. The β-decay results also indicate a likely precursor spin of greater than 5 or 6.

^{128}Pr: The proton activity at this mass number was at first assigned to ^{128}Nd [Nit83b] but a later experiment shown in Fig. 4.5 indicates delayed proton emission from only ^{128}Pr [Wil85]. No evidence for delayed proton decay from ^{128}Nd can be seen in the proton coincident x-ray spectrum and the decay curve appears to be a single component. The 3.1(3) s β decay of ^{128}Pr, which populated levels in ^{128}Ce most consistent with a spin of 4 or 5, has been recently reported in [Bér88].

^{130}Pm: The discovery of this isotope, shown in Fig. 4.6, was reported in [Wil85]. The proton spectrum was highly distorted in this experiment. It appeared that the protons were degraded in energy but, during an examination of the telescope at the end of the experiment, no absorbing material between the detectors and collection tape was found. Protons from ^{129}Nd were also produced and could be compared with the ^{129}Nd proton spectrum from a later experiment. A gain shifting procedure that was able to approximately reproduce the ^{129}Nd spectrum was also applied to ^{130}Pm and the result is shown in Fig. 4.6(a). No attempt was made to compare this proton spectrum with calculations.

^{132}Pm: This isotope was first identified by decay analysis of the Nd x rays associated with electron capture [Bog77]. A delayed proton branch was first identified in [Wil85] and is shown in Fig. 4.7. Recent studies [Bér87, Ker87b, Kor87] of the β decay of ^{132}Pm have been completed but little information other than half-lives was given. In both studies, the 4^+ level in ^{132}Nd but not the 6^+ was fed perhaps indicating a spin of 3 or 4 for ^{132}Pm.

^{134}Eu: A weak proton activity is assigned to ^{134}Eu (Fig. 4.8); further details can be found in [Vie88a].

^{136}Eu: The delayed proton decay of this isotope is shown in Fig. 4.9 and is reported in [Vie88a]. The β decay of ^{136}Eu was also studied in [Vie88a] where tentative 3^+, 7^+ spin assignments for the low- and high-spin isomers were proposed. Other recent studies of ^{136}Eu β decay have also been reported [Bér87, Ker87a, Ker87b].

^{140}Tb: Identification of this isotope was first published in [Wil86] and is shown in Fig. 4.10.

A=142: Two delayed proton activities, ^{142}Tb (Fig. 4.11) and ^{142}Dy (Fig. 4.12) have been identified at this mass number [Wil86]. Analysis of the β decay data yielded a ^{142}Dy half-life of 2.3(8) s and this value was used in the decay curves shown in Figs. 4.11 and 4.12. A high-spin isomer (6^-) and the ground state (1^+) in ^{142}Tb with half-lives of 0.3(1) s and 0.6(2) s, respectively, were also identified [Gil87] in the β-decay analysis. The high spin isomer must have a weak β-decay branch due to the short half-life and the proton decay curves are more consistent with a 0.6 s component so the ^{142}Tb precursor is tentatively assigned to the 1^+ ground state. It was not possible to obtain a clean proton spectrum associated with ^{142}Tb decay [Fig 4.11(a) is only ~33% Tb] therefore no calculations for ^{142}Tb are shown in Fig. 4.11. The proton spectrum in Fig. 4.12(a) associated with ^{142}Dy decay is composed of ~82% Dy and ~18% Tb based on the decay curve analysis (the Tb admixture to the proton spectrum may affect comparisons with the calculations).

A=144: A proton emitter with a half-life of 0.7(1) s was assigned to ^{144}Ho on the basis of Dy K x rays observed in coincidence with the protons [Wil86]. A second delayed proton activity with a half-life of 7(3) s was assigned to ^{144}Dy

[Wil85] from proton coincident Tb K x rays. In the 3/84 experiment, a GeLi detector with poorer resolution and efficiency had to be used and the assignment of the longer lived proton activity *via* coincident x rays was difficult. In a later experiment, using a reaction where the production of ^{144}Ho was predicted to be negligible, the proton activity could be assigned to ^{144}Dy and the data from this experiment are shown in Fig. 4.13. The β decay of ^{144}Dy was reported in [Red86, Gil87] with a half-life of 9.1(5) s. Using this half-life value in the decay analysis shown in Fig. 4.14(c), it can be calculated that the proton spectrum in Fig. 4.14(a) contains ~15% ^{144}Dy and 85% ^{144}Ho. The proton spectrum associated with ^{144}Dy [Fig. 4.13(a)] is quite narrow and may distort the ^{144}Ho proton spectrum in Fig. 4.14(a). The statistics are too low to subtract the experimental ^{144}Dy spectrum [Fig. 4.13(a)] from the spectrum in Fig. 4.14(a) in order to get a better estimate of the ^{144}Ho proton spectrum. Instead, the calculations shown in Fig. 4.14(a) are a mixture of ^{144}Dy and ^{144}Ho (15% and 85%, respectively). No conclusive evidence for a delayed proton branch in ^{144}Tb, which has a Q_{EC}-S_p similar to ^{144}Dy was obtained.

^{146}Ho: The β-decay of ^{146}Ho was first reported in [Gui82]. The delayed proton branch was identified in [Wil86] and is shown in Fig. 4.15.

A=148: The high-spin isomer of ^{148}Ho was first observed in [Tot79] with a half-life of 9(1) s. The low-spin (1$^+$) isomer with a half-life of 2(1) s was identified in [Nol82b]. Detailed studies of ^{148}Ho β decay [Tot88] and ^{148}Ho delayed proton decay [Nit88] have been recently carried out. The presence of a delayed proton branch in ^{148}Er was also found in [Nit88] and the delayed protons shown in Fig 4.16(a) are ~20% Er and ~80% Ho from decay analysis and x-ray intensities. Since a clean ^{148}Er spectrum could not be obtained, only calculated spectra for ^{148}Ho are shown.

Weak γ transitions in ^{147}Tb were observed in coincidence with ^{148}Ho protons with the following intensities: 6(4)% to the 7/2$^+$ level, 1(4)% to the 5/2$^+$ level, 3(5)% to the 3/2$^+$ level, and 90(20)% to both the 1/2$^+$ and 11/2$^-$ levels. The calculated values for a 6$^-$ precursor are: 2% to the 7/2$^+$ level, 2% to the 5/2$^+$ level, 1% to the 3/2$^+$ level, and 95% to the 11/2$^-$ level. The calculated feedings are in good agreement with the measured values.

^{150}Tm: The isotope ^{150}Tm was first identified in [Nol82a] with a more extensive study of its β decay reported in [Tot87b] where a half-life of 2.2(2) s for the 6$^-$ state of ^{150}Tm was obtained. There was indirect evidence that a low-spin (1$^+$) isomer in ^{150}Tm was also present but no isomeric transition was observed and no half-life determined. A detailed study of the delayed proton decay [Nit88] was recently completed. The delayed proton spectrum, etc. are shown in Fig. 4.17. The final state feedings to levels in ^{149}Ho are summarized in Table 4.6 where a mixture of 20% 1^+ and 80% 6^- precursors gave the best result.

^{152}Lu: The first observation of ^{152}Lu and its β decay to levels of ^{152}Yb was reported in [Tot87a]. From the observation of an allowed transition to a 5^- level it was concluded that the spin/parity of ^{152}Lu is 4^-, 5^-, or 6^-. No evidence for a low-spin isomer was seen. The delayed proton decay was reported in [Nit88] and the data are shown in Fig. 4.18.

^{154}Lu: In a preliminary experiment, fifteen delayed proton events and a few possible delayed α events were assigned to ^{154}Lu based on energetics, half-life, and cross section predictions [Vie88b]. No particle coincident x rays were observed due to the poor statistics so the Z assignment is somewhat uncertain at this time. This is the first evidence for delayed α emission near the N=82 closed shell.

Table 4.1. Reactions used to produce even-mass delayed proton precursors; Thickness = target thickness, E_{HILAC} = beam energy at machine exit, E_{Target} = calculated beam energy at target center, σ = calculated cross section, Detectors = detector configuration used.

Isotope	Reaction	Thickness (mg/cm^2)	E_{HILAC} (MeV)	E_{Target} (MeV)	σ[a] (mb)	Date[b]	Detectors[c]
^{120}La	$^{58}Ni(^{64}Zn,pn)$	2	380	253	3.5	9/83	A
^{122}La	$^{92}Mo(^{36}Ar,3p3n)$	2	196	188	7	9/83	A
^{124}Pr	$^{92}Mo(^{36}Ar,p3n)$	2	186	174	0.4	4/86	B
^{128}Pr	$^{92}Mo(^{40}Ca,3pn)$	2	195	186	100	10/84	A
^{130}Pm	$^{92}Mo(^{40}Ca,pn)$	2	182	170	0.2	7/84	A
^{132}Pm	$^{96}Ru(^{40}Ca,3pn)$	0.8	195	175	90	10/84	A
^{134}Eu	$^{92}Mo(^{46}Ti,p3n)$	2	223	212	0.8	11/86	C
^{136}Eu	$^{92}Mo(^{46}Ti,pn)$	2	204	192	1.5	11/86	C
^{140}Tb	$^{92}Mo(^{54}Fe,3p3n)$	2	312	297	5	12/85	B
^{140}Tb	$^{92}Mo(^{52}Cr,p3n)$	2	244	230	2	2/87	C
^{142}Dy	$^{92}Mo(^{54}Fe,2p2n)$	2	277	261	5	2/84	A
^{142}Tb	$^{92}Mo(^{54}Fe,3pn)$	2	277	261	35	2/84	A
^{142}Dy	$^{92}Mo(^{54}Fe,2p2n)$	2	261	247	4.5	12/85	B
^{142}Tb	$^{92}Mo(^{54}Fe,3pn)$	2	261	247	60	12/85	B
^{142}Dy	$^{92}Mo(^{52}Cr,2n)$	2	224	210	1	2/87	C
^{142}Tb	$^{92}Mo(^{52}Cr,pn)$	2	224	210	10	2/87	C
^{144}Ho	$^{92}Mo(^{56}Fe,p3n)$	2	273	257	0.4	2/84	A
^{144}Dy	$^{92}Mo(^{56}Fe,2p2n)$	2	273	257	17	2/84	A
^{144}Tb	$^{92}Mo(^{56}Fe,3pn)$	2	273	257	80	2/84	A
^{144}Ho	$^{92}Mo(^{58}Ni,3p3n)$	2	342	325	0.8	3/84	A
^{144}Dy	$^{92}Mo(^{58}Ni,4p2n)$	2	342	325	11	3/84	A
^{144}Tb	$^{92}Mo(^{58}Ni,5pn)$	2	342	325	23	3/84	A
^{144}Dy	$^{92}Mo(^{56}Fe,2p2n)$	2	261	245	18	6/85	B
^{144}Tb	$^{92}Mo(^{56}Fe,3pn)$	2	261	245	100	6/85	B
^{146}Ho	$^{92}Mo(^{58}Ni,2p2n)$	2	278	262	40	11/84	A
^{148}Er	$^{94}Mo(^{58}Ni,2p2n)$	2	275	257	9	11/85	B
^{148}Ho	$^{94}Mo(^{58}Ni,3pn)$	2	275	257	80	11/85	B
^{150}Tm	$^{96}Ru(^{58}Ni,3pn)$	1.5	372	267	22	11/85	B
^{152}Lu	$^{96}Ru(^{58}Ni,pn)$	1.5	354	244	0.4	4/85	B
^{154}Lu	$^{92}Mo(^{64}Zn,pn)$	2	285	267	0.6	12/87	C

[a] Calculated from [Win72].

[b] To indicate when more than one experiment was performed at a given mass chain and to correlate with entries in Table 4.2.

[c] The symbols A, B, and C refer to the detector configurations shown in Figure 3.3.

Table 4.2. Half-lives of even-mass delayed proton precursors; Transit Time = tape transport time, Cycle Time = length of collection and counting intervals, No. of Events = number of delayed protons at the respective counting cycle, $T_{1/2}$ Exp. = measured half-life, $T_{1/2}$ g.t. = predicted half-life from the gross theory of β decay, $T_{1/2}$ RPA = half-life from Nilsson/RPA β-strength function calculations.

Isotope	Date	Transit Time (s)	Cycle Time (s)[a]	No. of Events	$T_{1/2}$ Exp.[b] (s)	$T_{1/2}$ g.t.[c] (s)	$T_{1/2}$ RPA[d] (s)
^{120}La	9/83	0.07	5,<u>10</u>	62,441	2.8(4)	1.4	1.8
^{122}La[e]	5/83	--	-	1800	8.7(7)	4.2	5.5
^{124}Pr	4/86	0.25	4	493	1.2(2)	1.0	0.6
^{126}Pr[f]	10/82	--	--	171	3.2(6)	3.0	2.0
^{128}Pr	10/84	0.25	12	126	4(1)	9.2	7.7
^{130}Pm	7/84	0.25	8	62	2(1)	2.3	1.7
^{132}Pm	10/84	0.25	12	287	5(1)	5.7	3.7
^{134}Eu	11/86	0.07	4	34	0.5(2)	1.4	1.3
^{136}Eu	11/86	0.07	4,<u>16</u>	44,167	4(1)	3.8	1.8
^{140}Tb	12/85	0.25	8	206	2.0(5)	2.2	2.0
^{142g}Tb	2/87	0.07	2.4	144[g]	0.6(2)[h]	4.9	3.5
^{142}Dy	12/85	0.25	8	115[g]	2.3(3)[h]	4.2	2.7
^{144}Dy	6/85	0.25	12	66[g]	9.1(5)[h]	9.3	9.7
^{144}Ho	3/84	0.07	2.4,<u>5</u>,50	42[g],345[g],67[g]	0.7(2)	1.5	1.3
^{146}Ho	11/84	0.25	12	288	3.1(5)	2.6	2.9
^{148}Ho[i]	11/85	0.25	16	1975[g]	9.7(3)[h]	4.8	5.9
^{148}Er	11/85	0.25	16	1975[g]	4.4(2)[h]	4.2	2.4
^{150}Tm[i]	11/85	0.25	8	6191	2.2(2)	1.5	0.9
^{152}Lu[i]	4/85	0.25	4	353	0.7(1)	0.6	0.3
^{154}Lu	12/87	0.07	2.56	~15	~1	3.1	1.4

[a] Decay curves are shown in Figures 4.1 to 4.18. When more than one tape cycle was used only the underlined cycle time is presented in the corresponding figure.

[b] Best value from all available proton data.

[c] Values from the gross theory [Tak73, Tak88] using the modified Lorentz strength function.

[d] Calculated by integrating β-strength functions from [Kru84] assuming a Gamow-Teller quenching factor of 0.5.

[e] Data taken from [Nit84].

[f] Data taken from [Nit83b].

[g] Mixture of all delayed protons in this isobaric chain.

[h] Half-lives quoted are values from β-delayed γ rays given in [Nit87] and references cited therein.

[i] Decay dominated by high spin (~6⁻) isomer.

Table 4.3. Summary of the delayed proton decay of even-mass precursors; Type = type of precursor: odd-odd (oo) or even-even (ee), T_z = 1/2(N-Z) precursor isospin projection, No. of Events = number of protons shown in Figures 4.1(a) to 4.18(a), Range = approximate lowest and highest observed proton energies, $\bar{x}$ = average proton energy, $\bar{w}$ = FWHM of proton distribution, P_p = measured proton branching ratio, and J^π = precursor spin and parity.

Isotope	Type	T_z	No. of Events	Range (MeV)	$\bar{x}$ (MeV)	$\bar{w}$ (MeV)	P_p	J^π
^{120}La	oo	3	508	2.0,5.6	3.71(3)	1.67(8)	–	–
^{122}La[a]	oo	4	1813	2.0,4.8	3.42(2)	1.46(4)	–	–
^{124}Pr	oo	3	493	2.1,7.0	3.73(3)	1.68(8)	–	–
^{126}Pr[b]	oo	4	191	2.1,5.4	3.67(5)	1.61(9)	–	–
^{128}Pr	oo	5	123	1.9,4.2	3.24(4)	1.11(9)	–	–
^{130}Pm[c]	oo	4	62	–	–	–	–	–
^{132}Pm	oo	5	286	2.1,5.0	3.60(3)	1.26(9)	–	–
^{134}Eu	oo	4	35	2.1,6.0	3.7(2)	2.2(4)	–	–
^{136}Eu	oo	5	211	2.4,5.7	3.90(5)	1.66(9)	$9(3)\times10^{-4}$	(3+)
^{140}Tb	oo	5	350	2.0,6.6	4.18(4)	1.85(9)	$7(3)\times10^{-3}$	(6-)
^{142g}Tb	oo	6	144[d]	2.0,5.1	~3.7	~1.4	–	(1+)
^{142}Dy	ee	5	115[e]	2.5,5.2	~3.9	~1.4	–	0+
^{144}Dy	ee	6	66	2.5,4.5	3.25(5)	1.00(9)	–	0+
^{144}Ho	oo	5	345[f]	2.2,7.0	4.15(5)	2.12(9)	–	–
^{146}Ho	oo	6	288	2.3,6.3	4.13(4)	1.76(9)	–	–
^{148}Ho	oo	7	1975[g]	2.2,5.4	4.07(1)	1.27(3)	$8(2)\times10^{-4}$	(6-)
^{148}Er	ee	6	–	–	–	–	–	0+
^{150}Tm	oo	6	6182	2.2,7.5	4.71(1)	2.09(3)	$1.2(4)\times10^{-2}$	(1+,6-)[h]
^{152}Lu	oo	5	353	2.3,7.9	4.56(5)	2.28(9)	$1.5(7)\times10^{-1}$	(6-)
^{154}Lu	oo	6	~15	–	~4.3	–	$\sim6\times10^{-4}$	(7+)

[a] Data taken from [Nit84].
[b] Data taken from [Nit83b].
[c] Proton energies could not be determined. See text for details.
[d] Proton activity is 67% ^{142}Dy and 33% ^{142}Tb.
[e] Proton activity is 82% ^{142}Dy and 18% ^{142}Tb.
[f] Proton activity is 85% ^{144}Ho and 15% ^{144}Dy.
[g] Proton activity is 82% ^{148}Ho and 18% ^{148}Er.
[h] Relative position of high- and low-spin isomers is unknown. High-spin decay is expected to dominate and proton branching ratio is for the 6- precursor.

Table 4.4. Input parameters for statistical model calculations of even-mass precursors; J^{π} = precursor spin and parity, Q_{EC} = β^{+}/EC decay energy, B_p = proton binding energy, Final States = references where energies, spins, and parities of levels in the final nucleus can be found. All calculations used level density parameters from [Dil73], optical model parameters from [Bec69], average radiation widths from [Har82], and gross theory or Nilsson/RPA β-strength functions (as indicated in Figures 4.1 to 4.18).

Isotope	J^{π}	Q_{EC}[a] (MeV)	B_p[a] (MeV)	Final States
^{120}La	5⁻	11.37	3.75	[Gar78, Gar79]
^{122}La	5⁻	9.99	4.49	[Eks77, Gar78, Gar79]
^{124}Pr	5⁻	11.76	3.40	[Gen87], systematics
^{126}Pr	5⁻	10.43	4.08	[Lei73, Gen87]
^{128}Pr	5⁻	9.21	4.72	[War75, Smi85, Gen87]
^{130}Pm	5⁻	10.92	3.60	systematics
^{132}Pm	5⁻	9.75	4.20	[God87]
^{134}Eu	5⁻	11.44	3.09	[Lis85, Wad87b]
^{136}Eu	3⁺	10.30	3.67	[Lis85, Wad87b, Wad88, Vie88a]
^{140}Tb	6⁻	10.88	3.18	[Red86, Bis88]
^{142g}Tb	1⁺	9.91	3.76	[Lun86, Red86, Gil87, Tur81]
^{142}Dy	0⁺	7.13	0.93	[Gil87, Tur87]
^{144}Dy	0⁺	6.24	1.55	[Oll85, Red86, Tur87]
^{144}Ho	6⁻	11.48	2.76	[Oll85, Red86]
^{146}Ho	6⁻	10.57	3.35	[Alk82, Nol82b]
^{148}Ho	6⁻	9.90	3.98	[Nag81, Tot82, Alk83, Sty83, Sch84a]
^{148}Er	0⁺	7.04	1.21	[Nol82b]
^{150}Tm[b]	1⁺,6⁻	11.36	2.99	[Wil80, Tot85]
^{152}Lu	6⁻	12.75	2.02	[Nol82c]

[a] Reference [Lir76].

[b] The calculations shown in Fig. 4.17 are for the 6⁻ precursor.

Table 4.5. Energies (and approximate intensities) of K x rays for lanthanide elements from Ref. [TOI78] appendix III. Energies are given in keV.

Element	$K_{\alpha 1}$ (I~100)	$K_{\alpha 2}$ (I~55)	$K_{\alpha,ave.}$	$K_{\beta 1}$ (I~31)	$K_{\beta 1}$ (I~8)	$K_{\beta,ave.}$
Cesium	30.97	30.63	30.85	35.0	35.8	35.2
Barium	32.19	31.82	32.06	36.4	37.3	36.6
Lanthanum	33.44	33.02	33.30	37.8	38.7	38.0
Cerium	34.72	34.28	34.56	39.2	40.2	39.5
Praseodymium	36.03	35.55	35.86	40.7	41.8	41.0
Neodymium	37.36	36.85	37.18	42.2	43.3	42.5
Promethium	38.72	38.17	38.52	43.8	44.9	44.1
Samarium	40.12	39.52	39.91	45.4	46.6	45.7
Europium	41.54	40.90	41.31	47.0	48.3	47.3
Gadolinium	43.00	42.31	42.75	48.7	50.0	49.0
Terbuim	44.48	43.74	44.21	50.3	51.7	50.7
Dysprosium	46.00	45.21	45.72	52.1	53.5	52.4
Holmium	47.55	46.70	47.24	53.8	55.3	54.2
Erbium	49.13	48.22	48.80	55.6	57.2	56.3
Thulium	50.74	49.77	50.39	57.5	59.1	57.8
Ytterbium	52.39	51.35	52.01	59.3	61.0	59.7
Lutetium	54.07	52.97	53.67	61.2	63.0	61.6

Table 4.6. Relative experimental and calculated β-delayed proton branches from ^{150}Tm to levels in ^{149}Ho. The last column represents a mixture of 80% 6^- decay and 20% 1^+ decay.

Levels in ^{149}Ho		Relative Proton Branches (%)			
J^π	Energy (keV)	Experiment	$^{150}Tm(6^-)$ calc.	$^{150}Tm(1^+)$ calc.	[0.8(6^-) + 0.2(1^+)] cacl.
$1/2^+$ $11/2^-$	0	78(5)	92	46	83
$3/2^+$	171.5	7(3)	2	41	9
$5/2^+$	515.4	4(2)	2	12	4
$7/2^+$	952.1	5(2)	2	1	2
$15/2^+$ [a]	1380 [b]	5(3)	2	--	1
$15/2^-$ [a]	1560 [b]	1(1)	1	--	1

[a] Spin and parity assignments of these levels are uncertain; the statistical model calculations are, however, not sensitive to variations of ± 1 unit of angular momentum because of the small relative branches.

[b] Reference [Wil80].

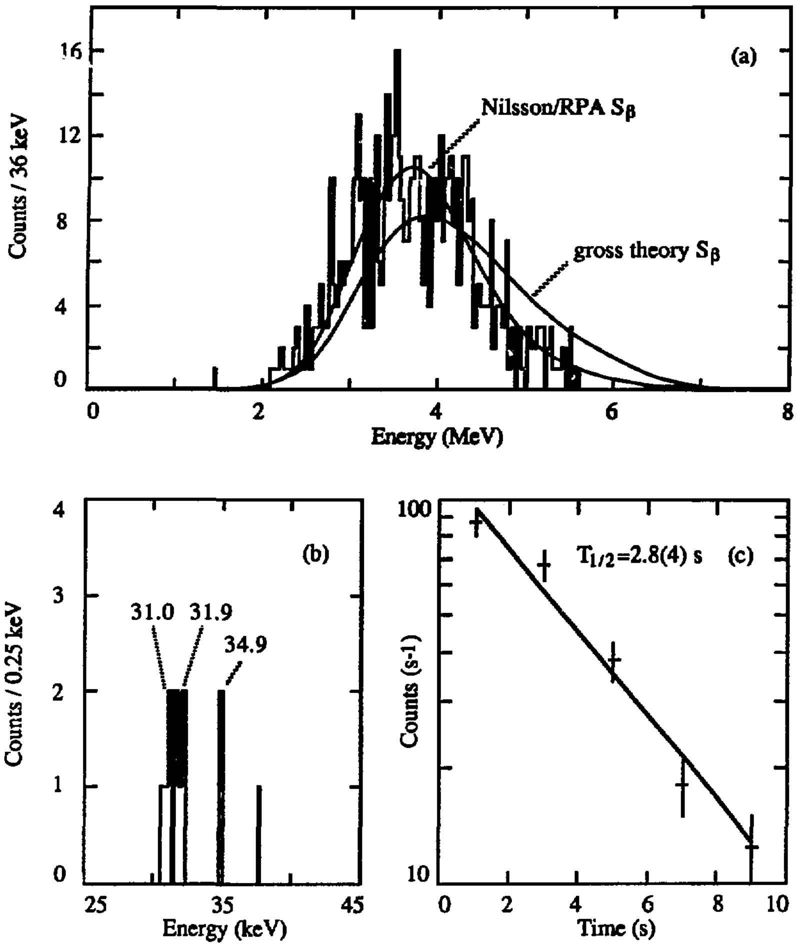

Figure 4.1. Decay of ^{120}La; (a) beta-delayed proton spectrum, (b) proton coincident x-ray spectrum, and (c) decay of the proton activity. The smooth curves in (a) are the results of statistical model calculations using the indicated beta-strength functions.

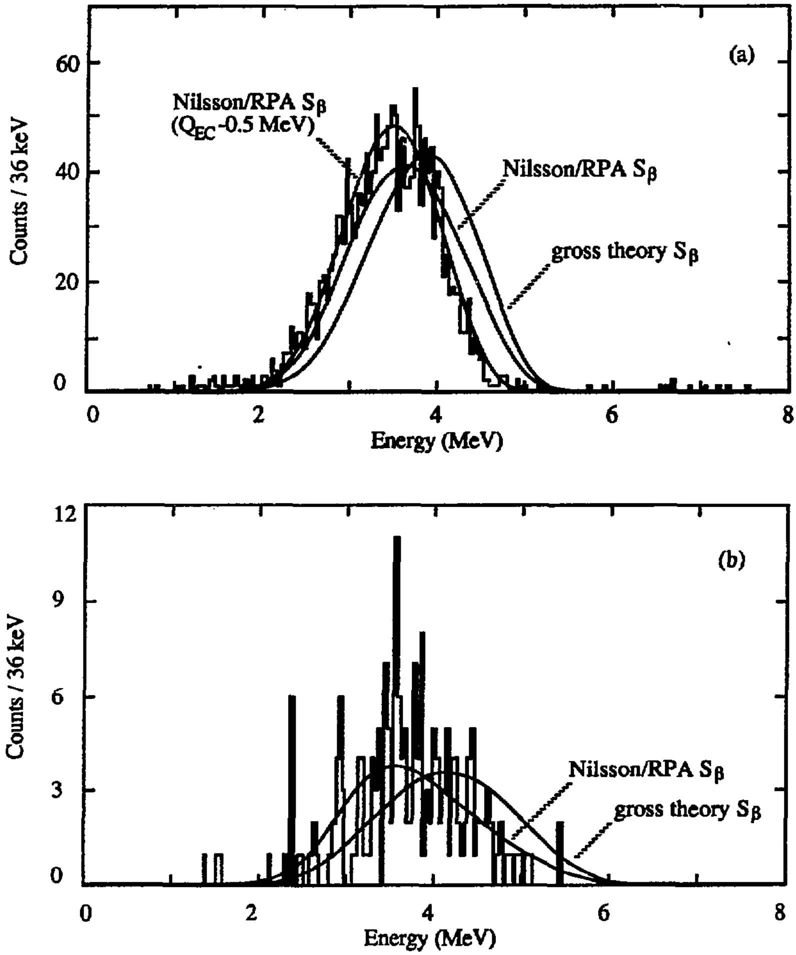

Figure 4.2. Delayed proton spectra of (a) ^{122}La, and (b) ^{126}Pr from experiments performed before the tape system was completed. The smooth curves in each figure are the results of statistical model calculations using the indicated beta-strength functions. The data were first reported in [Nit84] and [Nit83b], respectiveley.

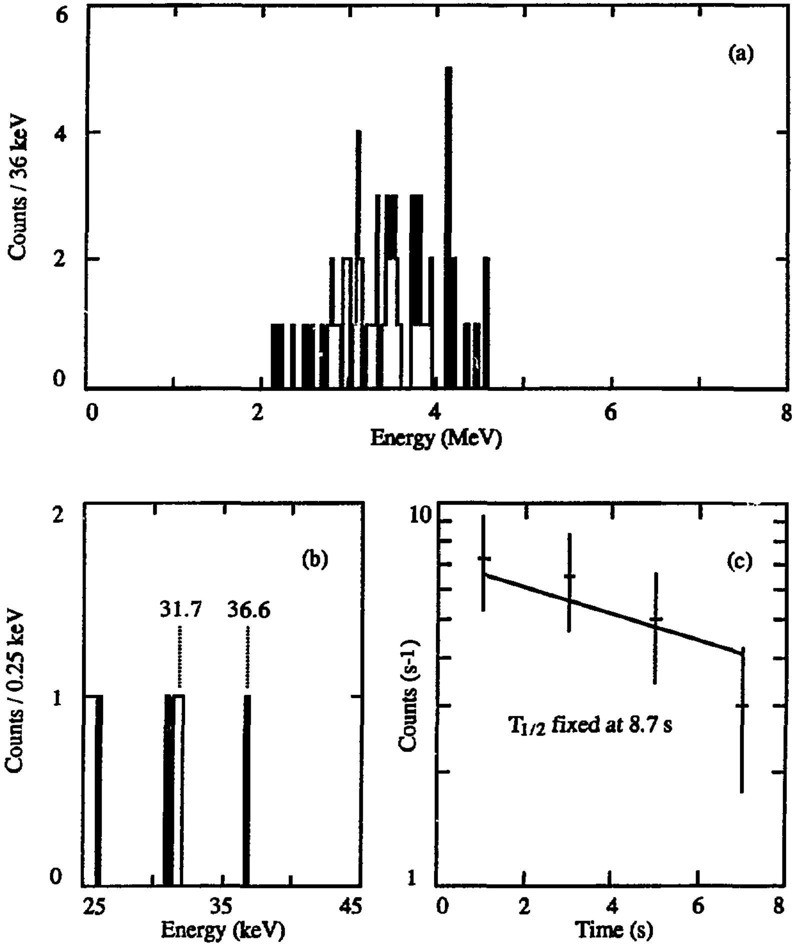

Figure 4.3. Decay of ^{122}La; (a) beta-delayed proton spectrum, (b) proton coincident x-ray spectrum, and (c) decay of the proton activity.

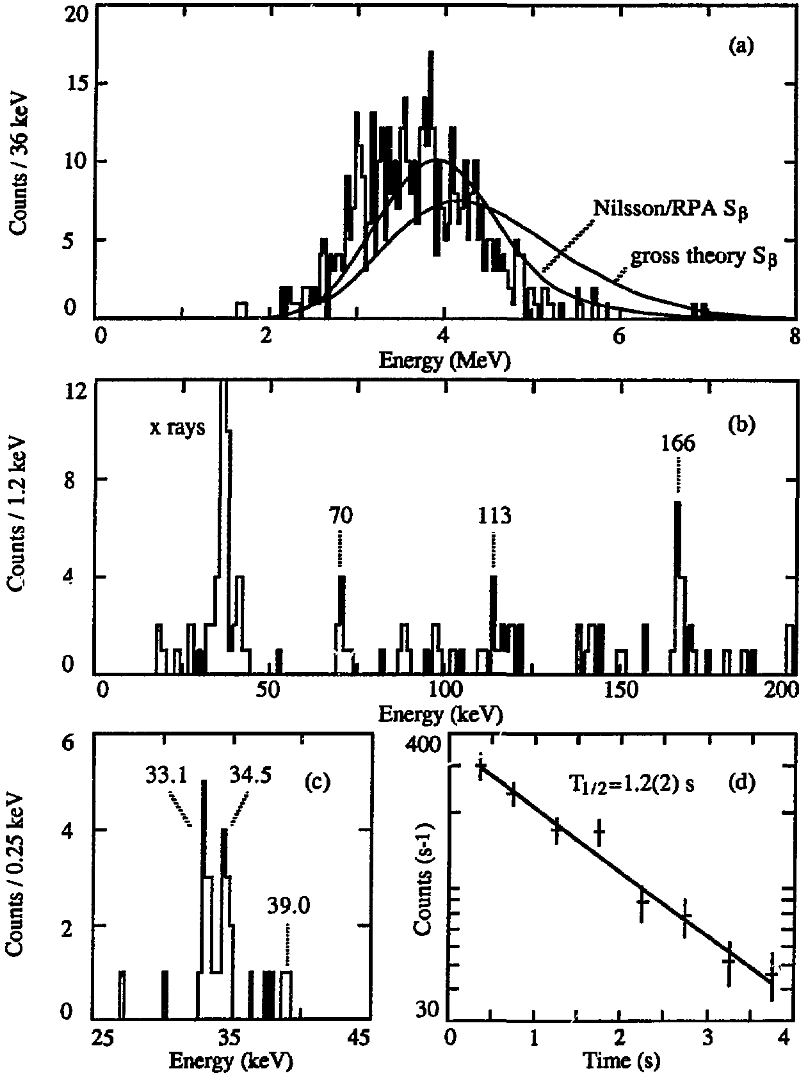

Figure 4.4. Decay of ^{124}Pr; (a) beta-delayed proton spectrum, (b) proton coincident gamma-ray spectrum, (c) proton coincident x-ray spectrum, and (d) decay of the proton activity. The smooth curves in (a) are the results of statistical model calculations using the indicated beta-strength functions.

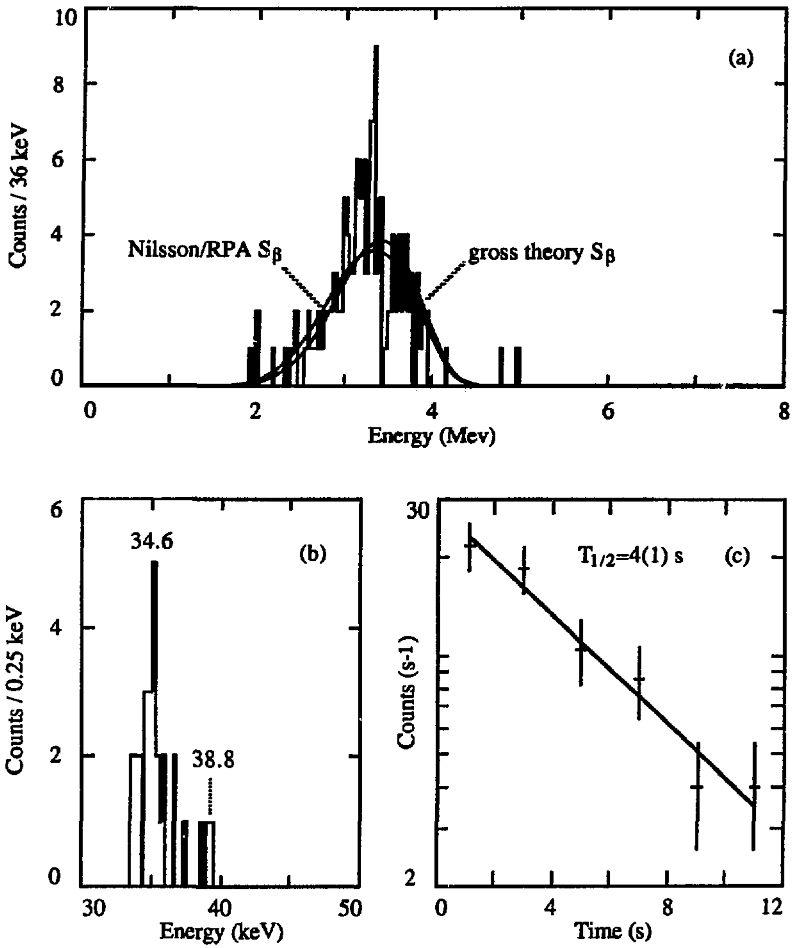

Figure 4.5. Decay of ^{128}Pr; (a) beta-delayed proton spectrum, (b) proton coincident x-ray spectrum, and (c) decay of the proton activity. The smooth curves in (a) are the results of statistical model calculations using the indicated beta-strength functions.

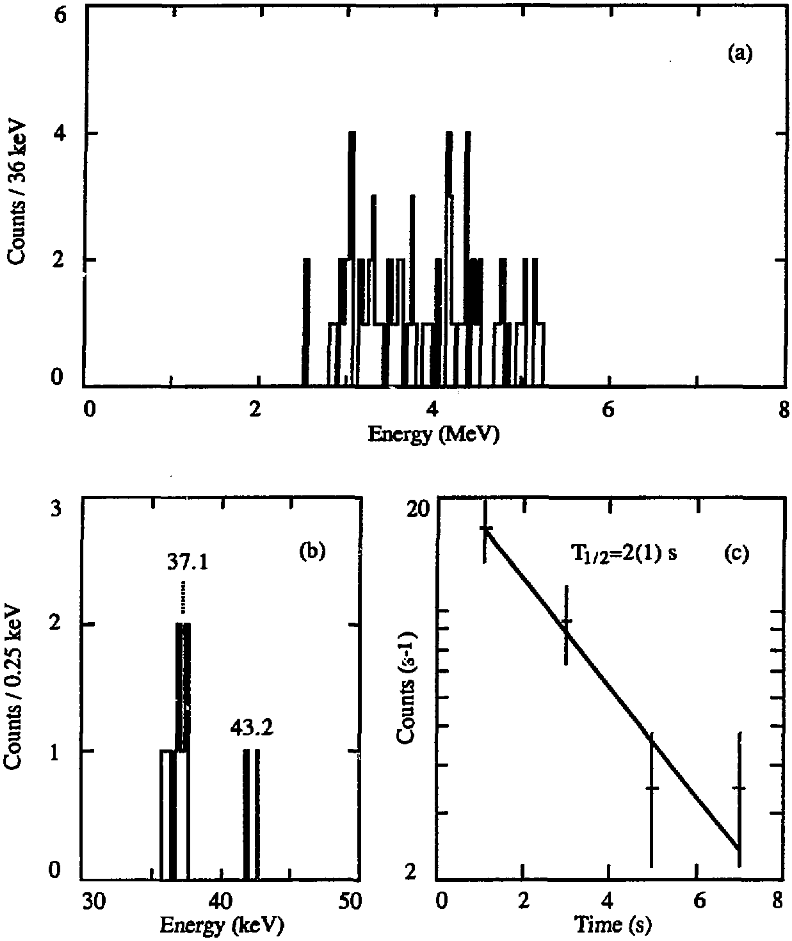

Figure 4.6. Decay of ^{130}Pm; (a) beta-delayed proton spectrum, (b) proton coincident x-ray spectrum, and (c) decay of the proton activity. The energy scale for the protons is only approximate, see text for details.

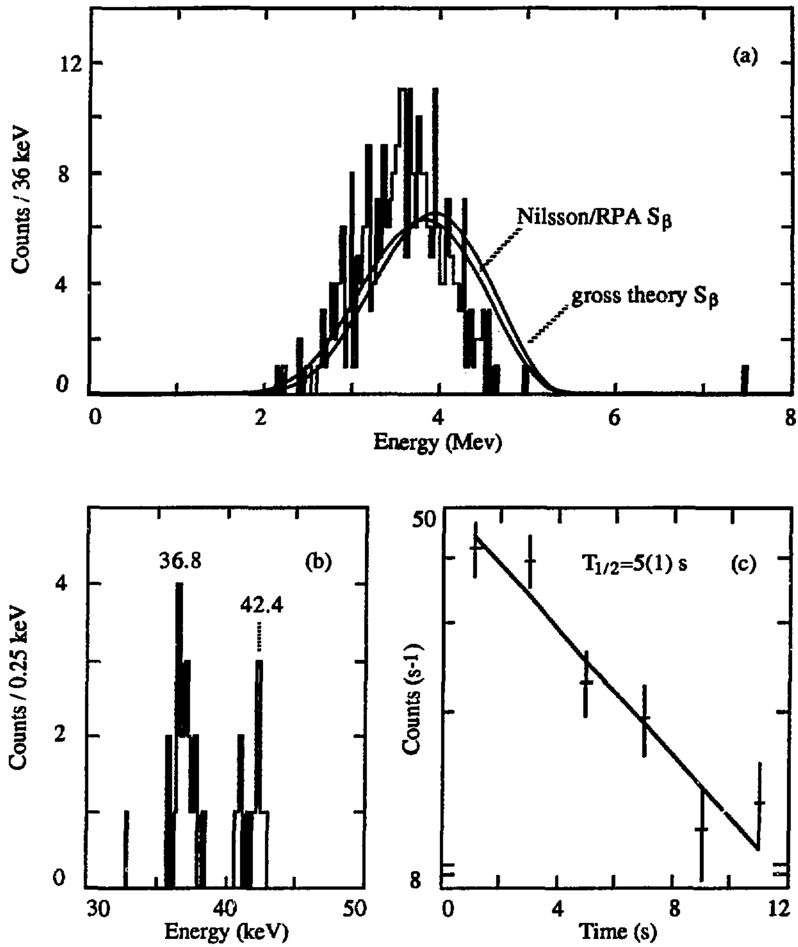

Figure 4.7. Decay of ^{132}Pm; (a) beta-delayed proton spectrum, (b) proton coincident x-ray spectrum, and (c) decay of the proton activity. The smooth curves in (a) are the results of statistical model calculations using the indicated beta-strength functions.

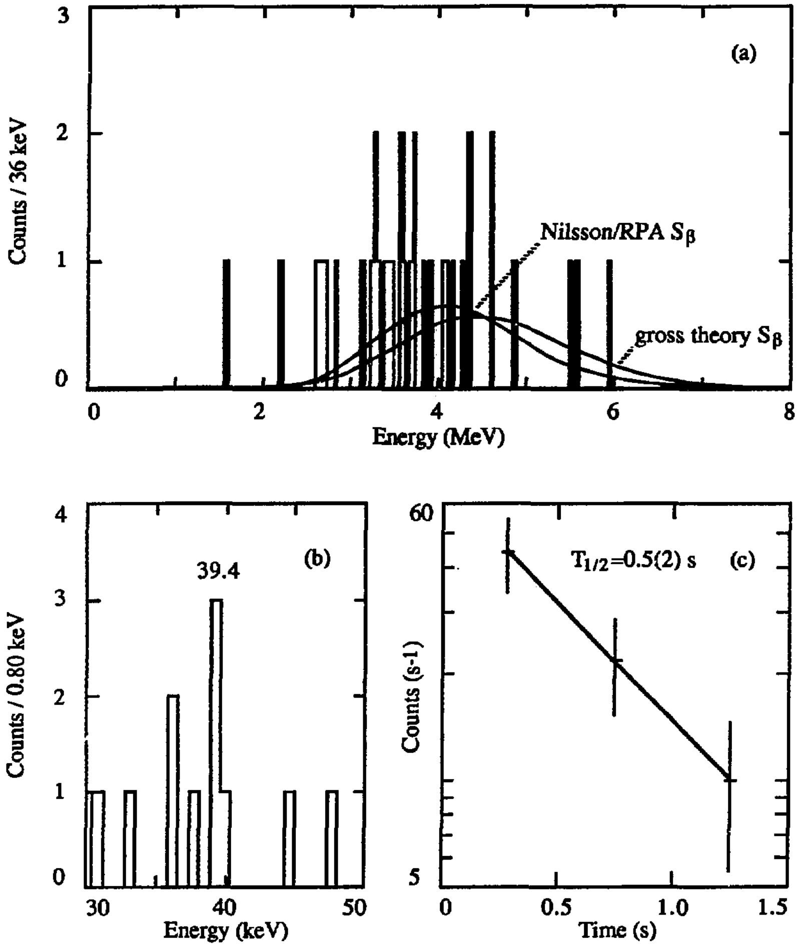

Figure 4.8. Decay of ^{134}Eu; (a) beta-delayed proton spectrum, (b) proton coincident x-ray spectrum, and (c) decay of the proton activity. The smooth curves in (a) are the results of statistical model calculations using the indicated beta-strength functions.

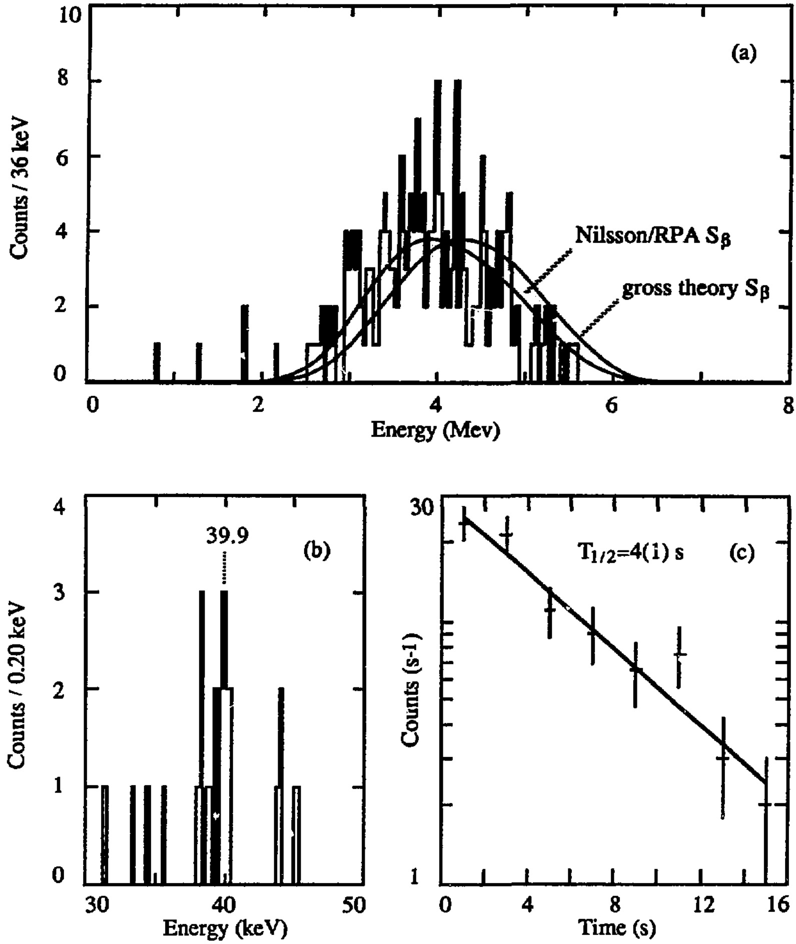

Figure 4.9. Decay of ^{136}Eu; (a) beta-delayed protons, (b) proton coincident x rays, and (c) decay of the proton activity. The smooth curves in (a) are the results from statistical model calculations.

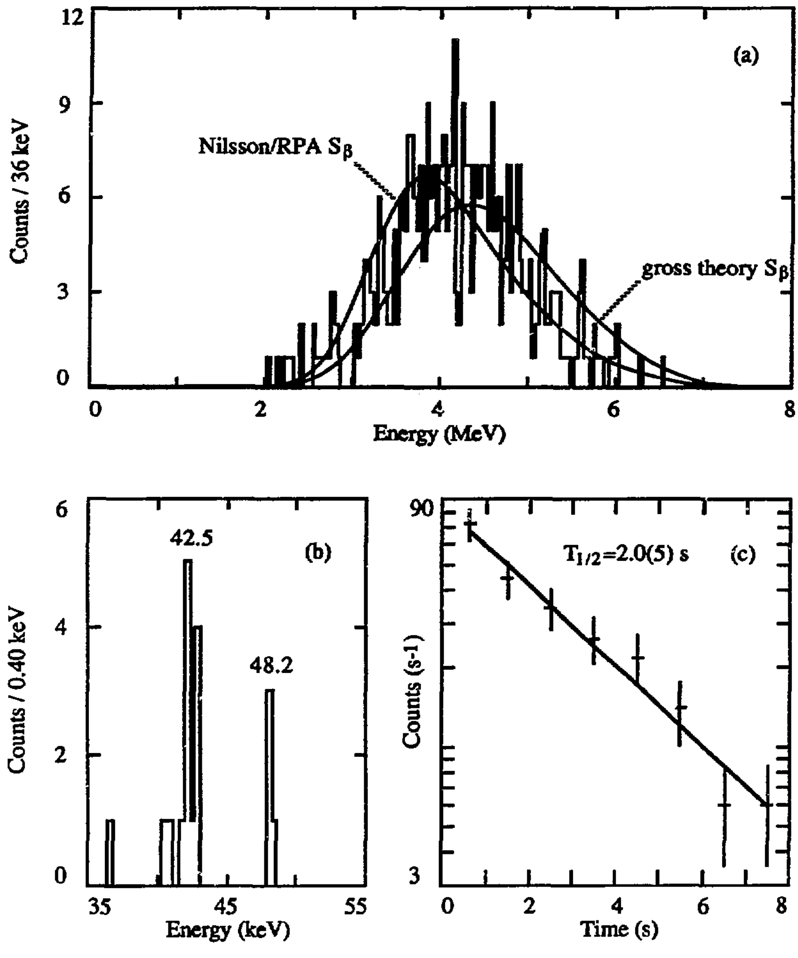

Figure 4.10. Decay of ^{140}Tb; (a) beta-delayed proton spectrum, (b) proton coincident x-ray spectrum, and (c) decay of the proton activity. The smooth curves in (a) are the results of statistical model calculations using the indicated beta-strength functions.

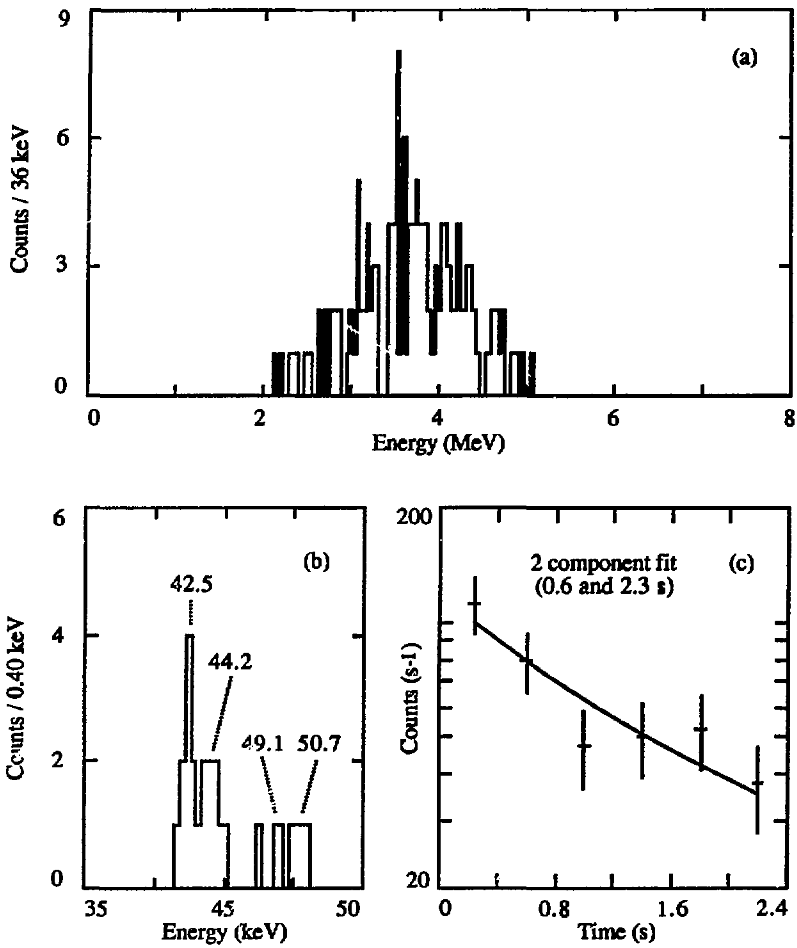

Figure 4.11. Decay of ^{142}Tb (and ^{142}Dy); (a) beta-delayed proton spectrum, (b) proton coincident x-ray spectrum, and (c) decay of the proton activities. The spectrum in (a) is only ~33% ^{142}Tb decay, see text for details.

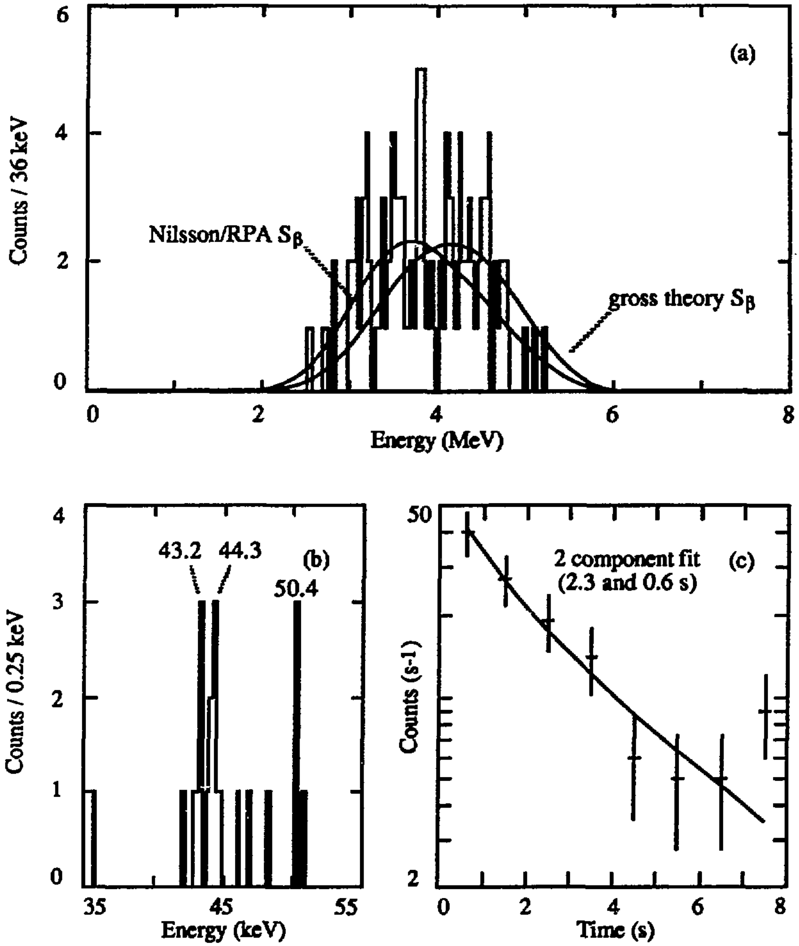

Figure 4.12. Decay of ^{142}Dy (and ^{142}Tb); (a) beta-delayed proton spectrum, (b) proton coincident x-ray spectrum, and (c) decay of the proton activities. The smooth curves in (a) are the results of statistical model calculations for ^{142}Dy using the indicated beta-strength functions. See text for details.

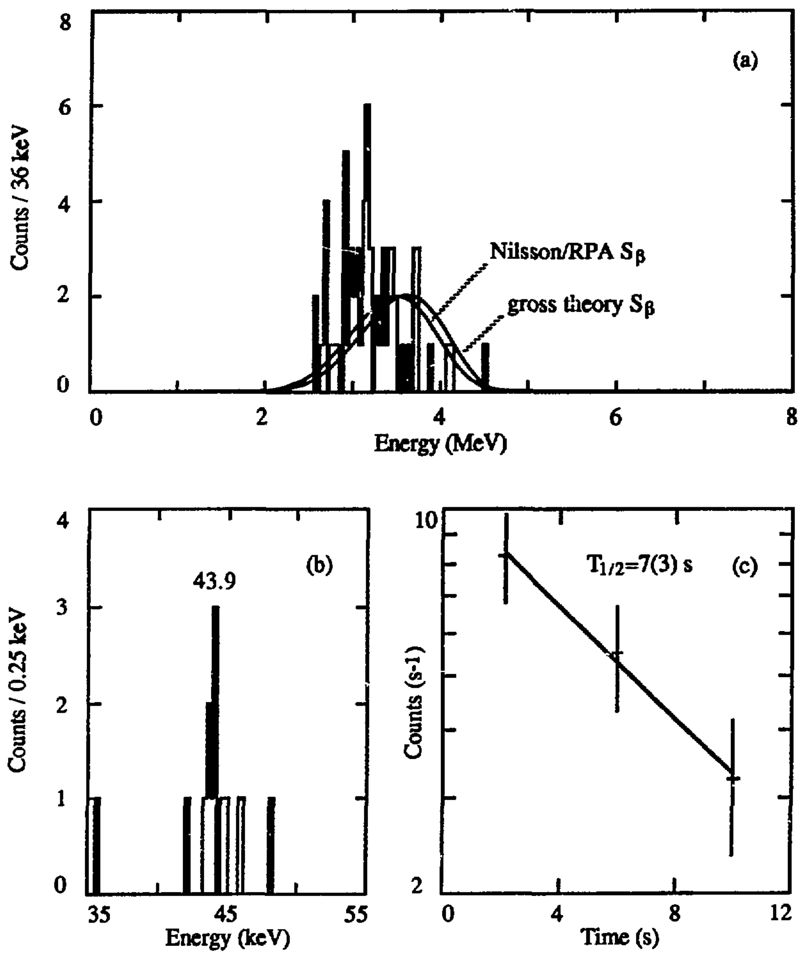

Figure 4.13. Decay of ^{144}Dy; (a) beta-delayed proton spectrum, (b) proton coincident x-ray spectrum, and (c) decay of the proton activity. The smooth curves in (a) are the results of statistical model calculations using the indicated beta-strength functions.

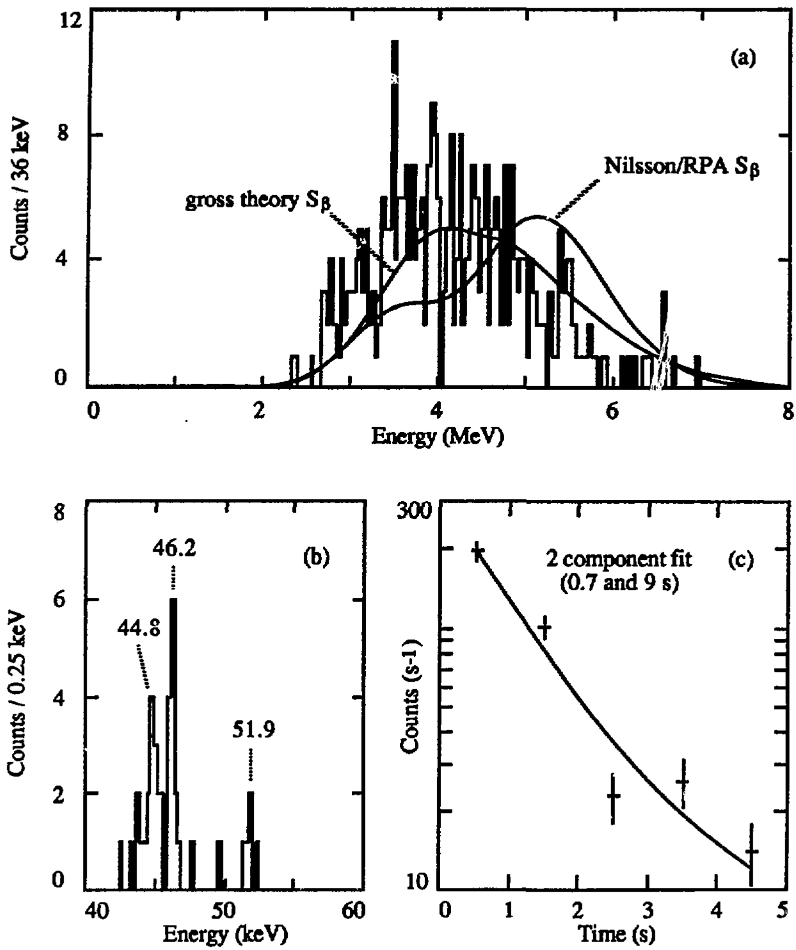

Figure 4.14. Decay of ^{144}Ho (and ^{144}Dy); (a) beta-delayed proton spectrum, (b) proton coincident x-ray spectrum, and (c) decay of the proton activities. The smooth curves in (a) are the combined results of statistical model calculations for both precursors using the indicated beta-strength functions. See text for details.

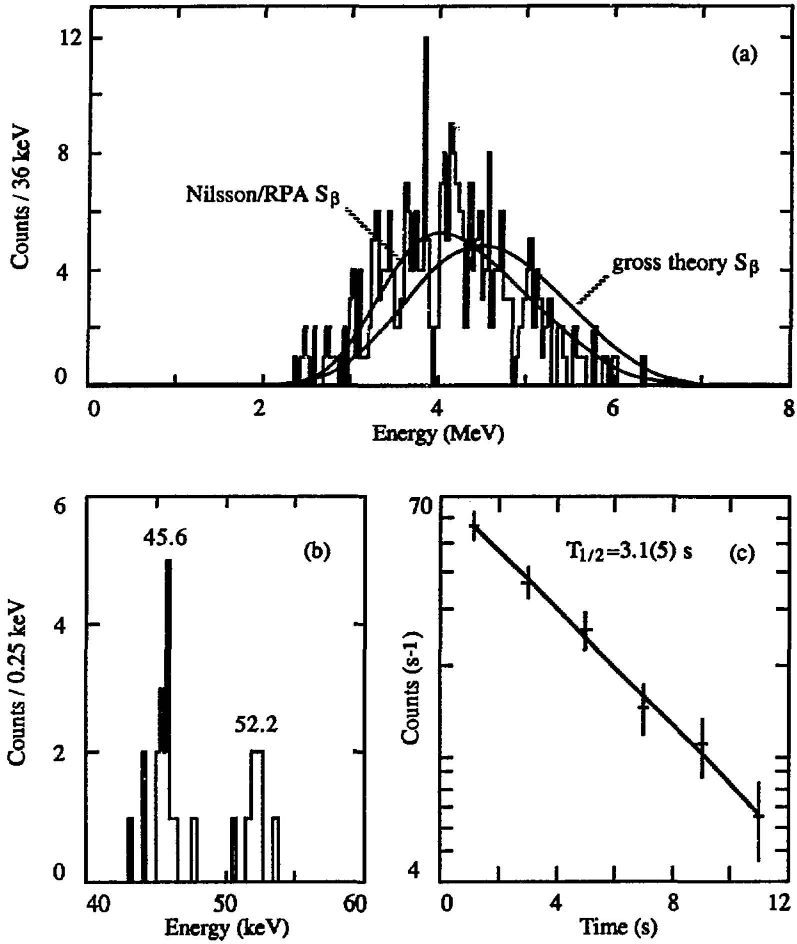

Figure 4.15. Decay of ^{146}Ho; (a) beta-delayed proton spectrum, (b) proton coincident x-ray spectrum, and (c) decay of the proton activity. The smooth curves in (a) are the results of statistical model calculations using the indicated beta-strength functions.

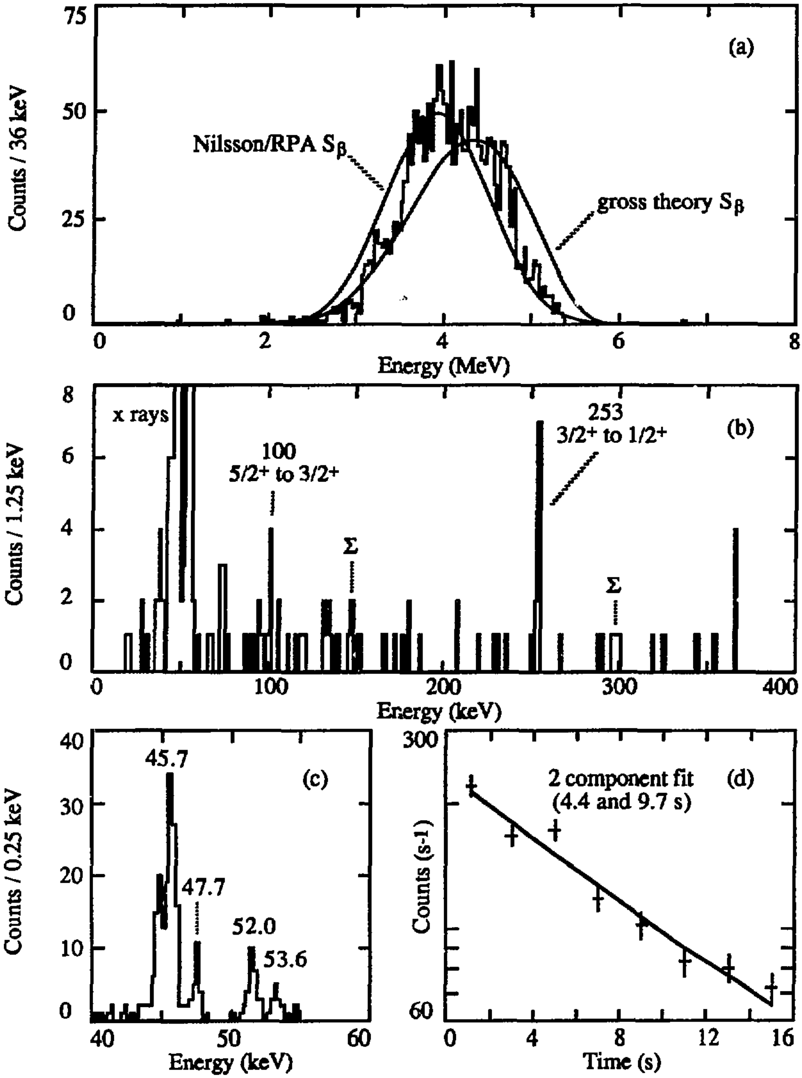

Figure 4.16. Decay of ^{148}Ho (and ^{148}Er); (a) beta-delayed proton spectrum, (b) proton coincident gamma-ray spectrum, (c) proton coincident x-ray spectrum, and (d) decay of the proton activities. The smooth curves in (a) are the results of statistical model caculations for ^{148}Ho using the indicated beta-strength functions (see text).

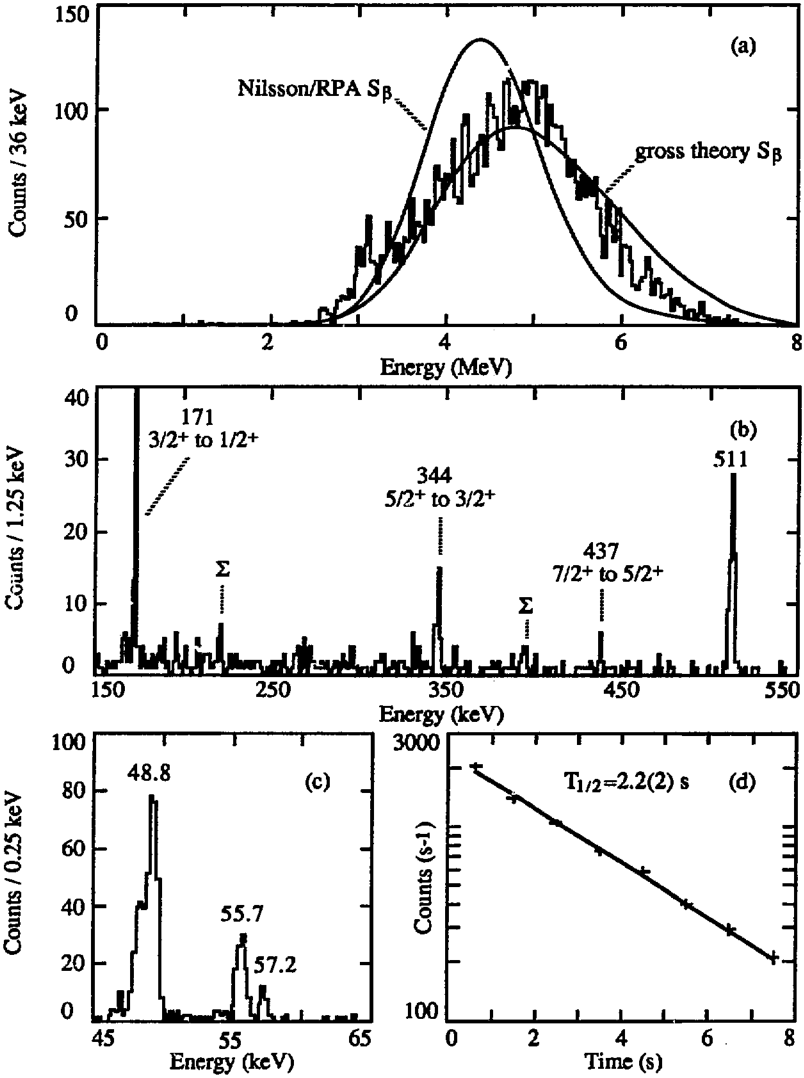

Figure 4.17. Decay of ^{150}Tm; (a) beta-delayed proton spectrum, (b) proton coincident gamma-ray spectrum, (c) proton coincident x-ray spectrum, and (d) decay of the proton activity. The smooth curves in (a) are the results of statistical model calculations using the indicated beta-strength functions.

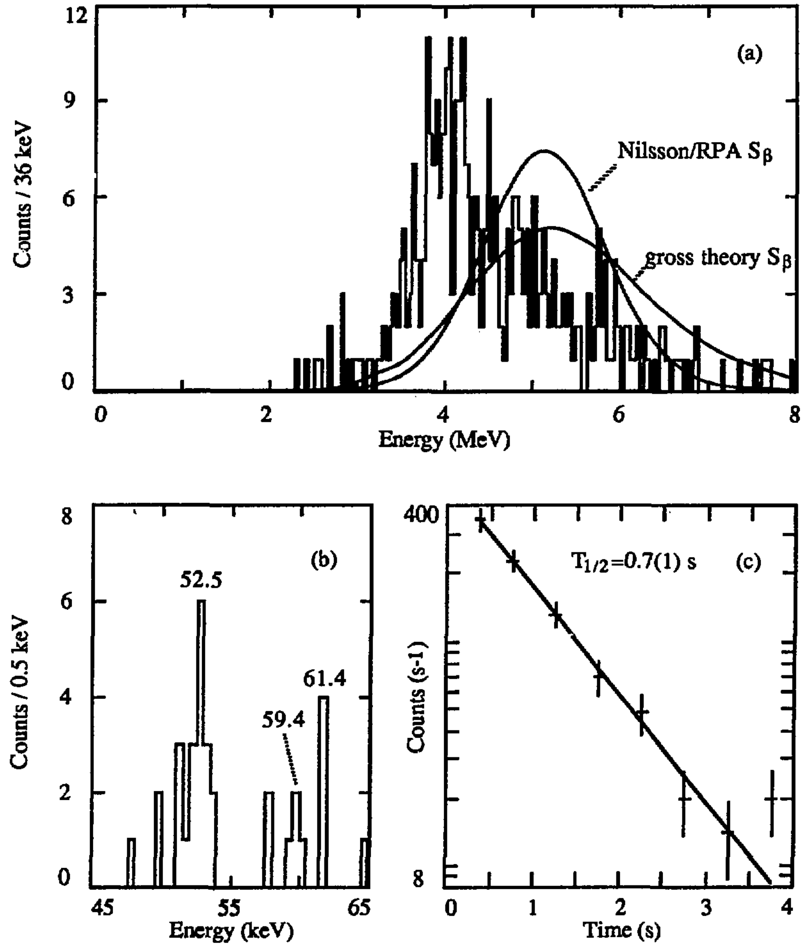

Figure 4.18. Decay of ^{152}Lu; (a) beta-delayed proton spectrum, (b) proton coincident x-ray spectrum, and (c) decay of the proton activity. The smooth curves in (a) are the results of statistical model calculations using the indicated beta-strength functions.

5. ODD MASS PRECURSORS

5.1. GENERAL

Twenty-two precursors with odd mass numbers have been studied; 21 of the precursors were even-odd and one was odd-even. For all even-odd precursors, final state branches were determined from the intensities of proton coincident γ rays. The reactions, calculated cross sections, detector configurations, and dates when the bombardments were performed are listed in Table 5.1.

Half-life related information for the delayed proton activities is given in Table 5.2, delayed proton information for each precursor is summarized in Table 5.3, and input parameters for statistical model calculations are given in Table 5.4. All three tables are similar to the corresponding Tables in chapter 4. The measured final state branches for precursors with $Z<64$ are listed in Table 5.5 along with the calculated values from statistical model calculations. The calculations used Nilsson/RPA β-strength functions and masses from [Lir76]. Final state branches for precursors with $Z\geq64$ are presented in Table 5.6. In even-odd isotopes in the region $Z\geq64$ and $N\leq82$, $1/2^+$ and $11/2^-$ isomer pairs are well established [Tot87d] and calculations (using Nilsson/RPA S_β's and [Lir76] masses) for these spins are also listed in Table 5.6. In most cases, a mixture of 1/2+ and 11/2- precursor spins (the last column) results in much improved agreement with experiment.

The experimental results are presented in figures 5.1 though 5.20 which have a format similar to the figures in chapter 4. The delayed proton spectra are plotted from 0 to 8 MeV at 36 keV per channel in the deformed region and at 18 keV per channel for precursors near N=82. The statistical model calculated proton spectra shown in the figures correspond to the precursor spins given in Table 5.4 (or combination of spins deduced from Table 5.6). Proton coincident γ-ray spectra (with the peaks labeled by energy) are shown for most precursors. The transitions in the proton daughter nuclei associated with the γ rays are also shown. Sum peaks in the coincident γ-ray spectra are denoted by a Σ.

5.2. DISCUSSION OF INDIVIDUAL PRECURSORS

^{119}Ba: This isotope was first identified in [Bog75] with a more complete study of its delayed proton decay reported in [Bog78a]. The data shown in Fig. 5.1

confirm the half-life and Z assignment of the earlier work and the proton coincident γ rays indicate a precursor spin of $1/2^+$.

^{123}Ce: The discovery of this precursor was first reported in [Nit84] and is shown in Fig. 5.2. From the final state feedings in Table 5.5, a $5/2^+$ precursor spin could be determined. The half-life for ^{123}Ce has been confirmed in a recent study of its β decay [Gen87].

^{125}Ce: The identification and half-life determination of ^{125}Ce was first reported in [Bog78b] and its delayed proton branch first measured in [Nit83b]. The results of a much improved study [Wil86] are shown in Fig. 5.3 and, from Table 5.5, a precursor spin of $5/2^+$ seems most likely. Preliminary results from studies of ^{125}Ce β decay [Gil87, Gen87] have confirmed the half-life of 9.8(8) s from the delayed proton studies.

^{127}Nd: Figure 5.4 shows the delayed proton decay of ^{127}Nd [Nit83b, Wil86]. A γ ray of 170 keV was observed in coincidence with the protons and confirms the first 2^+ to 0^+ transition in ^{126}Ce [Lis85]. The final state feedings are most consistent with a low-spin ($1/2^+$) precursor.

^{129}Nd: A β-delayed proton activity with a half-life of 5.9(6) s at this mass was previously assigned to ^{129}Nd [Bog77] based on systematics for delayed proton emission. Subsequently, the Z assignment was confirmed and proton coincident γ rays measured in [Wil85]. The data are presented in Fig. 5.5. A comparison of the final state branches with statistical model calculations in Table 5.5 indicates that a precursor spin of $5/2^+$ is the most compatible with the experiment.

A=131: Delayed protons from ^{131}Nd, previously reported in [Wil86, Bog77], from a ^{94}Mo(^{40}Ca,2pn) reaction are shown in Fig. 5.6. A 1.2(2) s delayed proton activity coincident with Pm K x-rays, observed in a ^{96}Ru(^{40}Ca,2p3n) bombardment (which also produced ^{131}Nd), was identified as ^{131}Sm [Wil86] and is shown in Fig. 5.7. The final state feedings in Table 5.5 suggest a $5/2^+$ spin for ^{131}Nd but ^{131}Sm shows relatively strong feeding of both the 0^+ and 4^+ levels in ^{130}Nd. A single precursor spin cannot reproduce this feeding pattern which may indicate a low- and high-spin isomer pair in ^{131}Sm. A 75% $1/2^+$, 25% $11/2^-$ precursor combination gives calculated final state branches of 36%(0^+), 41%(2^+), 17%(4^+), and 6%(6^+) which are in much better agreement with the measured values. However, the 0^+ feeding, which is determined from the difference in the total number of protons and the number feeding excited states, is dependent on the subtraction of the ^{131}Nd activity to determine the proton intensity associated with ^{131}Sm. A reduction in the total number of protons from ^{131}Sm would decrease the

0^+ branch and raise the 4^+ and 2^+ branches which would then be more consistent *with a 7/2 assignment. Due to this ambiguity, a spin of* $5/2^+$ *for* ^{131}Sm *was used in* the statistical model calculations shown in Fig. 5.7.

^{133}**Sm:** Delayed proton emission from ^{133}Sm was first reported in [Bog77] and later studied in more detail [Wil85] where proton coincident γ rays and x rays were measured. The data are shown in Fig. 5.8. From Table 5.5, a precursor spin of $3/2^+$ gives the best agreement with experiment but other precursor spins (1/2 or 5/2) cannot be ruled out.

^{135}**Sm:** Delayed proton emission from ^{135}Sm was first observed in [Bog77]. The results of the present experiments are shown in Fig. 5.9. Beta-decay studies [Gil87, Vie88a] indicate a high-spin (~$11/2^-$) isomer with a half-life similar to that of the delayed protons but the final state feedings are more consistent with a lower-spin precursor such as 3/2 or 5/2. This discrepancy cannot be resolved with the present data and a spin of $5/2^+$ was used in the statistical model results shown in Fig. 5.9.

^{137}**Gd and** ^{139}**Gd:** Both isotopes were first reported in [Nit83b] from experiments completed prior to the construction of the tape system. The precursor Z assignments were based on systematics and predicted cross sections; no additional studies have been performed. The proton spectra are shown in Fig. 5.10. The half-life for ^{139}Gd has been recently confirmed [Bér88] in a study of its β decay.

A=141: Two delayed proton precursors, ^{141}Gd and ^{141}Dy [Nit84, Wil86], have been identified at this mass number and are shown in Figs. 5.11 and 5.12, respectively. The β decay of ^{141}Gd was first studied in [Red86] and additional results have been recently reported [Tur87, Gil87]. There is an $11/2^-$ isomer located 378 keV above the $1/2^+$ ground state; both states β decay and have similar half-lives. The delayed proton half-life is consistent with the $1/2^+$ ground state value and the final state branches in Table 5.6 support the $1/2^+$ precursor assignment.

The final state feedings for ^{141}Dy are more consistent with a combination of $1/2^+$ and $11/2^-$ precursors but additional evidence of an isomer pair could not be found. The calculated proton spectra in Fig. 5.12(a) originate from a mixture of precursors with spins of $1/2^+$ and $11/2^-$.

^{143}**Dy:** Figure 5.13 shows the result of ^{143}Dy [Nit83b, Nit84] delayed proton decay. The proton coincident γ rays suffered from poor resolution and the 2^+ to 0^+ transition at 515 keV was difficult to resolve from the 511 annihilation radiation but the final state feedings in Table 5.6 suggest a $1/2^+$, $11/2^-$ isomer pair. The calculated proton spectra in Fig. 5.13(a) are from a combination of $1/2^+$ and $11/2^-$

precursors in the relative proportions that gave the best agreement with the final state feedings.

A=145: The delayed proton branch in ^{145}Dy was first reported in [Sch84b] but coincident x and γ rays were not measured. This decay was reinvestigated and the results are shown in Fig. 5.14. There is an $11/2^-$ isomer (at an excitation energy of ~120 keV) above the $1/2^+$ ground state. The final state feedings seem to indicate an equal mixture of both precursors whereas the 8 s half-life of the protons is the same as the $1/2^+$ ground state half-life; a 50% admixture of an ~14 s $11/2^-$ isomer [Nol82b, Alk82] would result in a proton half-life longer than 8 s. Analysis of the β-decay data is in progress and may help clear up this discrepancy.

The delayed proton precursor ^{145}Er was identified for the first time with a half-life of ~0.9 s (see Fig. 5.15). The low production cross section made it impossible to obtain a clean ^{145}Er proton spectrum. Even at the shortest cycle times, a significant fraction of the protons were due to ^{145}Dy decay. The proton spectrum in Fig. 5.15(a), obtained from a subtraction of the ^{145}Dy contribution, should, therefore, be considered as a qualitative rather than quantitative representation of the ^{145}Er delayed proton distribution. The final state feedings suggest the delayed proton decay originates predominantly from a high-spin precursor ($11/2^-$) but the existence of a $1/2^+$ precursor cannot be ruled out.

A=147: The delayed proton precursor ^{147}Dy (N=81), shown in Fig. 5.16, has been the focus of many studies [Kle82, Sch84a, Sch84b, Tot84a, Tot84b, Alk86, Nit87, Sch87] because of the pronounced structure in its delayed proton spectrum. The proton spectrum is associated with the decay of the $1/2^+$ ground state only and the nature of the structure will be discussed in the next chapter. Even though the assumptions of the statistical model appear to be invalid in this case, the results from such calculations are shown in Fig. 5.16(a).

A second delayed proton activity at this mass number, ^{147}Er [Sch84b, Tot87d], is shown in Fig. 5.17. From the final state feedings in Table 5.6, the $11/2^-$ isomer is the predominant precursor but there is a possible contribution from the $1/2^+$ ground state. The direct proton emission from ^{147}Tm [Kle82, Hof84, and references therein] can also be seen in Fig. 5.17(a).

A=149: The delayed proton results from a detailed study [Fir88] of ^{149m}Er and ^{149g}Er decays are shown in Fig. 5.18. Earlier studies of this N=81 even-odd precursor focused on the structure in the delayed proton spectrum [Sch84b, Tot84a, Tot84b] or single particle states in ^{149}Er and ^{149}Ho [Sch84a, Tot85]. Based on the observed final state feedings, about 30% of the delayed protons follow β decay of

^{149m}Er(11/2$^-$) with the remaining protons from ^{149g}Er(1/2$^+$) decay. The peak-like structure in the delayed proton spectrum is associated with ^{149g}Er decay and will be discussed in the following chapter. It is impossible to experimentally separate the delayed proton spectra of ^{149m}Er and ^{149g}Er and the calculations shown in Fig. 5.18(a) represent a mixture of both precursors.

Delayed proton emission was also observed in ^{149}Tm [Tot87c] but its proton spectrum could not be measured due to the intense ^{149}Er activity also present.

^{151}Yb: Delayed proton studies [Tot84a, Tot86] and β-decay studies [Kle85, Ako88] have been performed for this N=81 precursor which exhibits structure in its delayed proton spectrum [Fig. 5.19(a)] analogously to other N=81 even-odd precursors. In [Tot86] it was shown that the delayed proton spectrum is composed of a structureless component associated with the 11/2$^-$ isomer and a structured component due to the 1/2$^+$ ground state decay. This structure in N=81 precursors will be discussed in the next chapter.

^{153}Yb: A thorough report on the delayed proton branch in this isotope can be found in [Wil88] and the data are shown in Fig. 5.20 and Table 5.7.

Table 5.1. Reactions used to produce odd-mass delayed proton precursors; Thickness = target thickness, E_{HILAC} = beam energy at machine exit, E_{Target} = calculated beam energy at target center, σ = calculated cross section, Detectors = detector configuration used.

Isotope	Reaction	Thickness (mg/cm^2)	E_{HILAC} (MeV)	E_{Target} (MeV)	σ^a (mb)	Date^b	Detectors^c
^{119}Ba	^{58}Ni(^{64}Zn,2pn)	2	380	253	40	9/83	A
^{123}Ce	^{92}Mo(^{36}Ar,2p3n)	2	196	188	3	9/83	A
^{125}Ce	^{92}Mo(^{36}Ar,2pn)	2	165	153	80	4/86	B
^{127}Nd	^{92}Mo(^{40}Ca,2p3n)	2	223	208	1.5	2/85	B
^{129}Nd	^{92}Mo(^{40}Ca,2pn)	2	182	170	40	7/84	A
^{129}Nd	^{92}Mo(^{40}Ca,2pn)	2	184	172	40	10/84	A
^{131}Sm	^{96}Ru(^{40}Ca,2p3n)	0.6	288	208	0.6	2/85	B
^{131}Nd	^{96}Ru(^{40}Ca,4pn)	0.6	288	208	80	2/85	B
^{131}Nd	^{94}Mo(^{40}Ca,2pn)	2	180	168	60	2/85	B
^{133}Sm	^{96}Ru(^{40}Ca,2pn)	0.8	195	175	30	10/84	A
^{135}Sm	^{92}Mo(^{46}Ti,2pn)	2	204	192	80	11/86	C
^{141}Dy	^{92}Mo(^{54}Fe,2p3n)	2	292	276	0.7	10/83	A
^{141}Gd	^{92}Mo(^{54}Fe,4pn)	2	292	276	62	10/83	A
^{141}Dy	^{92}Mo(^{54}Fe,2p3n)	2	291	276	0.7	2/86	B
^{141}Gd	^{92}Mo(^{54}Fe,4pn)	2	291	276	62	2/86	B
^{141}Gd	^{92}Mo(^{52}Cr,2pn)	[illegible]	224	210	100	2/87	C
^{143}Dy	^{92}Mo(^{56}Fe,2p3n)	2	290	275	4	10/83	A
^{145}Er	^{92}Mo(^{58}Ni,2p3n)	2	325	297	0.2	3/88	C
^{145}Dy	^{92}Mo(^{58}Ni,4pn)	2	310	283	58	3/88	C
^{147}Er	^{92}Mo(^{58}Ni,2pn)	2	261	245	18	4/87	C
^{147}Dy	^{92}Mo(^{58}Ni,xpyn)^d	2	261	245	100	4/87	C
^{147}Dy	^{93}Nb(^{58}Ni,3pn)	2	268	250	100	10/86	C
^{149}Tm	^{94}Mo(^{58}Ni,p2n)	2	259	242	1.5	10/86	C
^{149}Er	^{94}Mo(^{58}Ni,2pn)	2	259	242	38	10/86	C
^{149}Er	^{94}Mo(^{58}Ni,2pn)	2	278	262	5	11/84	A
^{151}Yb	^{96}Ru(^{58}Ni,2pn)	0.8	275	248	8.5	11/84	A
^{151}Yb	^{96}Ru(^{58}Ni,2pn)	1.5	360	250	8.5	4/85	B
^{153}Yb	^{92}Mo(^{64}Zn,2pn)	2	285	267	45	12/87	C

[a] Calculated from [Win72].

[b] To indicate when more than one experiment was performed at a given isobaric chain and to correlate with entries in Table 5.2.

[c] The symbols A, B, and C refer to the detector configurations shown in Figure 3.3.

[d] Not produced directly. The cross section is the sum of all 3-particle reaction channels.

Table 5.2. Half-lives of odd-mass delayed proton precursors; Transit Time = tape transport time, Cycle Time = length of collection and counting interval, No. of Events = number of delayed protons at the respective counting cycle, $T_{1/2}$ Exp. = measured half-life, $T_{1/2}$ g.t. = predicted half-life from the gross theory of β decay, $T_{1/2}$ RPA = half-life from Nilsson/RPA β-strength function calculations.

Isotope	Date	Transit Time (s)	Cycle Time (s)[a]	No. of Events	$T_{1/2}$ Exp.[b] (s)	$T_{1/2}$ g.t.[c] (s)	$T_{1/2}$ RPA[d] (s)
^{119}Ba	9/83	0.07	10,50	14255,1263	6.0(3)	7.3	8.3
^{123}Ce	9/83	0.07	10	2611	3.8(2)	4.6	1.9
^{125}Ce	4/86	0.25	16	5487	9.8(8)	13.9	10.2
^{127}Nd	2/85	0.25	6	302	1.8(4)	3.0	1.7
^{129}Nd	10/84	0.25	12	1915	4.9(3)	8.3	6.8
^{131}Nd	2/85	0.25	24	2167[e]	25(5)	25.2	18.5
^{131}Sm	2/85	0.25	6	849[e]	1.2(2)	1.9	1.6
^{133}Sm	10/84	0.25	8	838	2.8(5)	5.5	3.5
^{135}Sm	11/86	0.07	16,40	475,148	10(2)	13.0	5.6
^{137}Gd[f]	12/82	--	-	358	7(3)	3.1	1.2
^{139}Gd[f]	12/82	--	-	315	5(1)	7.5	4.5
^{141g}Gd	2/87	0.07	128	426	23(3)	15.6	16.3
^{141}Dy	2/86	0.25	2.4,4	790[e],1180[e]	0.8(2)	1.8	1.4
^{143}Dy	10/83	0.07	10	1486	3.1(3)	4.1	2.9
^{145m,g}Dy	3/88	0.07	16,40	2251,673	8(1)	7.6	11.2
^{145}Er	3/88	0.07	1.6,4	1570[e],1223[e]	0.9(3)	1.2	0.7
^{147g}Dy	10/86	0.25	160	4699	~40[g]	22.5	32.9
^{147m,g}Er	4/87	0.07	1.28,4	3001,6817	2.6(2)	2.2	2.5
^{149m,g}Er	10/86	0.25	4,16	2099[e],9912	8.8(5)	4.8	3.2
^{149}Tm	10/86	0.25	4	2099[e]	0.9(2)[h]	1.6	0.9
^{151m,g}Yb	4/85	0.25	4	5745	1.6(1)	1.2	0.9
^{153}Yb	12/87	0.07	1.28,12.8	295,506	3.9(5)	13.6	8.9

[a] Decay curves are shown in Figures 4.19 to 4.38. When more than one tape cycle was used only the underlined cycle time is presented in the corresponding figure.

[b] Best value from all available proton data.

[c] Values from the gross theory [Tak73, Tak88] using the modified Lorentz strength function.

[d] From integrating β-strength functions from [Kru84] with a Gamow-Teller quenching factor of 0.5.

[e] Mixture of all delayed protons in this isobar.

[f] Data taken from [Nit83b].

[g] Fitted with half-lives for ^{147m}Dy and ^{147g}Dy from [Sch84b].

[h] Half-life is the value from β-delayed γ rays given in [Nit87] and references cited therein.

Table 5.3. Summary of the delayed proton decay of odd-mass precursors; Type = type of precursor: even-odd (eo) or odd-even (oe), T_z = 1/2(N-Z) precursor isospin projection, No. of Events = number of protons shown in Figures 5.1(a) to 5.20(a), Range = approximate lowest and highest observed proton energies, $\bar{x}$ = average proton energy, $\bar{w}$ = FWHM of proton distribution, P_p = measured proton branching ratio, J^π Exp.= deduced precursor spin and parity, J^π Calc. = predicted precursor spin and parity from [See75]

Isotope	Type	T_z	No. of Events	Range (MeV)	$\bar{x}$ (MeV)	$\bar{w}$ (MeV)	P_p	J^π Exp.	J^π Calc.
^{119}Ba	eo	7/2	15526	1.9,5.6	3.43(1)	1.55(1)	–	(1/2$^+$)	3/2$^+$
^{123}Ce	eo	7/2	2611	2.0,6.2	3.61(1)	1.66(3)	–	(5/2$^+$)	5/2$^+$
^{125}Ce	eo	9/2	5487	1.8,4.8	3.33(1)	1.28(2)	–	(5/2$^+$)	1/2$^+$
^{127}Nd	eo	7/2	302	2.2,6.0	3.66(4)	1.78(9)	–	–	1/2$^+$
^{129}Nd	eo	9/2	1916	1.9,5.5	3.66(2)	1.51(4)	–	(5/2$^+$)	5/2$^+$
^{131}Nd	eo	11/2	2167	1.8,4.2	3.13(1)	1.04(2)	–	(5/2$^+$)	5/2$^+$
^{131}Sm^a	eo	7/2	673	2.0,6.5	3.85(3)	1.81(7)	–	–	7/2$^-$
^{133}Sm	eo	9/2	836	2.0,6.2	3.77(5)	1.80(6)	–	–	5/2$^+$
^{135}Sm	eo	11/2	623	1.8,5.1	3.54(2)	1.36(6)	2(1)x10^{-4}	–	9/2$^-$
^{137}Gd^b	eo	9/2	358	2.2,6.7	3.83(5)	2.16(9)	–	–	9/2$^-$
^{139}Gd^b	eo	11/2	313	1.8,6.0	3.80(5)	1.86(9)	–	–	7/2$^+$
^{141g}Gd	eo	13/2	433	1.8,4.8	3.52(3)	1.26(6)	3(1)x10^{-4}	(1/2$^+$)	3/2$^-$
^{141}Dy^c	eo	9/2	790	2.3,7.1	4.14(3)	1.90(7)	–	–	7/2$^+$
^{143}Dy	eo	11/2	1487	2.2,6.8	4.17(2)	1.86(5)	–	–	3/2$^+$
^{145g}Dy	eo	13/2	2923	1.8,6.0	3.99(1)	1.69(3)	–	(1/2$^+$)	3/2$^+$
^{145m}Dy							–	(11/2$^-$)	–
^{145}Er^d	oo	9/2	839	2.5,7.6	4.34(3)	2.00(7)	–	–	3/2$^-$
^{147g}Dy	eo	15/2	4699	2.0,4.4	3.50(1)	1.03(2)	2(1)x10^{-3}	1/2$^+$	11/2$^-$
^{147g}Er^e	eo	11/2	5899	2.2,7.9	4.32((1)	1.96(3)	–	(1/2$^+$)	1/2$^-$
^{147m}Er							–	(11/2$^-$)	–
^{149g}Er	eo	13/2	9912	2.0,7.3	4.28(1)	1.87(2)	7(2)x10^{-2}	1/2$^+$	11/2$^-$
^{149m}Er							1.8(7)x10^{-3}	11/2$^-$	–
^{149}Tm	oe	9/2	–	–	–	–	–	(11/2$^-$)	11/2$^-$
^{151g}Yb	eo	11/2	5745	2.2,7.8	4.52(1)	1.92(3)	–	1/2$^+$	11/2$^-$
^{151m}Yb							–	11/2$^-$	–
^{153}Yb	eo	13/2	801	2.1,5.8	3.88(2)	1.53(5)	8(2)x10^{-5}	7/2$^-$	7/2$^-$

[a] Contribution from ^{131}Nd decay was subtracted.
[b] Data taken from [Nit83b].
[c] Proton spectrum contains less than 12% ^{141}Gd decay.
[d] Contribution from ^{145}Dy decay was subtracted.
[e] Contribution from ^{147}Dy decay was subtracted.

Table 5.4. Input parameters for statistical model calculations of odd-mass precursors; J^π = precursor spin and parity, Q_{EC} = β^+/EC decay energy, B_p = proton binding energy, Final States = references where energies, spins, and parities of levels in the final nucleus can be found. All calculations used level density parameters from [Dil73], optical model parameters from [Bec69], average radiation widths from [Har82], and gross theory or Nilsson/RPA β-strength functions (as indicated in Figures 5.1 to 5.20).

Isotope	J^π	Q_{EC}[a] (MeV)	B_p[a] (MeV)	Final States
^{119}Ba	1/2+	8.05	1.69	[Gen77, Ker84]
^{123}Ce	5/2+	8.53	1.47	[Con74, Gen87]
^{125}Ce	5/2+	7.27	2.20	[Con74, Gil87, Mar87]
^{127}Nd	1/2+	9.05	1.13	[Lis85]
^{129}Nd	5/2+	7.83	1.80	[War75]
^{131}Nd	5/2+	6.71	2.43	[Kor87, Tod84]
^{131}Sm	5/2+	9.60	0.72	[Lis85]
^{133}Sm	3/2+	8.43	1.35	[Lis85, Mak86, Bér87, Ker87b, Kor87, Wad87b, Wad88]
^{135}Sm	5/2+	7.35	1.96	[Bér87, Bil87, Ker87b, Kor87, Pau87, Wad87b, Vie88a, Wad88]
^{137}Gd	5/2+	9.04	0.91	[Lis85, Mak86, Bér87, Ker87a, Ker87b, Wad87b, Vie88a]
^{139}Gd	5/2+	8.01	1.51	[Cha85, Lis85, Mak86, Red86, Bér87, Ker87b, Pau87]
^{141g}Gd	1/2+	7.08	2.12	[Mar76, Ker87a, Ker87b, Sta87]
^{141}Dy	1/2+,11/2-	9.65	0.50	[Lis85, Bis88]
^{143}Dy	1/2+,11/2-	8.68	1.12	[Lun86, Gil87, Goe87, Sta87]
^{145}Dy	1/2+,11/2-	7.81	1.74	[Nol82b, Lac84, Red86]
^{145}Er	1/2+,11/2-	10.29	0.16	[Goe87]
^{147g}Dy	1/2+	6.55[b]	2.08[b]	[Jul80]
^{147}Er	1/2+,11/2-	9.39	0.79	[Gui82]
^{149g}Er	1/2+	8.40[c]	1.40[c]	[Dal78, Tot88]
^{149m}Er	11/2-	9.10[c]	1.40[c]	[Dal78, Tot88]
^{149}Tm	11/2-	9.76	2.58	[Bro84]
^{151g}Yb	1/2+	10.11	0.39	[Nol82a, Nol82b]
^{151m}Yb	11/2-	10.86[d]	0.39	[Nol82a, Nol82b]
^{153}Yb	7/2-	6.91	0.94	[Hor81, Nol82c, Tot87a]

[a] Reference [Lir76].
[b] Reference [Wap87].
[c] Reference [Fir88].
[d] Isomer assumed to be ~750 keV above ground.

Table 5.5. Comparison of experimental and calculated proton final state branches; Precursor → Daughter = delayed proton precursor and proton daughter, J^π = spin and parity of level in proton daughter, Energy = excitation energy of level in proton daughter, Exp. = measured branch to level in proton daughter, and calculated branches for various precursor spins.

Precursor → Daughter	J^π	Energy (keV)	Exp. (%)	1/2+ calc.	3/2+ calc.	5/2+ calc.	7/2+ calc.
^{119}Ba	0+	0	71(10)	60	46	21	–
→ ^{118}Xe	2+	337	29(5)	33	45	60	–
	4+	810	1(1)	1	1	9	–
^{123}Ce	0+	0	23(6)	–	37	14	9
→ ^{122}Ba	2+	197	66(6)	–	55	66	54
	4+	570	9(3)	–	3	14	32
	6+	1083	2(1)	–	–	–	1
^{125}Ce	0+	0	36(4)	–	49	20	14
→ ^{124}Ba	2+	197	53(4)	–	50	72	65
	4+	570	9(3)	–	1	8	21
	6+	1228	1(1)	–	–	–	–
^{127}Nd	0+	0	60(15)	50	37	14	–
→ ^{126}Ce	2+	170	35(13)	48	60	70	–
	4+	520	5(5)	2	3	16	–
^{129}Nd	0+	0	23(7)	–	44	17	12
→ ^{128}Ce	2+	207	68(7)	–	54	71	61
	4+	607	9(3)	–	2	12	27
^{131}Nd	0+	0	32(7)	–	57	26	20
→ ^{130}Ce	2+	254	67(7)	–	41	68	67
	4+	710	1(1)	–	1	4	11
^{131}Sm	0+	0	41(15)	47	35	13	7
→ ^{130}Nd	2+	158	36(15)	51	61	68	52
	4+	483	21(8)	2	4	19	39
	6+	938	3(3)	–	–	1	2
^{133}Sm	0+	0	35(9)	56	43	18	–
→ ^{132}Nd	2+	213	63(9)	43	54	70	–
	4+	611	1(1)	1	3	12	–
^{135}Sm	0+	0	42(13)	64	52	24	–
→ ^{134}Nd	2+	294	41(14)	31	41	61	–
	2+	754	10(6)	4	6	8	–
	4+	789	7(5)	–	1	5	–

Table 5.6. Comparison of experimental and calculated proton final state branches; Precursor → Daughter = delayed proton precursor and proton daughter, J^{π} = spin and parity of level in proton daughter, Energy = excitation energy of the level, Exp. = measured branch to the level, $1/2^{+}$ calc. = calculated final state branches for a $1/2^{+}$ precursor, $11/2^{-}$ calc. = caclulated final state branches for an $11/2^{-}$ precursor, Mixing = fractions (in percent) of $1/2^{+}$ and $11/2^{-}$ proton intensities that give improved final state branches, and Total calc. = combined calculated final state branches.

Precursor → Daughter	J^{π}	Energy (keV)	Exp. (%)	$1/2^{+}$ calc. (%)	$11/2^{-}$ calc. (%)	Mixing (%)	Total calc. (%)
^{141}Gd	0^{+}	0	79(11)	87	8	100/0	87
→ ^{140}Sm	2^{+}	530	21(10)	12	66		12
	4^{+}	1246	--	–	6		–
^{141}Dy	0^{+}	0	32(12)	60	1	57/43	34
→ ^{140}Gd	2^{+}	329	42(15)	39	26		34
	4^{+}	837	26(10)	1	61		27
	6^{+}	1465	–	–	12		5
^{143}Dy	0^{+}	0	24(10)	76	3	26/74	22
→ ^{142}Gd	2^{+}	515	34(12)	20	42		36
	2^{+}	980	11(3)	4	7		6
	4^{+}	1209	31(7)	–	42		31
	6^{+}	1964	–	–	4		3
^{145}Dy	0^{+}	0	56(8)	91	14	50/50	53
→ ^{144}Gd	2^{+}	743	44(8)	9	71		40
	4^{+}	1745	<2	–	11		5
^{145}Er	0^{+}	0	17(14)	67	2	20/80	15
→ ^{144}Dy	2^{+}	493	38(18)	33	38		37
	4^{+}	1165	44(12)	–	53		43
	6^{+}	1916	–	–	7		5
^{147}Er	0^{+}	0	19(6)	81	6	15/85	17
→ ^{146}Dy	2^{+}	683	54(7)	19	57		52
	4^{+}	1608	27(4)	–	30		25
	3^{-}	1783	<2	–	3		3
	5^{-}	2283	<2	–	3		2
^{149}Er	0^{+}	0	71(5)	99	24	70/30	76
→ ^{148}Dy	2^{+}	1678	4(3)	1	11		4
	3^{-}	1688	9(5)	-	31		9
	5^{-}	2349	5(3)	–	15		5
	4^{+}	2428	7(2)	–	10		3
	6^{+}	2732	2(1)	–	6		2

Table 5.6. *(Continued).*

Precursor / → Daughter	J^{π}	Energy (keV)	Exp. (%)	1/2+ calc. (%)	11/2- calc. (%)	Mixing (%)	Total calc. (%)
^{151}Yb	0^+	0	51(5)	95	5	50/50	51
→ ^{150}Er	2^+	1579	14(3)	3	10		7
	3^-	1786	10(1)	2	14		8
	5^-	2261	9(3)	-	18		9
	4^+	2295	11(3)	-	25		13
	6^+	2621	5(2)	-	19		9

Table 5.7. Experimental and calculated β-delayed proton branches from ^{153}Yb to levels in ^{152}Er. The precursor spin was assumed to be $7/2^-$ and calculations for three different forms of S_β are listed.

Levels in ^{152}Er		Final State Branches (%)			
J^{π}	Energy (keV)	Experiment	Gross Theory $7/2^-$	Nilsson/RPA $7/2^-$	Constant $7/2^-$
0^+	0	57(17)	50	66	49
2^+	808	40(12)	44	32	45
4^+	1481	3(3)	4	2	4

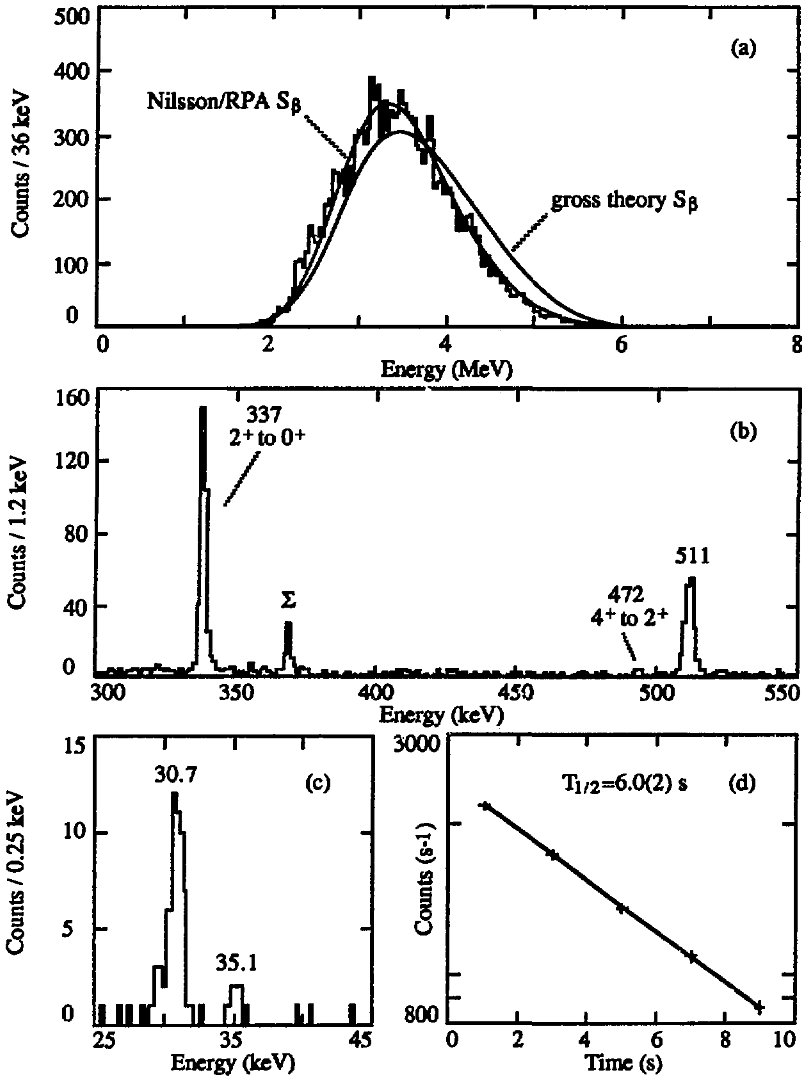

Figure 5.1. Decay of ^{119}Ba; (a) delayed proton spectrum, (b) proton coincident gamma-ray spectrum, (c) proton coincident x-ray spectrum, and (d) decay of the proton activity. The smooth curves in (a) are from statistical model calculations using the indicated beta-strength functions.

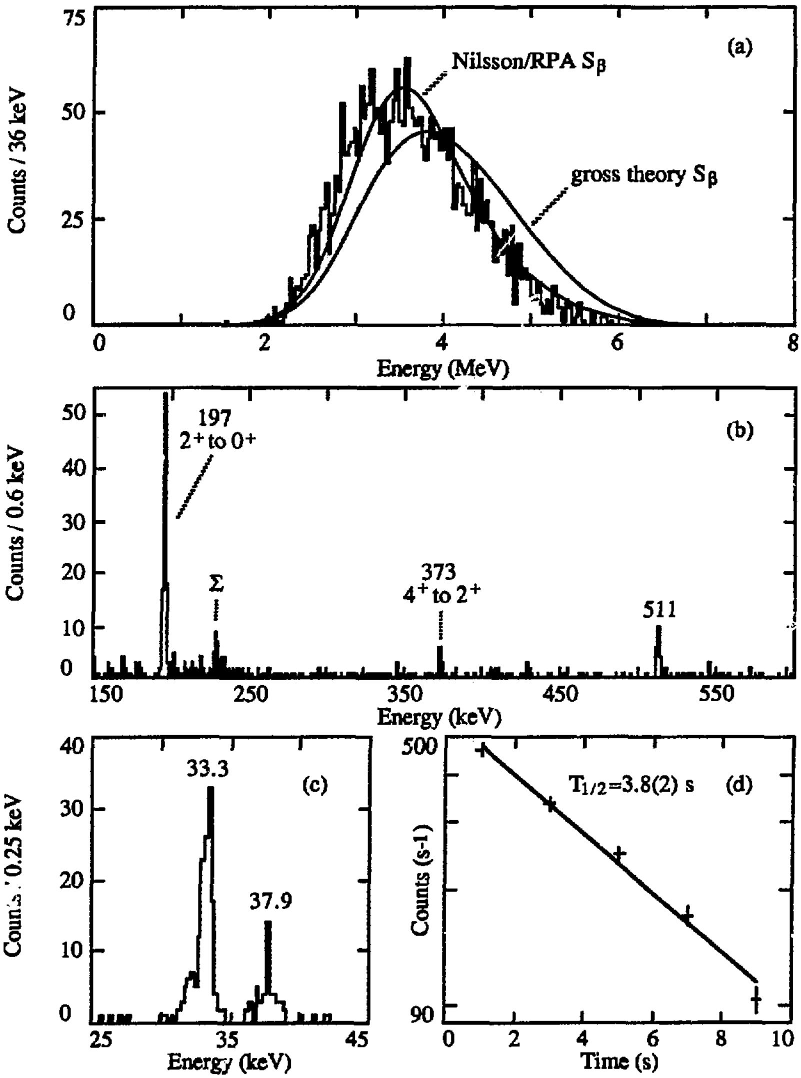

Figure 5.2. Decay of ^{123}Ce; (a) delayed proton spectrum, (b) proton coincident gamma-ray spectrum, (c) proton coincident x-ray spectrum, and (d) decay of the proton activity. The smooth curves in (a) are from statistical model calculations using the indicated beta-strength functions.

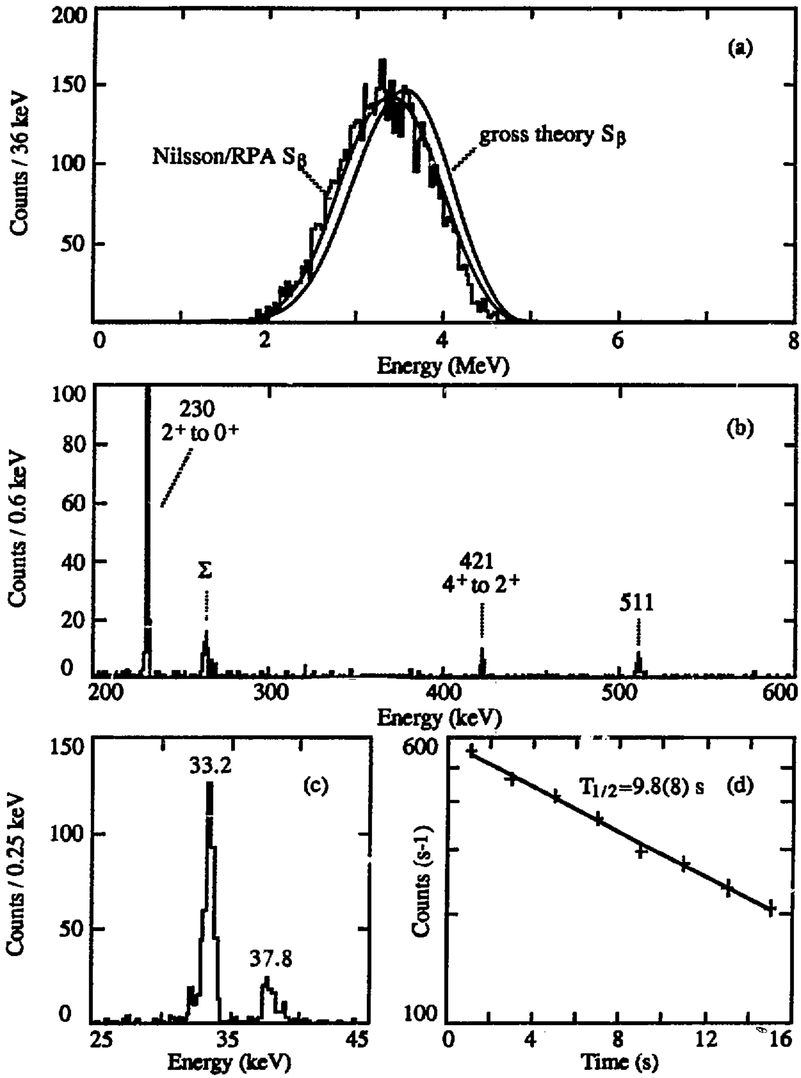

Figure 5.3. Decay of ^{125}Ce; (a) delayed proton spectrum, (b) proton coincident gamma-ray spectrum, (c) proton coincident x-ray spectrum, and (d) decay of the proton activity. The smooth curves in (a) are from statistical model calculations using the indicated beta-strength functions.

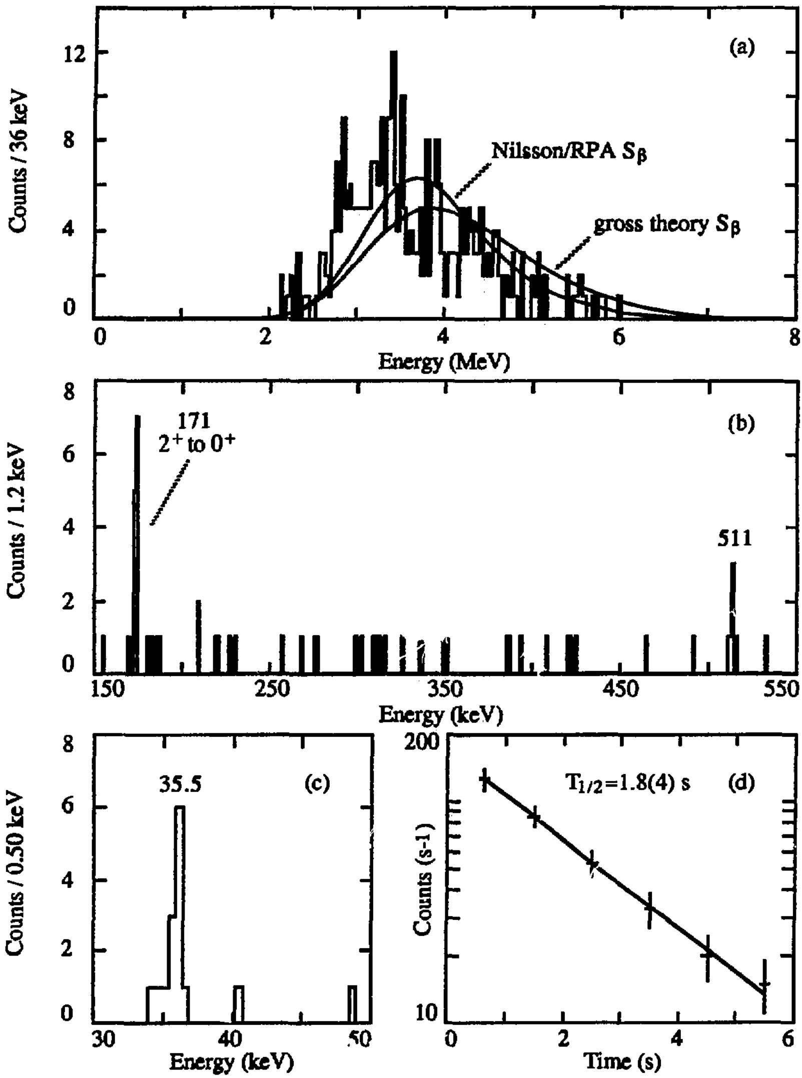

Figure 5.4. Decay of ^{127}Nd; (a) delayed proton spectrum, (b) proton coincident gamma-ray spectrum, (c) proton coincident x-ray spectrum, and (d) decay of the proton activity. The smooth curves in (a) are from statistical model calculations using the indicated beta-strength functions.

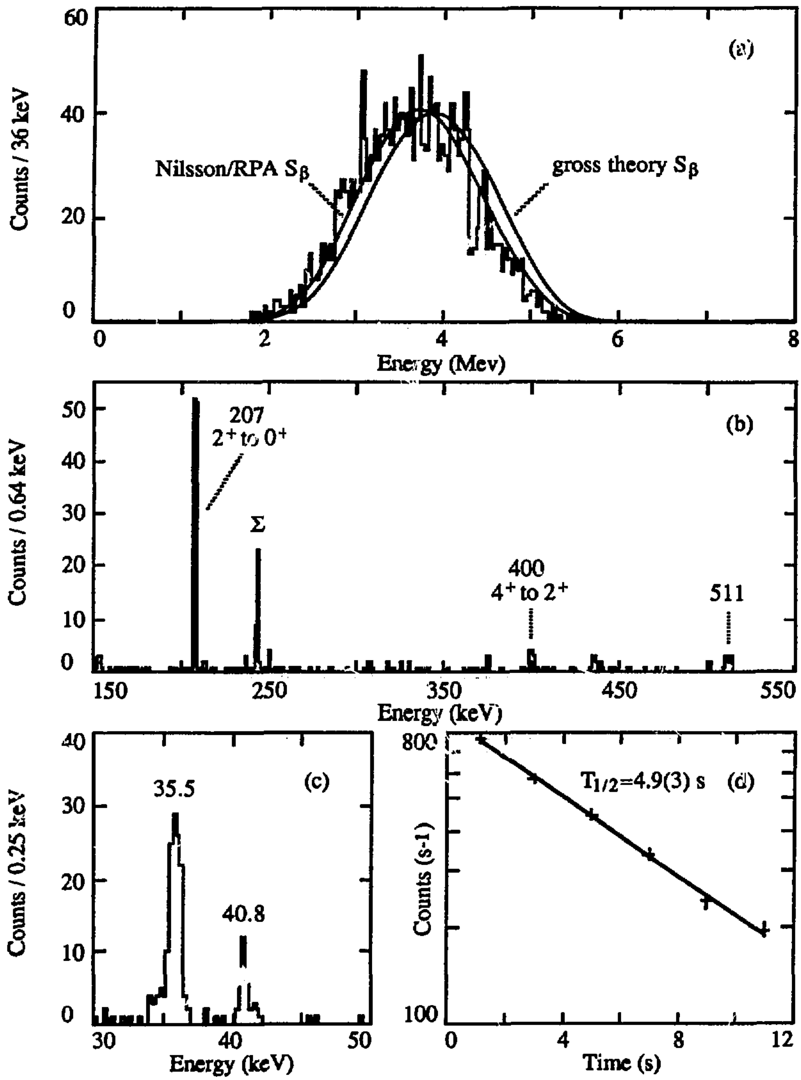

Figure 5.5. Decay of ^{129}Nd; (a) delayed proton spectrum, (b) proton coincident gamma-ray spectrum, (c) proton coincident x-ray spectrum, and (d) decay of the proton activity. The smooth curves in (a) are from statistical model calculations using the indicated beta-strength functions.

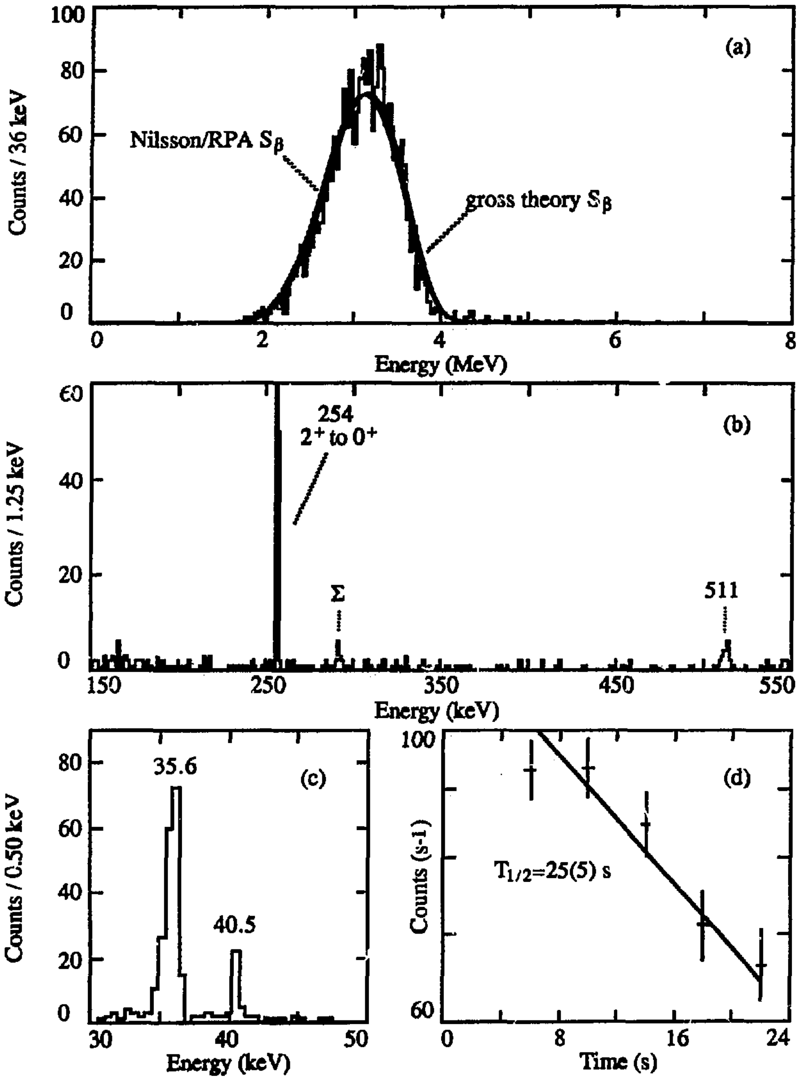

Figure 5.6. Decay of ^{131}Nd; (a) delayed proton spectrum, (b) proton coincident gamma-ray spectrum, (c) proton coincident x-ray spectrum, and (d) decay of the proton activity. The smooth curves in (a) are from statistical model calculations using the indicated beta-strength functions.

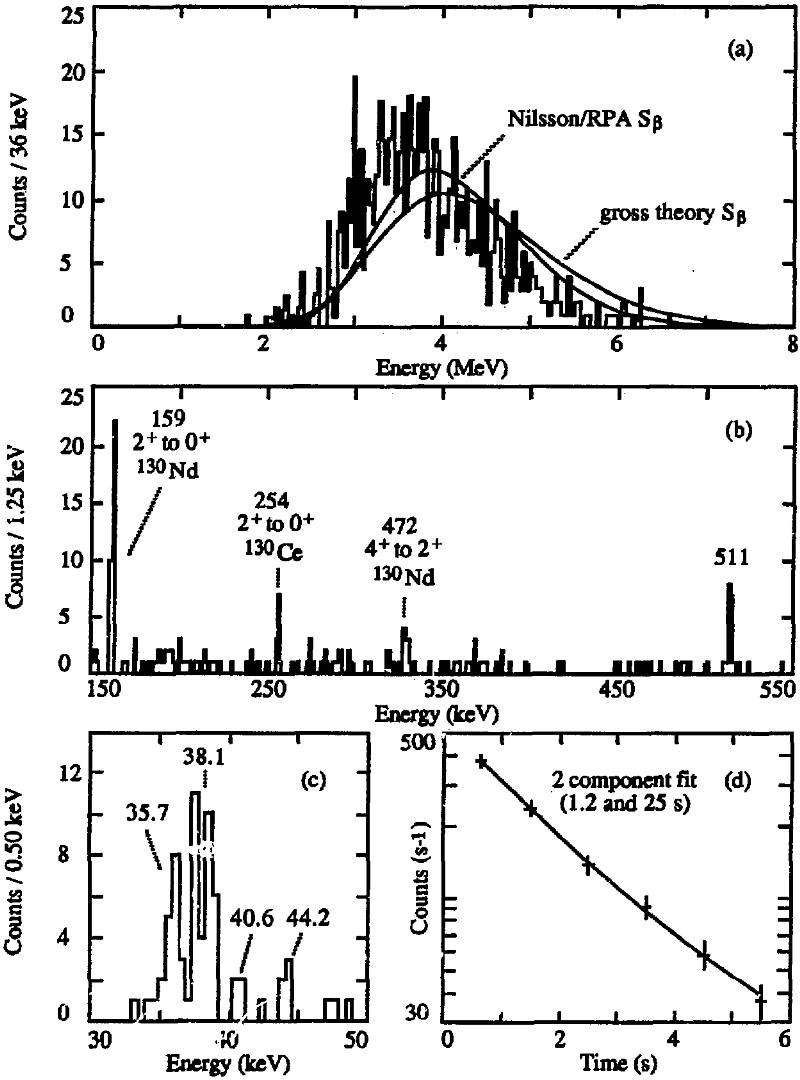

Figure 5.7. Decay of ^{131}Sm (and ^{131}Nd); (a) delayed proton spectrum, (b) proton coincident gamma-ray spectrum, (c) proton coincident x-ray spectrum, and (d) decay of the proton activity. The smooth curves in (a) are from statistical model calculations using the indicated beta-strength functions. Spectrum in part (a) was obtained after subtracting the ^{131}Nd contribution.

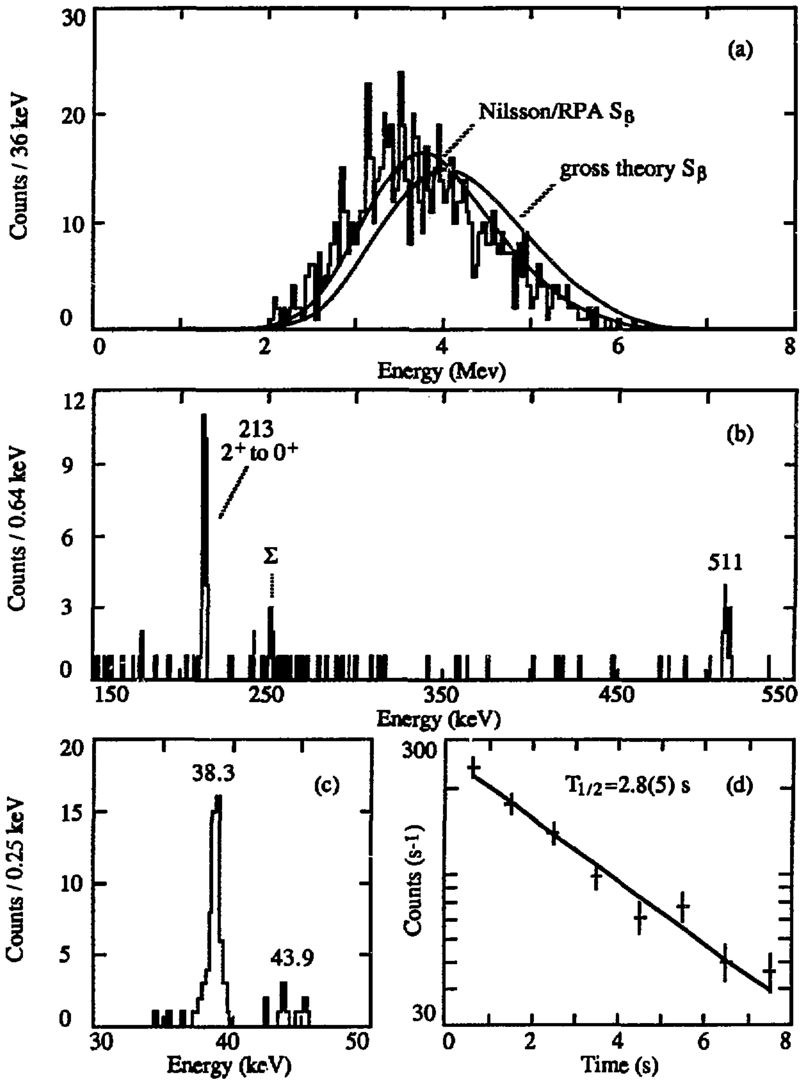

Figure 5.8. Decay of ^{133}Sm; (a) delayed proton spectrum, (b) proton coincident gamma-ray spectrum, (c) proton coincident x-ray spectrum, and (d) decay of the proton activity. The smooth curves in (a) are from statistical model calculations using the indicated beta-strength functions.

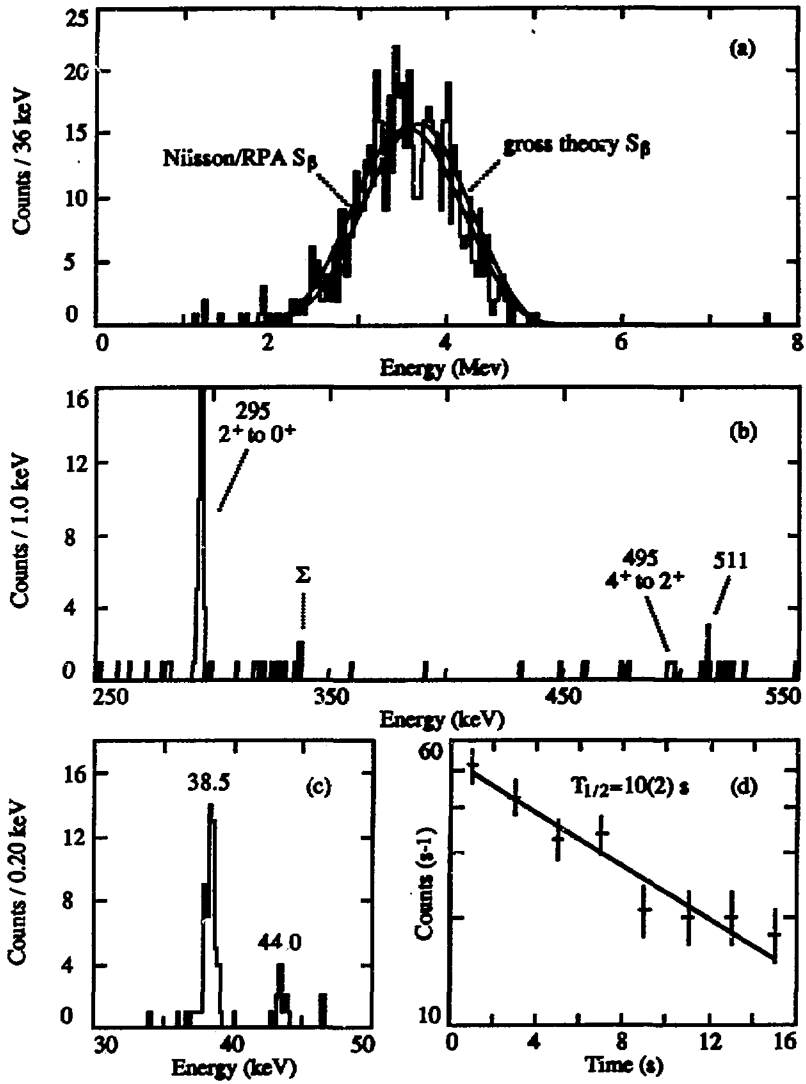

Figure 5.9. Decay of ^{135}Sm; (a) delayed proton spectrum, (b) proton coincident gamma-ray spectrum, (c) proton coincident x-ray spectrum, and (d) decay of the proton activity. The smooth curves in (a) are from statistical model calculations using the indicated beta-strength functions.

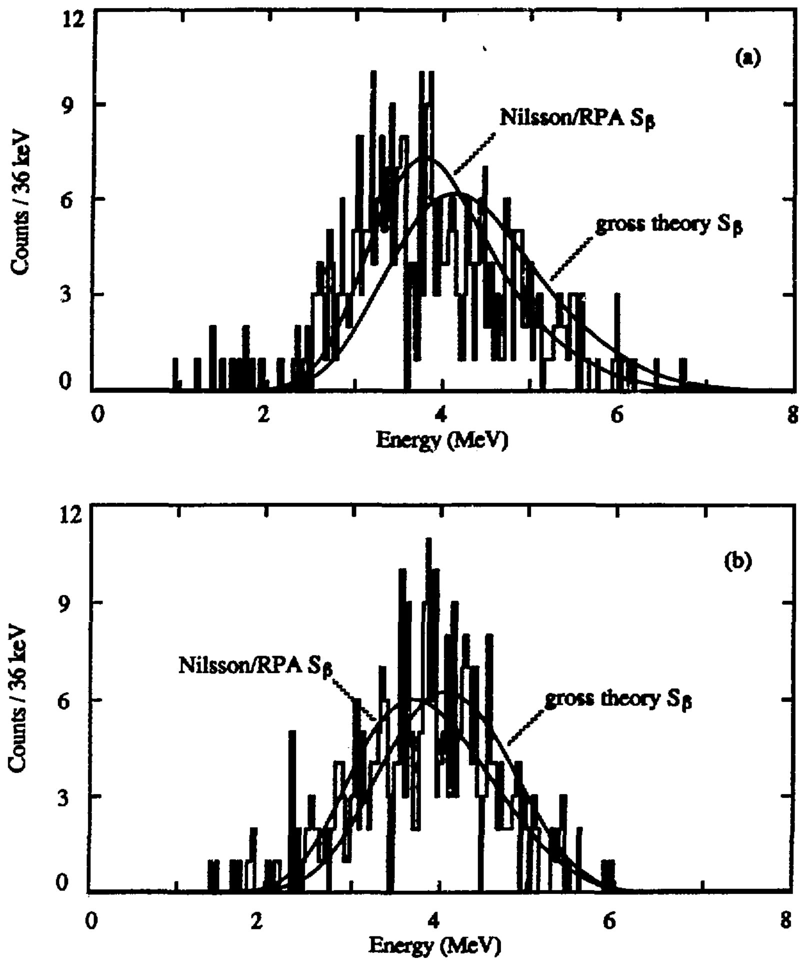

Figure 5.10. Delayed proton spectra of (a) ^{137}Gd, and (b) ^{139}Gd from experiments before the completion of the tape system. The smooth curves are from statistical model calculations using the indicated beta-strength functions. The data were first reported in [Nit83b].

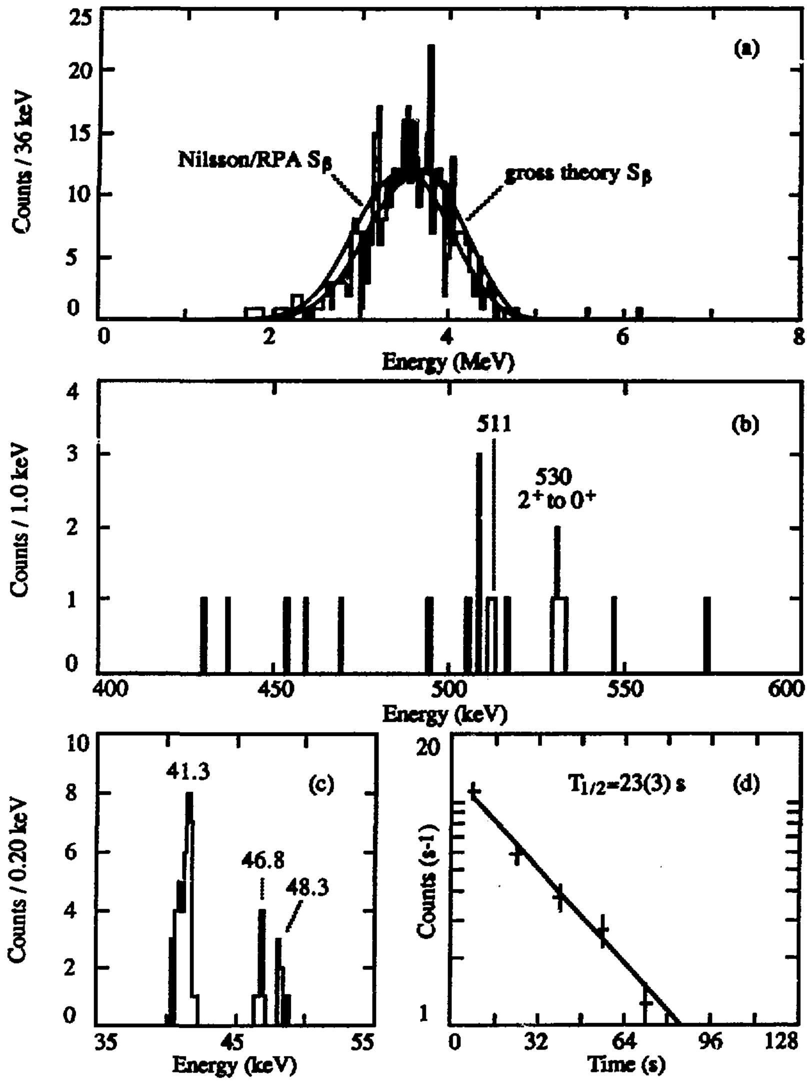

Figure 5.11. Decay of ^{141}Gd; (a) delayed proton spectrum, (b) proton coincident gamma-ray spectrum, (c) proton coincident x-ray spectrum, and (d) decay of the proton activity. The smooth curves in (a) are from statistical model calculations using the indicated beta-strength functions.

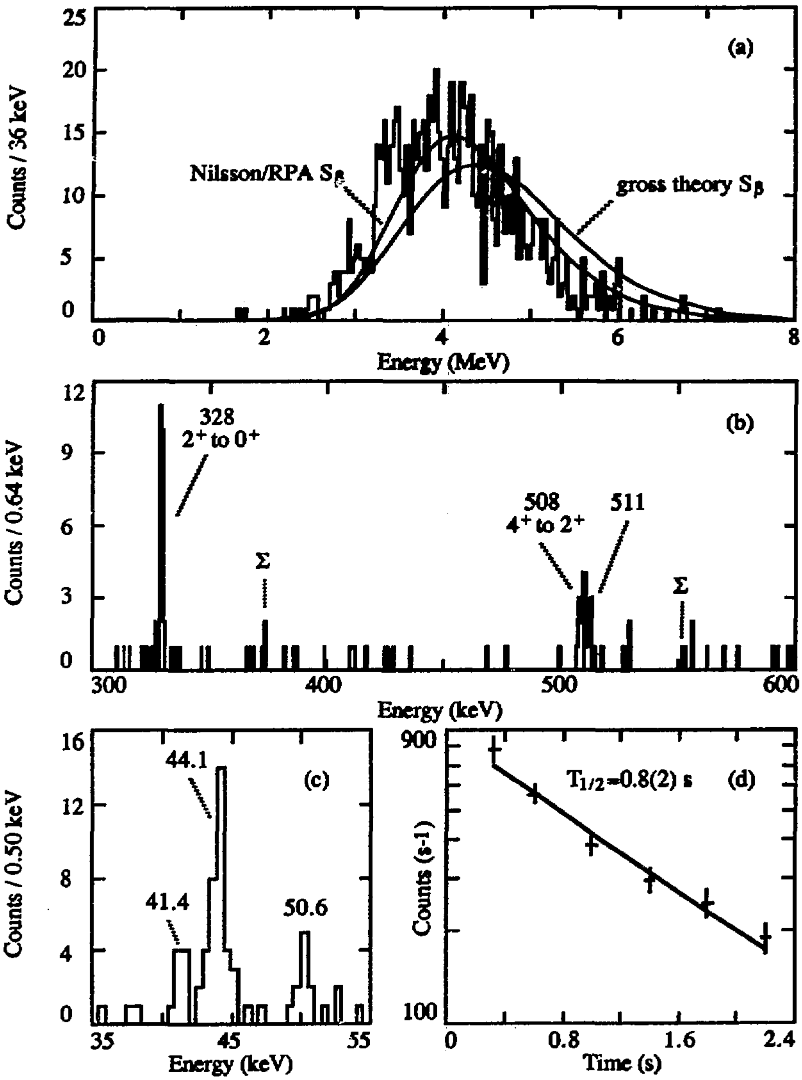

Figure 5.12. Decay of ^{141}Dy (and ^{141}Gd); (a) delayed proton spectrum, (b) proton coincident gamma-ray spectrum, (c) proton coincident x-ray spectrum, and (d) decay of the proton activity. The smooth curves in (a) are from statistical model calculations using the indicated beta-strength functions.

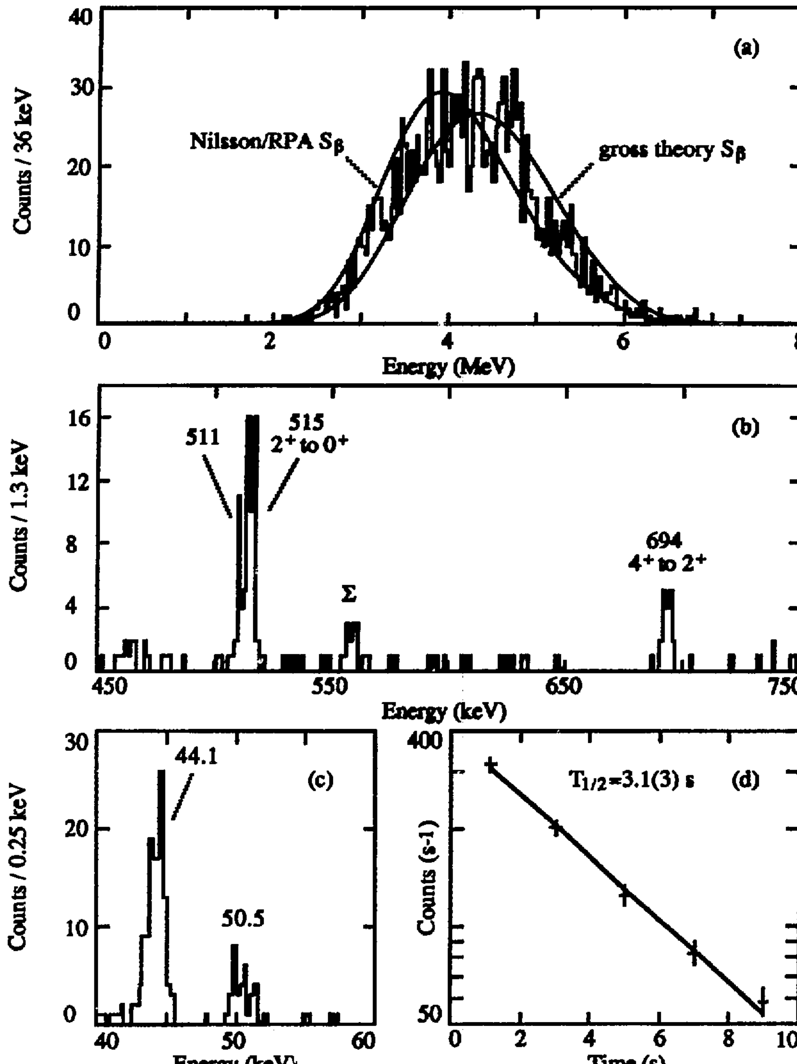

Figure 5.13. Decay of ^{143}Dy; (a) delayed proton spectrum, (b) proton coincident gamma-ray spectrum, (c) proton coincident x-ray spectrum, and (d) decay of the proton activity. The smooth curves in (a) are from statistical model calculations using the indicated beta-strength functions.

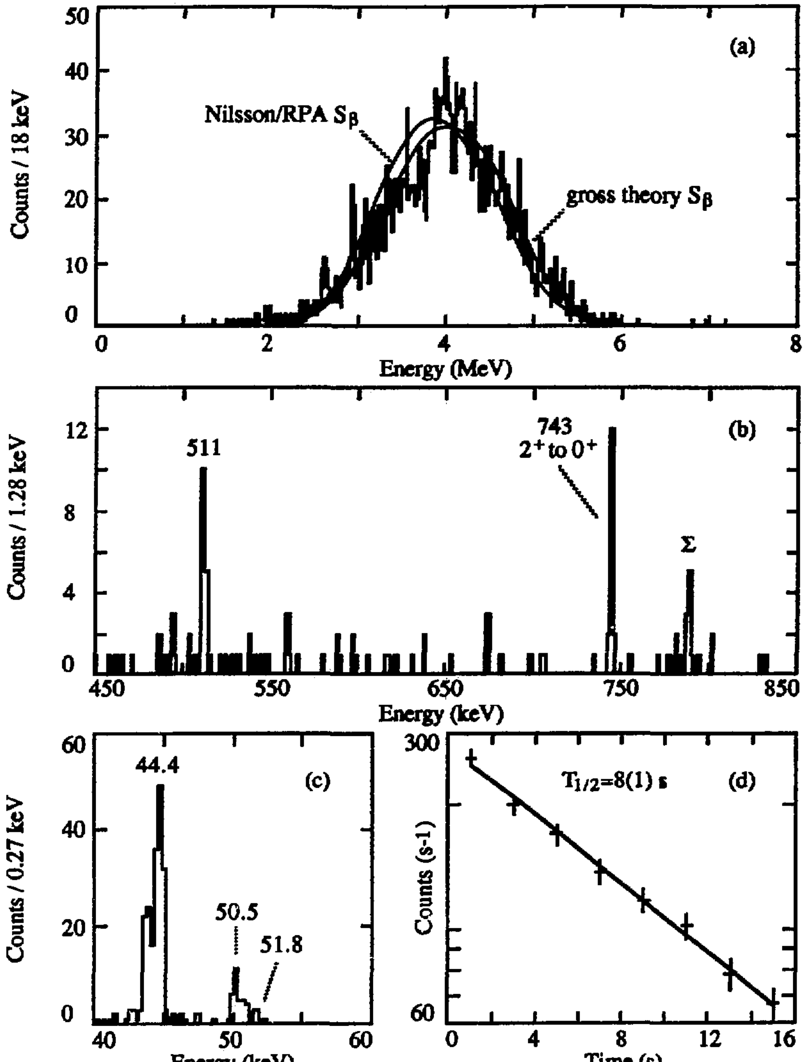

Figure 5.14. Decay of ^{145}Dy; (a) delayed proton spectrum, (b) proton coincident gamma-ray spectrum, (c) proton coincident x-ray spectrum, and (d) decay of the proton activity. The smooth curves in (a) are from statistical model calculations using the indicated beta-strength functions.

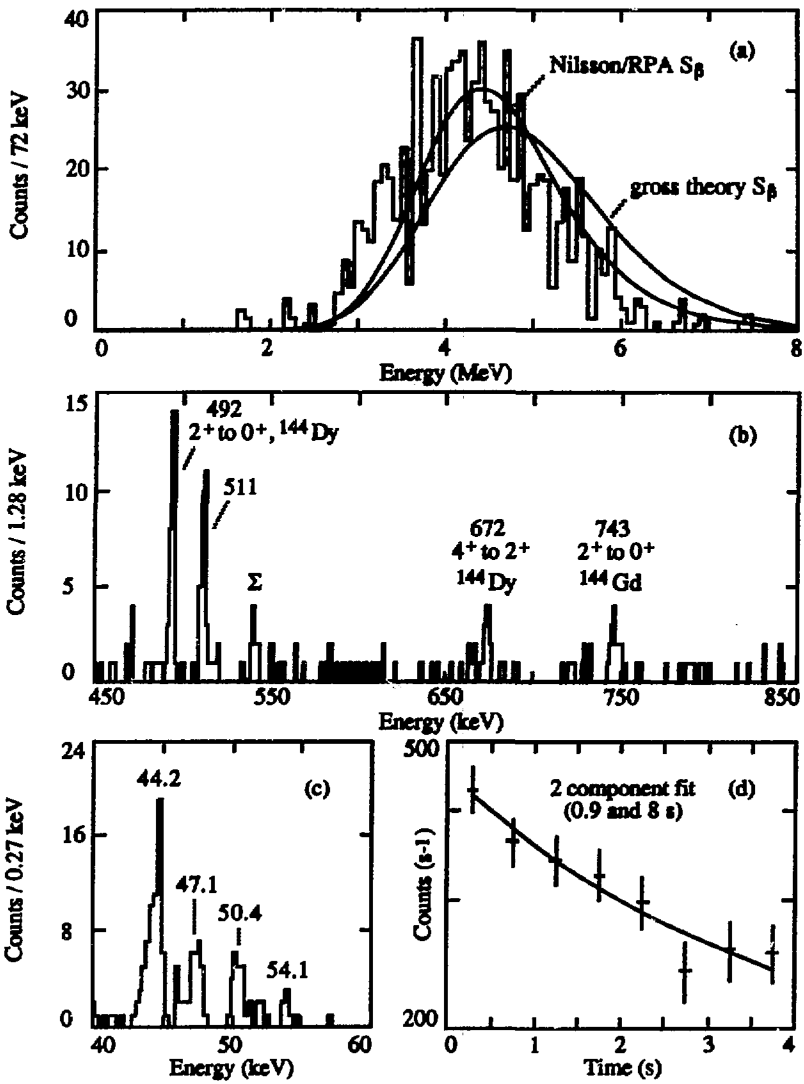

Figure 5.15. Decay of ^{145}Er (and ^{145}Dy); (a) delayed proton spectrum, (b) proton coincident gamma-ray spectrum, (c) proton coincident x-ray spectrum, and (d) decay of the proton activity. Spectrum in part (a) was obtained after subtracting the ^{145}Dy contribution. The smooth curves in (a) are from statistical model calculations using the indicated beta-strength functions.

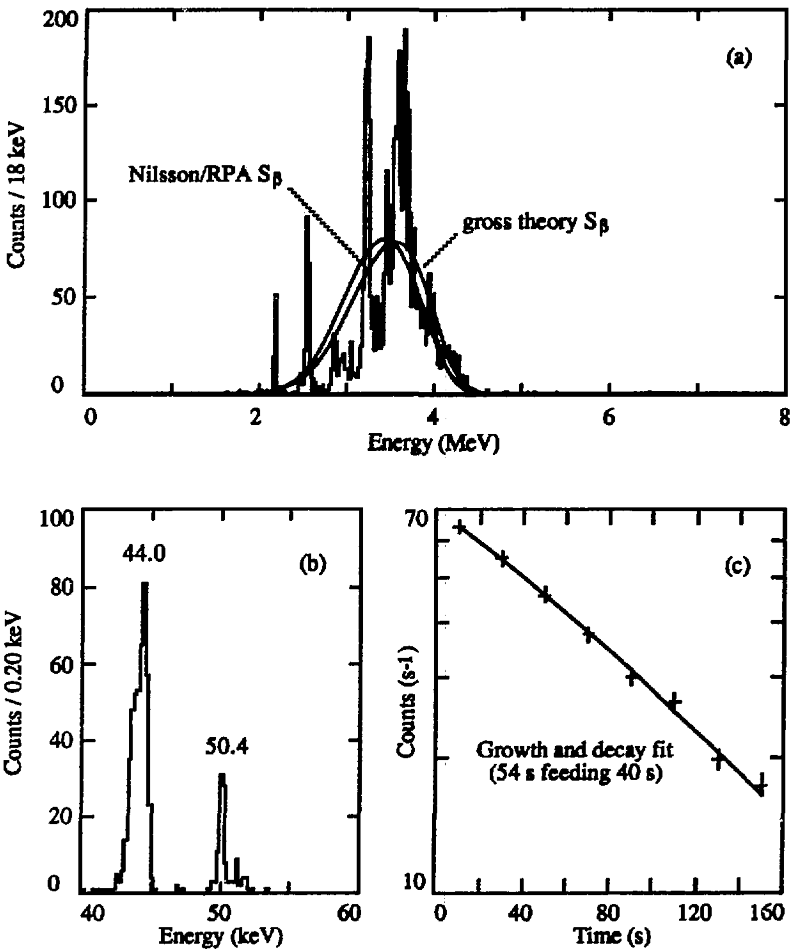

Figure 5.16. Decay of ^{147}Dy; (a) delayed proton spectrum, (b) proton coincident x-ray spectrum, and (d) decay of the proton activity. The smooth curves in (a) are from statistical model calculations using the indicated beta-strength functions. A discussion of the structured -vs- statistical nature of the proton spectrum in (a) can be found in chapter 6.

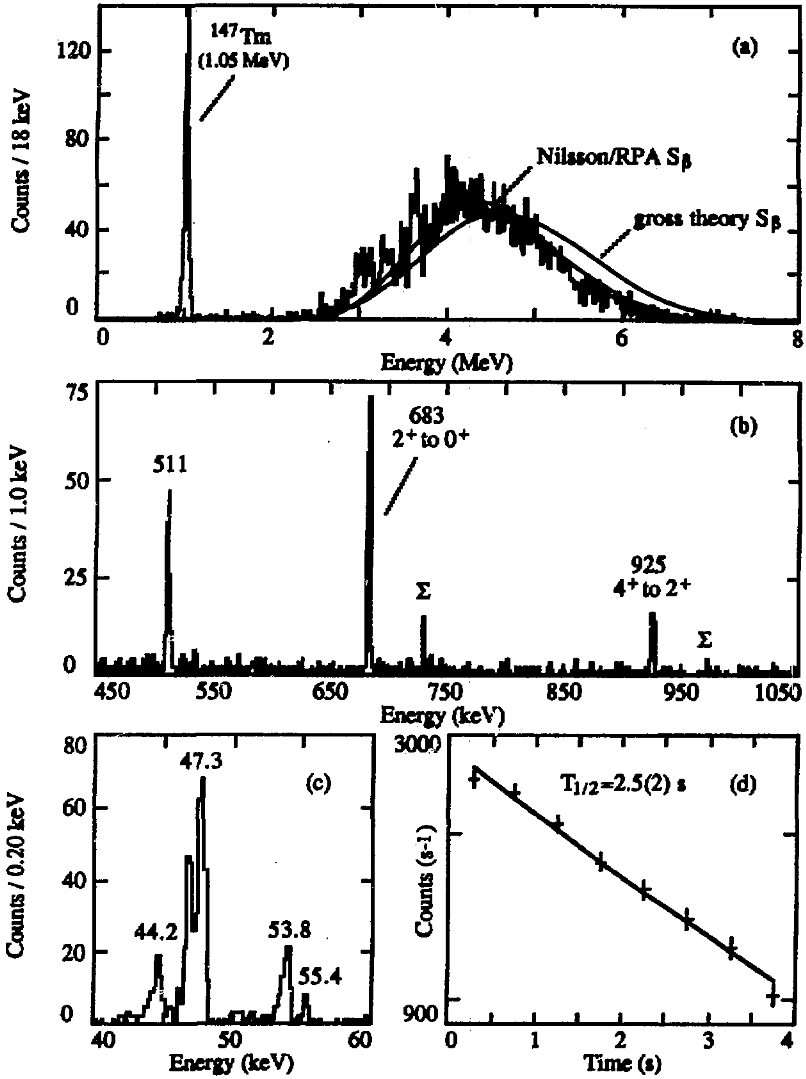

Figure 5.17. Decay of ^{147}Er (and ^{147}Dy); (a) delayed proton spectrum, (b) proton coincident gamma-ray spectrum, (c) proton coincident x-ray spectrum, and (d) decay of the proton activity. The spectrum in (a) was obtained after subtracting the ^{147}Dy contribution. Direct proton emission from ^{147}Tm (monoenergetic peak at 1.05 MeV) is also shown in (a). The smooth curves in (a) are from statistical model calculations.

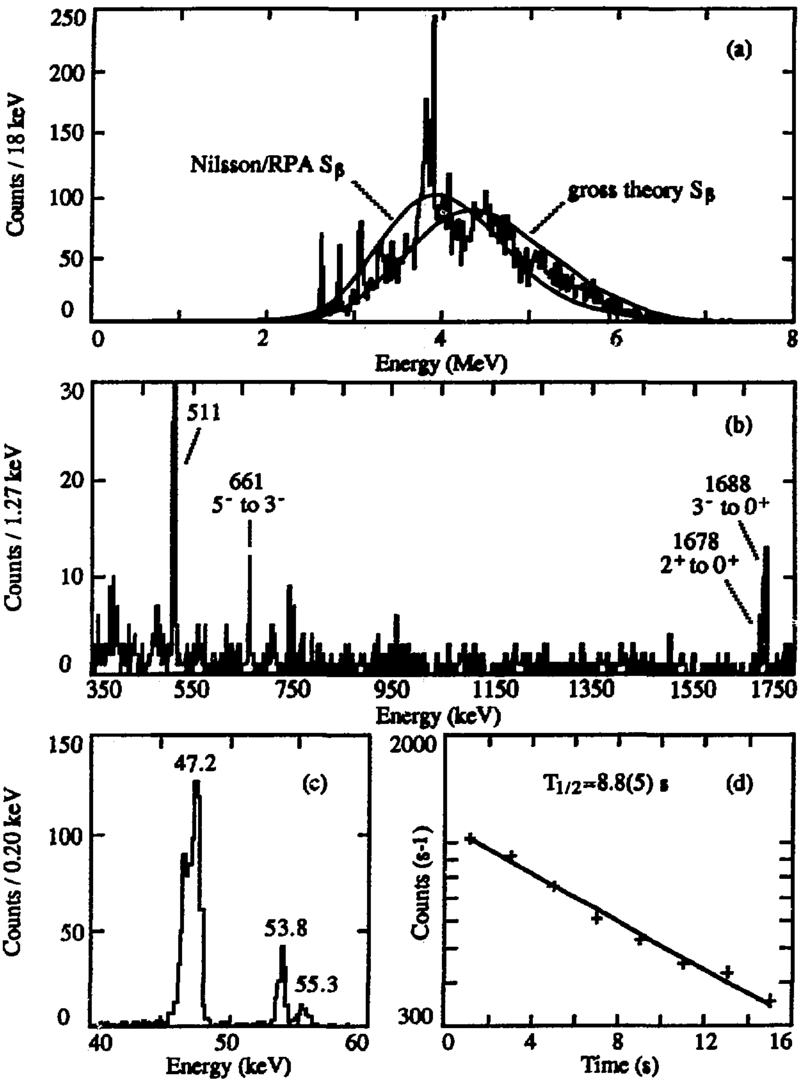

Figure 5.18. Decay of ^{149}Er; (a) delayed proton spectrum, (b) proton coincident gamma-ray spectrum, (c) proton coincident x-ray spectrum, and (d) decay of the proton activity. The smooth curves in (a) are from statistical model calculations using the indicated beta-strength functions. The structure in the proton spectrum (a) is discussed in chapter 6.

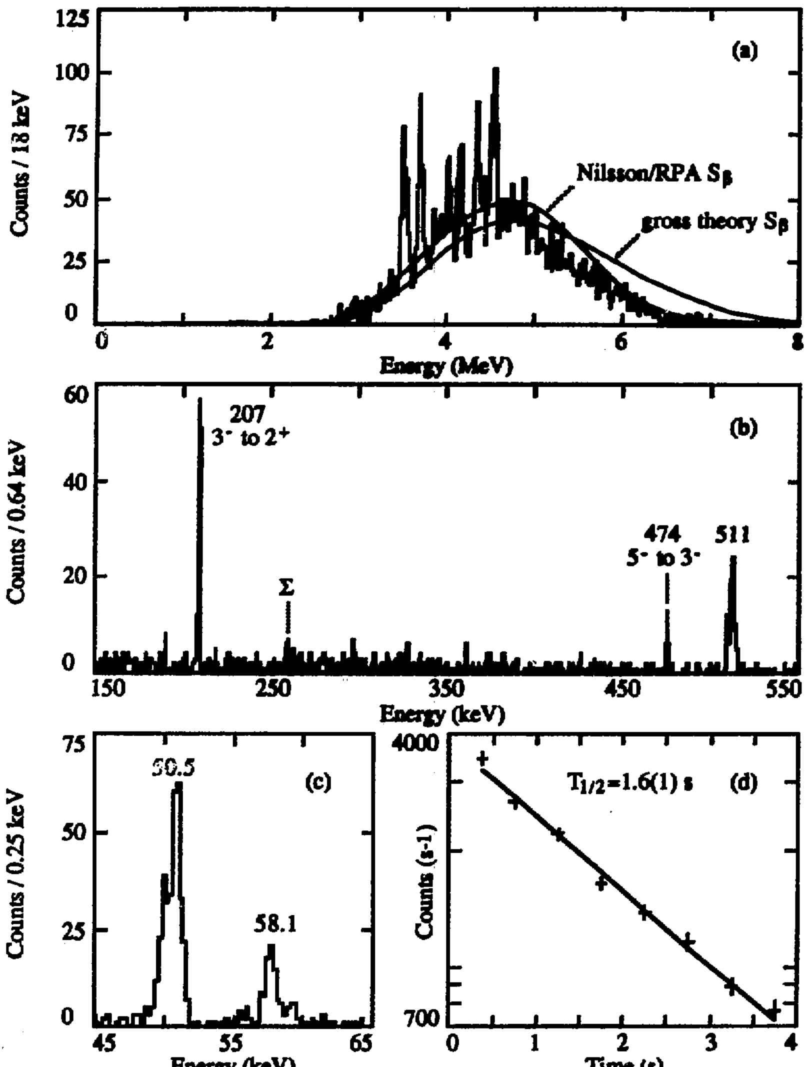

Figure 5.19. Decay of ^{151}Yb; (a) delayed proton spectrum, (b) proton coincident gamma-ray spectrum, (c) proton coincident x-ray spectrum, and (d) decay of the proton activity. The smooth curves in (a) are from statistical model calculations using the indicated beta-strength functions. The structure in the proton spectrum (a) is discussed in chapter 6.

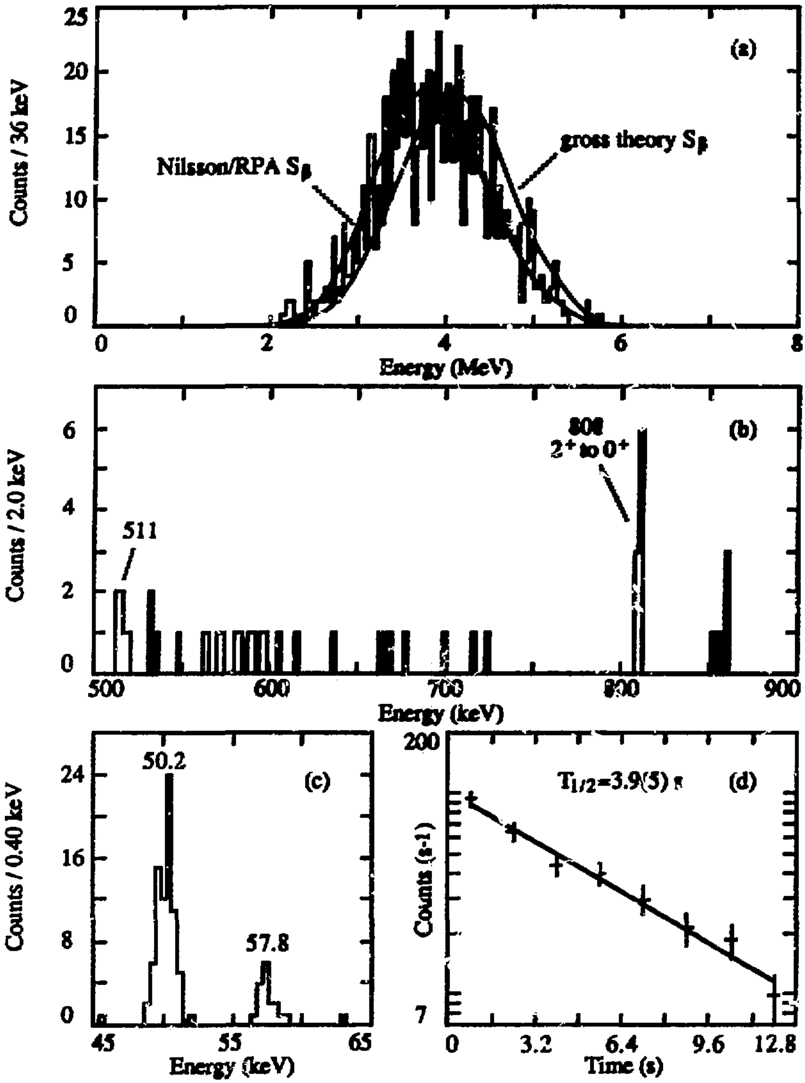

Figure 5.20. Decay of ^{153}Yb; (a) delayed proton spectrum, (b) proton coincident gamma-ray spectrum, (c) proton coincident x-ray spectrum, and (d) decay of the proton activity. The smooth curves in (a) are from statistical model calculations using the indicated beta-strength functions.

6. DISCUSSION

6.1. STRUCTURE IN N=81 EVEN-ODD PRECURSORS

Most of the delayed proton spectra (shown in the figures in chapters 4 and 5) have the typical smooth spectrum expected from heavy mass precursors due to the high level densities at excitation energies sufficiently high for proton emission. However, inspection of Figures 5.16, 5.18, and 5.19 (^{147}Dy, ^{149}Er, and ^{151}Yb, respectively) shows that the N=81 even-odd precursors exhibit pronounced structure in their delayed proton spectra. Before attempting any interpretation of the nature of this structure, isomer energies and sequences, Q values, and final state feedings have to be determined for each precursor before proton energies can be related to excitation energies in the emitter.

The even-odd N=81 isotopes ^{147}Dy, ^{149}Er, and ^{151}Yb have $11/2^-$ high-spin isomers located about 750 keV above a $1/2^+$ ground state. The proton daughter nuclei are even-even closed shell nuclei and have large energy gaps (~1.5 MeV) between the 0^+ ground state and higher-spin excited states. Due to the large angular momentum barrier for the emission of an l=5 proton from an $11/2^-$ precursor to a 0^+ daughter state, decay to higher-spin excited states is favored effectively increasing the B_p for proton emission from the $11/2^-$ isomers. This can be seen in Fig. 3.3(b) for ^{151}Yb. This shift in the effective B_p implies that proton emission of the $1/2^+$ precursor can start from states in the emitter roughly 1.5 MeV lower in excitation energy than proton emission for the $11/2^-$ isomer. Due to the different energy dependencies for positron and electron capture decay, large decay energies (feeding to low excitation energies in the emitter) occur preferentially *via* positron emission while decays to high excitation energies occur *via* electron capture. Requiring protons to be in coincidence with positrons is therefore expected to enhance the fraction of protons emitted from low excitation energies, i.e. to enhance the low-spin ($1/2^+$) precursor component. Figure 6.1(a) shows the proton singles spectrum from ^{149}Er decay and Fig. 6.1(b) shows the spectrum of protons in coincidence with positrons (recorded in the plastic scintillator). The structured component is clearly enhanced and can be associated with the $1/2^+$ precursor decaying to the 0^+ ground state in ^{148}Dy. This method was first reported in [Tot86] for ^{151}Yb and the resulting proton spectra are shown in Fig. 6.2. For this isotope, the structure is again associated with the $1/2^+$ precursor decay. In contrast, the $11/2^-$ precursor decay (protons observed in coincidence with the 3^- to 2^+ transition in ^{150}Er) was structureless [Tot86]. In the case of ^{147}Dy, the Q_{EC} is relatively low and the effective decay window for the high spin proton decay is small (~3.5 MeV) so that only 1/2$^+$ proton decay is observed. Since the peaks (or narrow resonances) in the proton spectra for all three precursors are from the 1/2$^+$ precursor ground state decaying to the 0$^+$ ground states in the proton daughter, their energies can be unambiguously related to excitation energy in the emitter, i.e. $E^* = B_p + E_p A/(A-1)$.

The spectra for ^{149}Er [Fig. 6.1(a)] and ^{151}Yb [Fig. 6.2(a)] appear to have a larger fraction of "statistical" delayed protons than the ^{147g}Dy decay [Fig 5.16(a)] which is due to the increasing fraction of delayed protons from the 11/2$^-$ isomer decays as the precursor Z increases. There were no proton coincident γ rays observed for ^{147}Dy indicating very little 11/2$^-$ precursor decay, whereas the fraction (in %) of 1/2$^+$ protons to 11/2$^-$ protons (based on predicted final state feedings in Table 5.6) were 70/30 and 50/50 for ^{149}Er and ^{151}Yb, respectively. One reason for this increase in 11/2$^-$ precursor proton intensity is that the IT branches decrease from 30% for ^{147m}Dy to 3% for ^{149m}Er to an estimated 0.3% for ^{151m}Yb. Since heavy-ion reactions predominantly produce high-spin products, the IT decay is a major source of the 1/2$^+$ precursor production so there is simply less 1/2$^+$ precursor produced for ^{149}Er and ^{151}Yb compared to ^{147}Dy. Another reason is that the energetics which are unfavorable for high-spin proton emission in ^{147m}Dy (Q_{EC}-B_p-1.5=~3.5 in MeV) are much more favorable in ^{149m}Er (Q_{EC}-B_p-1.5=~6 in MeV) and ^{151m}Yb (Q_{EC}-B_p-1.5=~9 in MeV). Given the more favorable energetics, decreasing IT branches, and the production of predominantly high spin products in heavy-ion reactions, the increase in the observed fraction of 11/2$^-$ precursor proton intensity from ^{147}Dy to ^{151}Yb can be readily explained.

Now that the structured component is seen to follow the 1/2$^+$ decay of all N=81 even-odd precursors, what gives rise to this structure? It is most likely related to the N=82 closed neutron shell in the emitters -- either the lower level densities in closed shell nuclei or some properties of the low lying levels in the emitter that are unique to N=82 nuclei. Two different experimental approaches to understand this structure were undertaken. A study of other even-odd precursors with neutron numbers near N=81, namely N=79 and N=83 precursors, was performed. In addition, a study of the odd-odd N=81 precursors, which probe higher regions of excitation energy (and higher level density) in the emitter, was also performed. The N=79 even-odd precursors have 11/2$^-$ isomers and 1/2$^+$ ground states but the 11/2$^-$ states decrease in energy rapidly with decreasing neutron number away from the closed shell. In ^{145}Dy, the 11/2$^-$ isomer is only about 117 keV above ground. There should be no appreciable IT branches in the N=79 even-odd isomers. The final state energies are also different: the first 2^+ levels are at ~700 keV with the 3^- and 4^+ levels remaining at ~1.5 MeV. The predicted feedings (see Table 5.6) for an $11/2^-$ precursor indicate considerable proton intensity to the 2^+ levels so that the separation in the excitation energies from which low- and high-spin precursor proton emission occurs is not as large as for N=81 precursors. Figure 6.3 shows the proton singles spectrum and positron coincident proton spectrum for ^{145}Dy. There may be weak structure at 2.6 and 2.9 MeV in Fig. 6.3(a) which is also present in Fig. 6.3(b) and could perhaps be associated with the $1/2^+$ decay. However, about half of the observed protons are due to the high-spin isomer which probably adds a "statistical" background to the $1/2^+$ decay and any potential structure in the proton spectrum would then be more difficult to observe. In ^{147}Er decay, Table 5.6 suggests ~85% of the protons follow the $11/2^-$ isomer β decay. In Fig. 6.4(a) there is weak, broad structure at 3.1 and 3.7 MeV in the proton singles spectra which is also enhanced in the positron coincident proton spectrum, Fig. 6.4(b). The low-spin decays in ^{145}Dy and ^{147}Er should probe similar regions of excitation energies in the emitter as the N=81 low-spin decays but the structure is much less pronounced at N=79. The only known even-odd N=83 precursor, ^{153}Yb, has no clear indication of any structure in the delayed proton spectrum [Fig. 5.20(a)]. The ground state of ^{153}Yb is expected to be $7/2^-$ and there are no known β-decaying isomers. Thus the decays of N=83 precursors are probably similar to the decay of $11/2^-$ precursors discussed above and little structure should be present.

The delayed proton decay of the three N=81 odd-odd precursors ^{148}Ho (Fig. 4.16), ^{150}Tm (Fig. 4.17), and ^{152}Lu (Fig. 4.18) is discussed in detail in [Nit88] and briefly summarized below. The decays of odd-odd precursors probe regions of higher excitation energy in the emitter due to the larger B_p values [see Fig. 3.2(d) and compare the B_p values for the N=81 odd-odd precursors (in Table 4.4) with the N=81 even-odd precursors (in Table 5.4)]. All three precursors have low- and high-spin isomers, typically 1^+, 6^- pairs, which are expected to be close to one another in energy. The proton decay daughters also have close lying low- and high-spin isomers ($1/2^+$, $11/2^-$ pairs) which create decay paths for both the low- and high-spin precursors that have very similar energetics. This can be seen in Fig. 3.3(a) for ^{150}Tm. It is very difficult to experimentally separate the low- and high-spin decays because of the similar energetics. Heavy-ion reactions are expected to strongly favor the high-spin states, and the observed final state feedings and precursor half-lives indicate that the proton decays are indeed dominated by the high-spin precursors.

The delayed proton singles spectrum from ^{150}Tm and the positron coincident proton spectrum are shown in Fig. 6.5. There is perhaps some deviation from the smooth behavior at about 3 MeV but in general the odd-odd precursors show little structure.

It was already pointed out that the structure in N=82 emitters is associated with low-spin states at relatively low excitation energies in the emitter (the decays of odd-odd precursors and 11/2- isomers, which are sensitive to higher spin levels at higher excitation energies, exhibit little structure) and is not present in emitters away from the N=82 closed shell. The decay (*via* proton and γ-ray emission) of these low-spin states in the emitter must be different than the decays of high-spin states. According to the shell model, the configurations for the 1/2+ precursor ground states are $\pi h_{11/2} \nu s_{1/2}^{-1}$ and the 11/2- isomeric precursors have configurations of $\pi h_{11/2} \nu h_{11/2}^{-1}$. The allowed Gamow-Teller β decays of both the 1/2+ and 11/2- states should be dominated by $\pi h_{11/2} \rightarrow \nu h_{9/2}$ GT transitions [Sch84a] to levels at around 4-5 MeV excitation energy in the β-decay daughters. The states following the $\pi h_{11/2} \rightarrow \nu h_{9/2}$ GT β decays of the high-spin isomers will have configurations $[(\pi h_{11/2} \nu h_{9/2})1^+ \times \nu h_{11/2}^{-1}]$ $9/2^-, 11/2^-, 13/2^-$ which can then decay by fast ~4 MeV M1 $\nu h_{9/2} \rightarrow \nu h_{11/2}^{-1}$ spin-flip transitions as shown in the top part of Fig. 6.6. The $[(\pi h_{11/2} \nu h_{9/2})1^+ \times \nu s_{1/2}^{-1}]$ $1/2^+, 3/2^+$ low spin states in the emitter following the $\pi h_{11/2} \rightarrow \nu h_{9/2}$ GT β decays of the 1/2+ precursor ground states must undergo complex rearrangements to decay to the low-lying low-spin (1/2+,3/2+, and 5/2+) single proton states (the bottom of Fig. 6.6). The γ decay of these low-spin levels is expected to be much slower than the γ decay for the high-spin states.

In [Sch84a] the β decay of ^{147}Dy was studied. The β decay of the 11/2- isomer had considerable strength to levels at ~4.7 MeV which de-excited by single high energy γ transitions to the 11/2- ground state in ^{147}Tb. In contrast, the 1/2+ β decay had considerable strength to levels at ~4 MeV which showed frequent γ branchings in their de-excitation. The low- and high-spin decays seem to be consistent with the simple shell model description presented above. Because of the slower γ decay of the low-spin levels, $\Gamma_p/(\Gamma_p+\Sigma\Gamma_\gamma)$ could be much larger than assumed in statistical model calculations and enhanced proton emission from these states would occur. A study of ^{147g}Dy [Alk86] using a total absorption spectrometer where the delayed protons and the β-strength function were independently measured indicates that the partial proton widths are about an order of magnitude larger than statistical model calculations would predict. In a detailed study of ^{149}Er β decay [Fir88], the high-spin decay showed the same pattern as in ^{147m}Dy and the partial proton widths for ^{149g}Er seemed to be about an order of magnitude larger than statistical model predictions. In both [Sch84a] and [Fir88], an attempt was made to match the proton energies to corresponding excited levels in the emitter determined from the γ-ray analysis. There is some correlation between the lowest energy proton lines and levels placed from the γ-ray data [Sch87] in ^{147g}Dy decay, but for ^{149g}Er no such correlation could be found [Fir88]. This suggests that the complex γ decay of the levels associated with the proton structure is slow enough that proton emission dominates. An interpretation of this structure in the framework of a "doorway" state model was proposed in [Nit87].

The simple shell model description above and shown in Fig. 6.6 gives a qualitative understanding of what is currently known about the structure in even-odd N=81 precursors. These low-spin states should occur at roughly the same excitation energy in the emitter and the most intense proton peaks in ^{147}Dy, ^{149}Er, and ^{151}Yb should be at essentially the same excitation in the emitter (see Fig. 6.7 where all six delayed proton spectra from N=81 precursors are shown as a function of excitation energy in the emitter) which is indeed the case. It also explains the difficulties in finding the corresponding γ decay of these levels and the large branching ratios associated with the 1/2+ decay (7% for ^{149}Er) since $\Gamma_p/(\Gamma_p+\Sigma\Gamma_\gamma)$ may be much larger than statistical model predictions. The lack of structure in the 11/2- decays and in the odd-odd precursors is due to the higher level densities at higher excitation energies and the faster γ decays of the proton-emitting states in these emitters. It should be pointed out that the proton energies associated with the 11/2- precursors in Fig. 6.7 are shown ~1.5 too low in emitter excitation energy since these protons could not be separated from those associated with the 1/2+ precursors. There may be weak structure in the N=79 1/2+ precursors, but the level densities are higher and there may be additional low-spin levels between the proton emitting region and the ground state in the emitter which could cause faster γ decays and reduce the level widths for proton emission.

6.2. Q_{EC}-B_P DETERMINATIONS

The detailed studies of the precursors near N=82 made it possible to measure the mass difference Q_{EC}-B_p by comparing the number of protons in coincidence with positrons to the total number of protons η_p. For a series of assumed Q_{EC} and B_p values, the proton energies can be related to excitation energies $E^*=B_p+E_pA/(A-1)$ which imply β-decay energies of $Q'=Q_{EC}-E^*$. The β^+ to (EC + β^+) ratios for these decay energies can be precisely calculated [Gov71] and compared to the measured values. The η_p values depend on the difference between Q_{EC} and B_p since the β^+ to $(EC + \beta^+)$ ratio is determined by the β-decay energy only. Because the experimental η_p value is usually an average over the entire proton spectrum and the final states in the proton daughter, proper averaging of the calculated ratios is required [Hor72a]. The η_p values were calculated according to following formula:

$$\eta_p = \frac{\sum_x I_p(x) \left[\sum_f W_f(E_p, E_f)\, \omega(Q') \right]}{\sum_x I_p(x)},$$

where $I_p(x)$ is the measured proton intensity as a function of proton energy (or channel number), $W_f(E_p, E_f)$ are the measured final state branches, $\omega(Q')$ is the calculated β^+ to $(EC + \beta^+)$ ratio, and $Q' = Q_{EC}-B_p-E_f-E_pA/(A-1)$. The sums over x are taken over all channels in the measured proton spectrum and the sum over f is taken over the number of observed final states. The final state branches depend on the proton energy but could not be measured due to the small number of γ rays coincident with protons. This dependence is probably strongest at the lowest and highest proton energies where the weighting by the proton spectrum is rather small. It was assumed that the final state branches were constant over the entire proton spectrum.

Using this technique, the results for ^{147}Er and ^{150}Tm are shown in Figs. 6.8(a) and 6.8(b), respectively. The statistical errors of the experimental η_p's were used to estimate the errors in $Q_{EC}-B_p$ values. Other $Q_{EC}-B_p$ values are listed in Table 6.1. The values for ^{149}Er and ^{151}Yb were determined in a slightly different way. The areas of the peaks in the proton singles and the positron coincident proton spectra were compared and the $Q_{EC}-B_p$ values inferred from the ratios [Fir88]. Since the peaks represent transitions to the 0^+ ground state in the daughter, there is no need to average over the proton spectrum. The extrapolated values from [Wap87] in Table 6.1 seem to offer better agreement with experiment than the values from [Lir76]. The B_p values quoted in [Wap87] are generally smaller than those in [Lir76] in the region near N=82 which may have a slight influence on the interpretation of the N=81 emitters discussed above. A figure similar in layout to Fig. 6.7 using the B_p values from [Wap87] instead of the values from [Lir76] can be found in [Nit87]. These figures are essentially identical; the region of excitation energy associated with the structure is still roughly the same for the three even-odd precursors and proton emission for odd-odd precursors occurs at higher excitation energies in the emitters than for the $1/2^+$ even-odd precursors.

6.3. STATISTICAL MODEL CALCULATIONS

Nuclear properties of the delayed proton emitters near N=82 are of great interest because of the structure discussed above and the close proximity to the proton drip line. However, a major focus of this work was to systematically study delayed proton emission of heavy mass precursors and to learn if the proton emission process could be adequately described within a statistical model framework. The emitters in the highly deformed region midway between the Z=50 and N=82 closed shells should satisfy the main requirement of a statistical model, namely, that the level spacing in the emitter be comparable to the level width. The low level densities near closed shells and shell model effects such as the slow γ decay of low spin states in N=82 emitters (^{147g}Dy, ^{149g}Er, and ^{151g}Yb) cannot be treated correctly in the simple statistical model presented in chapter 3.

An examination of the delayed proton spectra and the associated calculated spectra shown in the top part of the figures in chapters 4 and 5 indicates that, with the exception of the N=81 precursors, the statistical model calculations agree reasonably well with the measured spectra. In almost every case, the calculations using the Nilsson/RPA β-strength functions appear to be in much better agreement with the experiments than calculations using the gross theory β-strength functions. This is more quantitatively presented in Table 6.2, where the experimental spectra are compared with the results from three sets of calculations using three different forms of the β-strength function. The centroids from the Nilsson/RPA calculations are typically within 100 to 200 keV of the experiment while the gross theory and constant S_β calculations result in spectra that have centroids typically ~400 keV too high in energy. A chi squared X^2 evaluation was also performed to determine a "goodness of fit" parameter. A slight dependance on the number of counts prevented a comparison of the "goodness of fit" between different precursors but could still be used to judge the agreement between the experiment and the three different calculations for a given precursor. The X^2 values for each precursor were normalized to the X^2 value for the Nilsson/RPA calculation. The Nilsson/RPA results have X^2 values that are typically a factor of 2 to 3 better than the other calculations.

Other parameters in the statistical model can also influence the shape of the proton spectrum. Small changes in level densities, optical model parameters, and γ widths do not change the shape of the proton spectrum very much; however, the Q_{EC} and B_p values can have a significant effect of the spectrum shape, as shown in Fig. 4.2 for ^{122}La. The predictions of [Lir76] are generally expected to be reliable [Hau84] and data from the half-life predictions discussed below also indicate the energetics were well described in most cases. The strongest influence on the proton spectrum shape is exerted by the different β-strength functions, and the Nilsson/RPA model is clearly in better agreement with experiment in this region. However, due to the influences of the other parameters in the statistical model, direct measurements of the β-strength functions are the only method to determine if the Nilsson/RPA S_β calculations reliably reproduce the experimental S_β's. All that can be concluded from the delayed proton studies thus far is that the Nilsson/RPA S_β's in conjunction with the other statistical model parameters listed in Tables 4.4 and 5.4 result in much improved agreement with the experimental data.

The shape of the delayed proton spectrum is not the only quantity the statistical model must reproduce: the β-to-proton branching ratios and the relative branches to final states should also be correctly predicted. Very few odd-odd precursors had any γ rays in coincidence with delayed protons, so the majority of the final state feedings were obtained for even-odd precursors and are listed in Tables 5.5 and 5.6. The statistical model calculations are indeed capable of predicting the measured final state branches within the experimental uncertainty and could even be used in the region above Z=64 to determine the fraction of low- and high-spin precursors contributing to the delayed proton decay. The calculations of the final state feedings are, as expected, most sensitive to the optical model parameters and the choice of the precursor spin (see Table 5.5). The effect of the different β-strength functions on the final state feeding is shown in Table 5.7 for the example of ^{153}Yb, and in general there are only small differences in the values from the three calculations. Another indication that the optical model parameters used in the calculations (and to a lesser extent the γ widths) are reasonable is that the onset of proton emission is very well predicted by the statistical model calculations which can be seen in the figures in chapters 4 and 5. Even in cases where the calculation did not match the centroid or the upper part of the measured proton spectrum, the onset of emission was reliably predicted.

The final state feedings observed in delayed proton studies are a very sensitive method to identify the low-lying rotational transitions in even-even nuclei very far from stability. In all even-odd precursor decays, at least the first 2^+ to 0^+ transition in the proton daughter was observed. The x-rays, in coincidence with the delayed protons, and the mass separator uniquely identify the precursor and consequently, the even-even proton daughter. The x-ray sum peaks in the proton coincident γ-ray spectra provide additional identification information. In-beam γ-ray spectroscopists may have difficulty identifying band heads in nuclei far from stability due to the low cross sections and the possibility that transitions from other isotopes could obscure the transition of interest. The data from delayed proton studies may provide important complementary information on the level properties of even-even nuclei.

The other important quantity in evaluating the reliability of the statistical model calculations is the proton branching ratio. Unfortunately, proton branching ratios are difficult to determine with the present experimental setup. Essentially complete decay scheme work in nuclei with very complicated β decays due to the large Q_{EC} values and high level densities is required. This process is extremely time consuming and there is the potential for large errors in the total β intensity (and thus P_p) if there are incorrect assumptions about the decay scheme. The measured and predicted P_p's are listed in Table 6.3. There are only four measured values in the deformed region and the statistical model calculations are in reasonable agreement with experiment. The remainder of the measured values are for nuclei near N=82. The value for ^{153}Yb is in good agreement with the calculations but the N=81 precursors have branches that are about a factor of 10 larger than predicted. In the case of ^{149g}Er, the shell model interpretation discussed above would suggest a branch much larger than predicted. A possible explanation for the other precursors is a lower level density in N=82 nuclei than predicted, since the level density has a strong influence on the branching ratio. In [Nit88] the branching ratios for the three odd-odd precursors could be reproduced by decreasing the a parameter in the level density formula to 70% of the predicted value. Decreasing the γ widths will also result in larger branching ratios and may be justified for the odd-odd precursors. The precursor is expected to have a spin ~6^- in all three cases and is assumed to β decay by allowed GT transitions to 5^-, 6^-, or 7^- states in the even-even emitter. The even-even N=82 nuclei have a 0^+ ground state and higher spin states about 1.5 MeV above ground. In the statistical model, the γ width is given by equation 3.6 where the γ-strength function is integrated from 0 to the maximum available γ-decay energy. Since there is no γ decay from high spin levels to the 0^+ level, the maximum γ-decay energy should be E*-1.5 MeV rather than E*. The calculations presently do not take into consideration the low-lying level structure in the emitter and the γ strength is probably too large, resulting in low branching ratios.

6.4. PRECURSOR HALF-LIVES

While comparing β-strength functions and their effects on the statistical model calculations, the question of predicting precursor half-lives with the different β-strength functions arises. Half-life predictions in nuclei far from stability are of importance in s- and r-process calculations. In Tables 4.2 and 5.2 predictions from both the gross theory and Nilsson/RPA calculations are listed along with the measured values. Both models show surprisingly good agreement with the experimental values and, even more surprisingly, the two models usually predict similar values. The Q_{EC} values [Lir76] were the same in both calculations and, since two very different models show similar deviations from the measured values, it was suspected that errors in the Q-value predictions are the source of these deviations. For the gross theory calculations, changing the Q_{EC}'s by $\pm 5\%$ resulted in half-lives that were ~1.5 times longer with the lower Q_{EC}'s and ~0.7 times shorter with the larger Q_{EC}'s. The ratios of predicted half-lives to measured half-lives are plotted in Fig. 6.9. The scatter in the two sets of predictions is about the same with the gross theory values consistently a little longer than the experimental values. The Nilsson/RPA values could be improved slightly since there is some freedom in the choice of the Gamow-Teller quenching factor used in the calculations.

6.5. SUMMARY

Forty-two delayed proton precursors (25 new isotopes and 8 new branches) were produced in heavy-ion reactions and, after on-line mass separation, their radioactive decay properties were studied. The precursor Z and A were uniquely identified in all cases. Delayed proton spectra and final state branches were measured for all precursors and, in a few cases, proton branching ratios were determined. The statistical model adequately described the delayed proton emission process in heavy mass precursors with standard parameter prescriptions. Statistical model calculations using Nilsson/RPA model β-strength functions were compared to calculations using gross theory or constant β-strength functions. The Nilsson/RPA based calculations reproduced the spectral shapes and branching ratios better than calculations using the other β-strength functions. Precursor half-life predictions from the Nilsson/RPA S_β calculations were in better agreement with the measured values than the gross theory predictions. Final state feedings and the onset of proton emission were reasonably well predicted indicating the optical model adequately describes the low-energy proton barrier penetrability.

In N=81 precursors, which decay to N=82 closed shell proton emitters, the statistical model was not able to reproduce the experimental results. Pronounced structure associated with the decay of $1/2^+$ even-odd N=81 precursors could be explained by shell model configurations of the emitting states which have strongly hindered γ-decay channels resulting in enhanced proton emission from these states. The odd-odd N=81 precursors had proton branching ratios a factor of ~10 larger than predicted and the calculations could not reproduce the spectral shape. The branching ratio discrepancy can be resolved by reducing the level density in the emitter or decreasing the γ widths. Beta-strength functions from Nilsson/RPA calculations, which seemed to offer the best agreement with experiment in the majority of cases, may be inappropriate near closed shells since the assumption of the β-decay parent and daughter having the same deformation is not valid.

The statistical model has several free parameters and even with the large volume of data amassed for the precursors presented here, the determination of the best set of parameters was impossible. Additional data such as the direct measurement of β- and γ-strength functions, level widths, and level densities are required before further insight into the delayed proton emission process in heavy nuclei can be gained.

Table 6.1. Comparison between experimental and predicted Q_{EC}-B_p values; Experimental = Q_{EC}-B_p value from positron coincident to total proton intensity ratio, Liran-Zeldes = value calculated from [Lir76] mass formula, and Wapstra, *et al.* = value calculated from extrapolated mass values from the 1986-87 mass predictions [Wap87].

Precursor	Q_{EC}-B_p (MeV)		
	Experimental	Liran-Zeldes	Wapstra, *et al.*
^{145}Dy	5.8(4)	6.1	5.9(7)
^{147g}Dy	4.4(3)	4.8	4.5(1)[a]
^{148}Ho	5.7(5)	5.9	5.2(3)
^{147}Er	8.4(3)	8.6	8(1)
^{149g}Er	7.0(5)[b]	7.3	5.8(9)
^{150}Tm	7.5(3)	8.4	7.6(7)
^{151g}Yb	8.8(4)[c]	9.7	8.9(9)
^{153}Yb	5.7(4)	6.0	6.1(5)
^{152}Lu	9.6(9)	10.7	10(1)

[a] Mass values for precursor, emitter and proton daughter are known from other work.

[b] Reference [Fir88].

[c] R.B. Firestone, private communication.

Table 6.2. Comparison between calculated and experimental delayed proton spectra; Experiment = measured proton spectrum, Nilsson/RPA = results from statistical model calculation using a Nilsson/RPA β-strength function, Gross Theory = statistical model calculation using a gross theory β-strength function, Constant = statistical model calculation using a constant β-strength function, $\bar{E}$ = centroid of distribution in MeV, Δ = difference between measured and calculated centroids in MeV, and X^2 = a chi squared measure of the agreement between the calculated and measured spectra (see text for details). The X^2 values have been normalized to 1.0 for the Nilsson/RPA calculation. The other parameters of the statistical model were the same as those listed in Tables 4.4 and 5.4.

Precursor	Experiment	Nilsson/RPA			Gross Theory			Constant		
	$\bar{E}$	$\bar{E}$	Δ	X^2	$\bar{E}$	Δ	X^2	$\bar{E}$	Δ	X^2
^{119}Ba	3.43(1)	3.50	+0.07	1.0	3.67	+0.24	9.3	3.58	+0.15	4.1
^{120}La	3.71(3)	3.88	+0.17	1.0	4.20	+0.49	4.2	4.06	+0.35	2.2
^{122}La	3.42(2)	3.64	+0.22	1.0[a]	3.82	+0.40	2.7	3.79	+0.37	2.6
^{123}Ce	3.61(1)	3.75	+0.14	1.0	4.02	+0.41	6.8	3.91	+0.30	4.3
^{124}Pr	3.73(3)	4.05	+0.32	1.0	4.45	+0.72	5.6	4.30	+0.57	3.4
^{125}Ce	3.33(1)	3.39	+0.06	1.0	3.50	+0.17	5.9	3.50	+0.17	6.5
^{126}Pr	3.67(5)	3.80	+0.13	1.0	4.15	+0.48	4.3	4.12	+0.45	3.8
^{127}Nd	3.66(4)	3.91	+0.25	1.0	4.17	+0.51	2.7	4.03	+0.37	1.5
^{128}Pr	3.24(4)	3.27	+0.03	1.0	3.34	+0.10	1.4	3.36	+0.12	1.8
^{129}Nd	3.66(4)	3.75	+0.09	1.0	3.89	+0.23	5.5	3.90	+0.24	6.6
^{131}Nd	3.12(1)	3.06	−0.06	1.0	3.10	−0.02	0.8	3.13	+0.01	1.0
^{131}Sm	3.85(3)	4.17	+0.32	1.0	4.35	+0.50	2.2	4.19	+0.34	1.0
^{132}Pm	3.60(3)	3.77	+0.17	1.0	3.88	+0.28	1.7	3.92	+0.32	2.3
^{133}Sm	3.77(3)	3.93	+0.16	1.0	4.18	+0.41	5.5	4.16	+0.39	5.6
^{134}Eu	3.72(15)	4.24	+0.52	1.0	4.61	+0.89	1.3	4.51	+0.79	1.0
^{135}Sm	3.54(2)	3.56	+0.02	1.0	3.65	+0.11	2.3	3.69	+0.15	3.6
^{136}Eu	3.90(5)	4.12	+0.22	1.0	4.28	+0.38	1.8	4.23	+0.33	1.5
^{137}Gd	3.83(5)	4.02	+0.19	1.0	4.36	+0.53	2.6	4.33	+0.50	2.4
^{139}Gd	3.80(5)	3.85	+0.05	1.0	4.09	+0.29	2.7	4.15	+0.35	3.7
^{140}Tb	4.18(4)	4.16	−0.02	1.0	4.55	+0.37	3.2	4.59	+0.41	4.6
^{141}Gd	3.52(3)	3.47	−0.05	1.0	3.61	+0.09	1.0	3.65	+0.13	1.3
^{141}Dy	4.14(3)	4.38	+0.24	1.0	4.62	+0.48	3.8	4.57	+0.43	3.3
^{142}Dy	3.88(6)	3.86	−0.02	1.0	4.14	+0.26	3.8	4.22	+0.34	5.6
^{143}Dy	4.17(2)	4.09	−0.08	1.0	4.41	+0.24	3.5	4.49	+0.32	5.6
^{144}Dy	3.25(5)	3.43	+0.18	1.0	3.54	+0.29	2.2	3.57	+0.32	2.7
^{144}Ho	4.15(5)	4.84	+0.69	1.0	4.61	+0.46	0.4	4.63	+0.48	0.4

Table 6.2. *(continued).*

Precursor	Experiment	Nilsson/RPA			Gross Theory			Constant		
	$\bar{E}$	$\bar{E}$	Δ	X^2	$\bar{E}$	Δ	X^2	$\bar{E}$	Δ	X^2
^{145}Dy	3.99(1)	3.91	−0.08	1.0	4.03	+0.04	0.6	4.08	+0.09	0.7
^{145}Er	4.34(3)	4.64	+0.30	1.0	4.92	+0.58	3.3	4.90	+0.56	3.0
^{146}Ho	4.13(4)	4.28	+0.15	1.0	4.58	+0.45	5.5	4.68	+0.55	8.4
^{147g}Dy	3.50(1)	3.37	−0.13	1.0	3.46	−0.04	0.5	3.48	−0.02	0.4
^{147}Er	4.32(1)	4.52	+0.20	1.0	4.76	+0.44	2.8	4.85	+0.53	4.0
^{148}Ho	4.07(2)	3.94	−0.13	1.0	4.24	+0.17	2.2	4.30	+0.23	3.1
$^{149m+g}$Er	4.28(1)	4.10	−0.18	1.0	4.49	+0.21	0.9	4.60	+0.32	1.7
^{150}Tm	4.71(1)	4.49	−0.22	1.0	5.02	+0.31	1.4	5.15	+0.44	2.9
$^{151m+g}$Yb	4.52(1)	4.73	+0.21	1.0	5.05	+0.53	8.1	5.12	+0.60	12.5
^{152}Lu	4.56(5)	5.16	+0.60	1.0	5.43	+0.87	0.8	5.39	+0.83	0.6
^{153}Yb	3.88(2)	3.85	−0.03	1.0	4.10	+0.22	4.3	4.12	+0.24	5.2

[a] Using a Q_{EC} of 9.[illegible] MeV, $\bar{E}$ is 3.47 MeV and the "goodness of fit" is about a factor of [illegible]0 better.

Table 6.3. Comparison between measured and calculated proton branching ratios P_p; J^π = precursor spin and parity used in calculation, Experiment = measured P_p, Nilsson/RPA = P_p from statistical model calculation using a Nilsson/RPA β-strength function, Gross Theory = calculated P_p using a gross theory β-strength function, and Constant = calculated P_p using a constant β-strength function. The other parameters of the statistical model were the same as those listed in Tables 4.4 and 5.4.

Precursor	J^π	P_p			
		Experiment	Nilsson/RPA	Gross Theory	Constant
^{119}Ba	1/2+	–	4×10^{-2}	8×10^{-3}	8×10^{-3}
^{120}La	5-	–	2×10^{-2}	5×10^{-3}	4×10^{-3}
^{122}La	5-	–	6×10^{-4}	2×10^{-4}	1×10^{-4}
^{123}Ce	5/2+	–	8×10^{-3}	6×10^{-3}	5×10^{-3}
^{124}Pr	5-	–	6×10^{-3}	3×10^{-3}	2×10^{-3}
^{125}Ce	5/2+	–	4×10^{-4}	2×10^{-4}	2×10^{-4}
^{126}Pr	5-	–	3×10^{-4}	2×10^{-4}	1×10^{-4}
^{127}Nd	1/2+	–	4×10^{-2}	2×10^{-2}	1×10^{-2}
^{128}Pr	5-	–	7×10^{-6}	6×10^{-6}	4×10^{-6}
^{129}Nd	5/2+	–	2×10^{-3}	7×10^{-4}	5×10^{-4}
^{130}Pm	5-	–	1×10^{-3}	6×10^{-4}	3×10^{-4}
^{131}Nd	5/2+	–	2×10^{-5}	1×10^{-5}	1×10^{-5}
^{131}Sm	5/2+	–	8×10^{-2}	2×10^{-2}	2×10^{-2}
^{132}Pm	5-	–	5×10^{-5}	4×10^{-5}	3×10^{-5}
^{133}Sm	3/2+	–	9×10^{-3}	4×10^{-3}	3×10^{-3}
^{134}Eu	5-	–	6×10^{-3}	2×10^{-3}	1×10^{-3}
^{135}Sm	5/2+	$2(1)\times10^{-4}$	1×10^{-4}	2×10^{-4}	1×10^{-4}
^{136}Eu	3+	$9(3)\times10^{-4}$	4×10^{-4}	4×10^{-4}	2×10^{-4}
^{137}Gd	5/2+	–	1×10^{-2}	1×10^{-2}	7×10^{-3}
^{139}Gd	5/2+	–	9×10^{-4}	1×10^{-3}	7×10^{-4}
^{140}Tb	6-	$7(3)\times10^{-3}$	3×10^{-3}	1×10^{-3}	7×10^{-4}
^{141g}Gd	1/2+	$3(1)\times10^{-4}$	4×10^{-4}	1×10^{-4}	1×10^{-4}
^{141}Dy	1/2+	–	1×10^{-1}	4×10^{-2}	3×10^{-2}
^{141}Dy	11/2-	–	1×10^{-2}	5×10^{-3}	3×10^{-3}
^{142g}Tb	1+	–	3×10^{-4}	3×10^{-4}	2×10^{-4}
^{142}Dy	0+	–	1×10^{-3}	1×10^{-3}	1×10^{-3}
^{143}Dy	1/2+	–	2×10^{-2}	8×10^{-3}	6×10^{-3}
^{143}Dy	11/2-	–	4×10^{-4}	3×10^{-4}	2×10^{-4}
^{144}Dy	0+	–	1×10^{-4}	6×10^{-5}	7×10^{-5}

Table 6.3. ***(continued).***

Precursor	J^{π}	P_p			
		Experiment	Nilsson/RPA	Gross Theory	Constant
^{144}Ho	6^-	–	9×10^{-3}	5×10^{-3}	3×10^{-3}
^{145g}Dy	$1/2^+$	–	5×10^{-3}	1×10^{-3}	1×10^{-3}
^{145m}Dy	$11/2^-$	–	2×10^{-5}	6×10^{-6}	6×10^{-6}
^{145}Er	$1/2^+$	–	2×10^{-1}	8×10^{-2}	6×10^{-2}
^{145}Er	$11/2^-$	–	2×10^{-2}	7×10^{-3}	4×10^{-3}
^{146}Ho	6^-	–	2×10^{-3}	1×10^{-3}	6×10^{-4}
^{147g}Dy	$1/2^+$	$2(1)\times10^{-3}$	5×10^{-4}	9×10^{-5}	9×10^{-5}
^{147}Er	$1/2^+$	–	9×10^{-2}	3×10^{-2}	2×10^{-2}
^{147}Er	$11/2^-$	–	2×10^{-3}	7×10^{-4}	5×10^{-4}
^{148}Ho	6^-	$8(2)\times10^{-4}$	3×10^{-4}	8×10^{-5}	6×10^{-5}
^{149g}Er	$1/2^+$	$7(2)\times10^{-2}$	6×10^{-3}	4×10^{-3}	3×10^{-3}
^{149m}Er	$11/2^-$	$1.8(7)\times10^{-3}$	1×10^{-5}	2×10^{-5}	2×10^{-5}
^{150}Tm	6^-	$1.2(4)\times10^{-2}$	2×10^{-3}	2×10^{-3}	1×10^{-3}
^{151g}Yb	$1/2^+$	–	1×10^{-1}	5×10^{-2}	3×10^{-2}
^{151m}Yb	$11/2^-$	–	1×10^{-3}	1×10^{-3}	9×10^{-4}
^{152}Lu	6^-	$1.5(7)\times10^{-1}$	4×10^{-2}	2×10^{-2}	1×10^{-2}
^{153}Yb	$7/2^-$	$8(2)\times10^{-5}$	2×10^{-4}	1×10^{-4}	1×10^{-4}

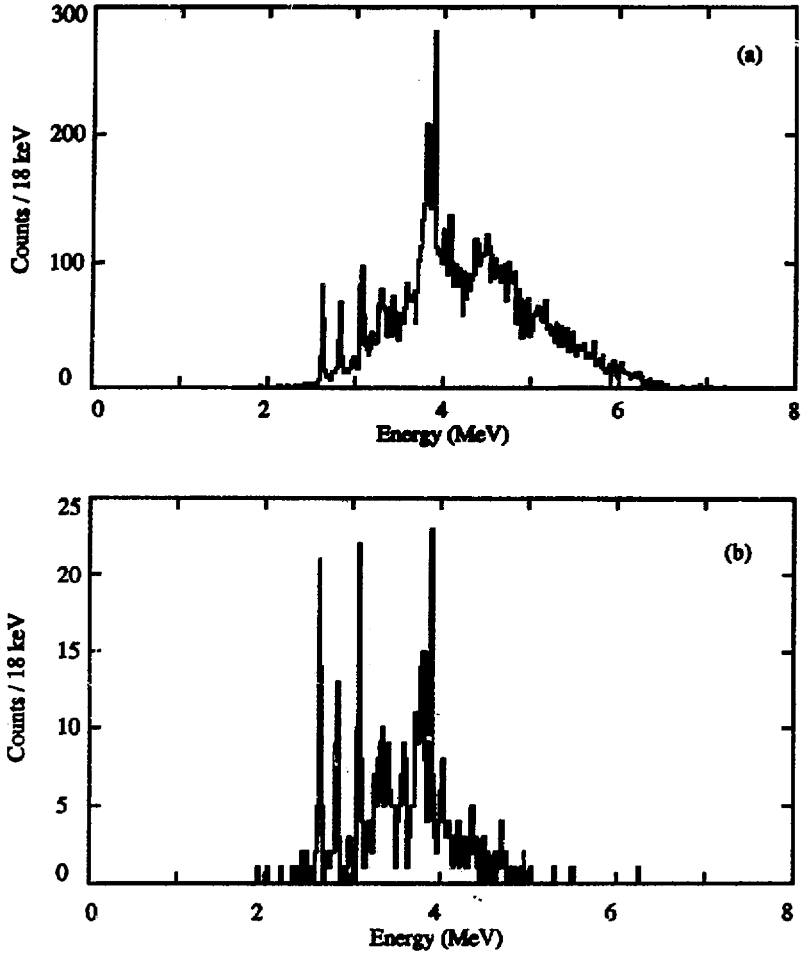

Figure 6.1. (a) Delayed proton singles spectrum and (b) positron coincident proton spectrum for ^{149}Er. From the enhancement of the structured component in spectrum (b), this structure can be assigned to the decay of the $1/2^+$ ground state in ^{149}Er to the 0^+ ground state in ^{148}Ho.

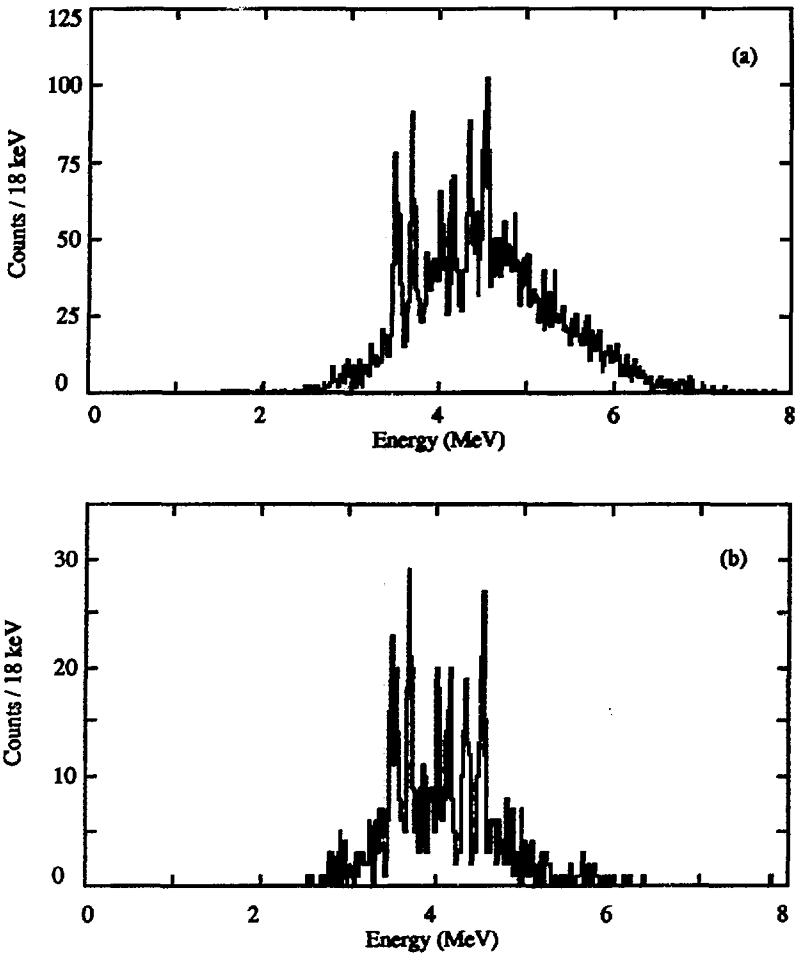

Figure 6.2. (a) Delayed proton singles spectrum and (b) positron coincident proton spectrum for ^{151}Yb. From the enhancement of the structured component in spectrum (b), this structure can be assigned to the decay of the $1/2^+$ ground state in ^{151}Yb to the 0^+ ground state in ^{150}Er.

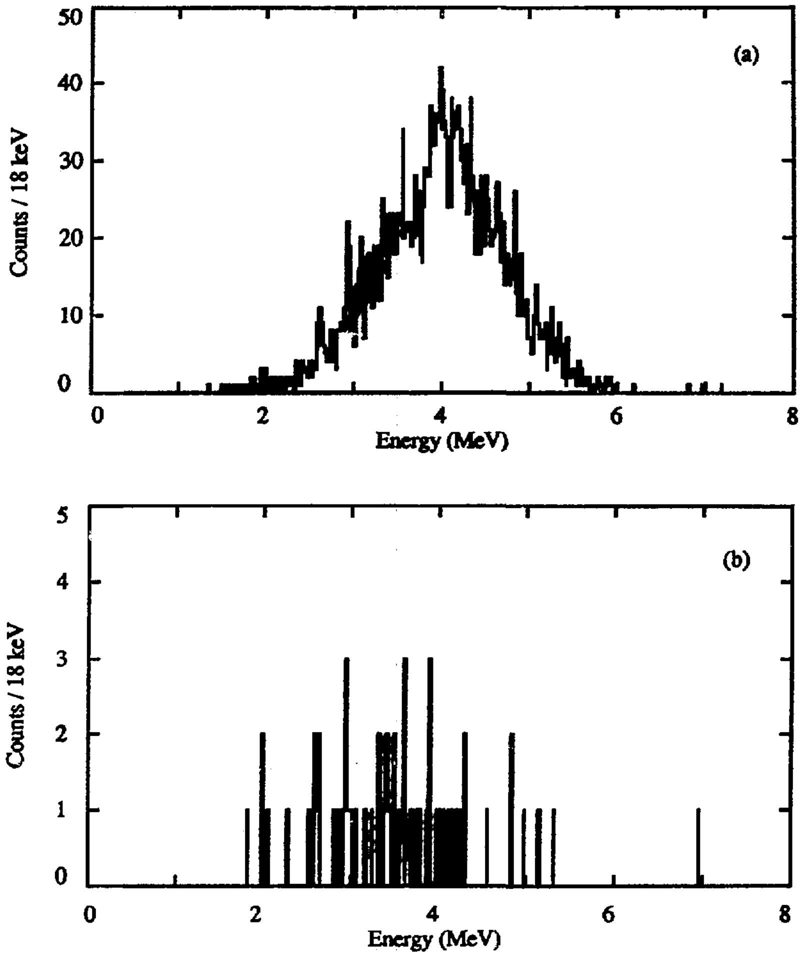

Figure 6.3. Delayed proton spectra from the combined 40 and 16 s counting cycles for ^{145}Dy; (a) proton singles spectrum and (b) positron coincident proton spectrum.

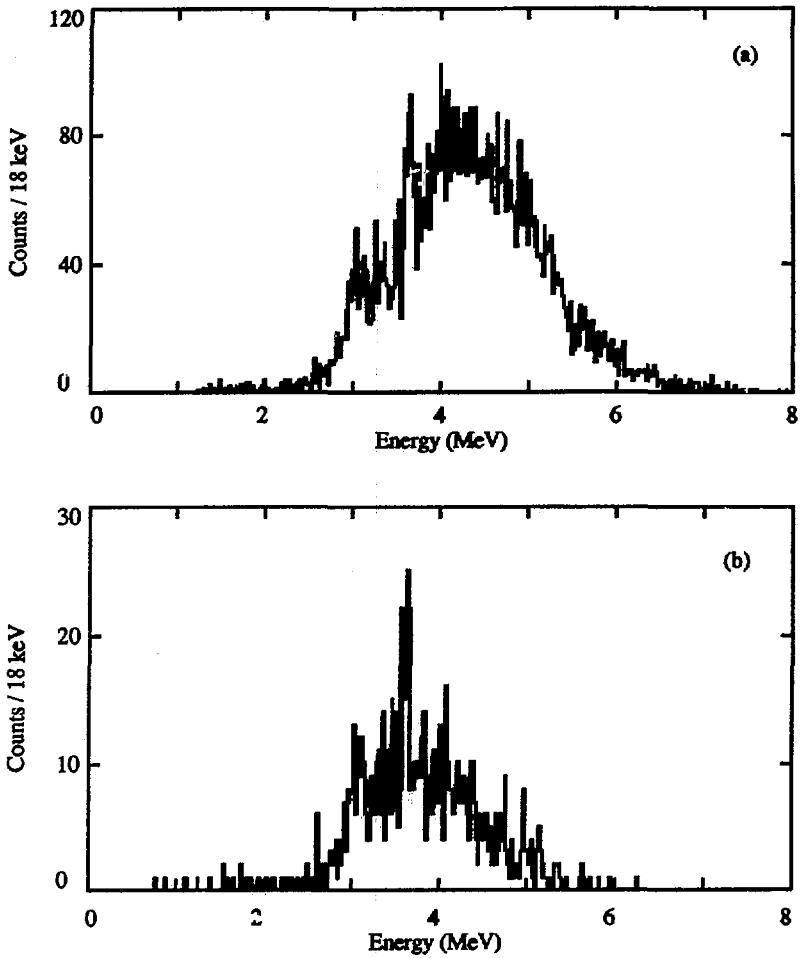

Figure 6.4. Delayed proton spectra from the combined 4 and 1.28 s counting cycles for ^{147}Er; (a) proton singles spectrum and (b) positron coincident proton spectrum. The contribution to spectrum (a) from ^{147}Dy has been subtracted.

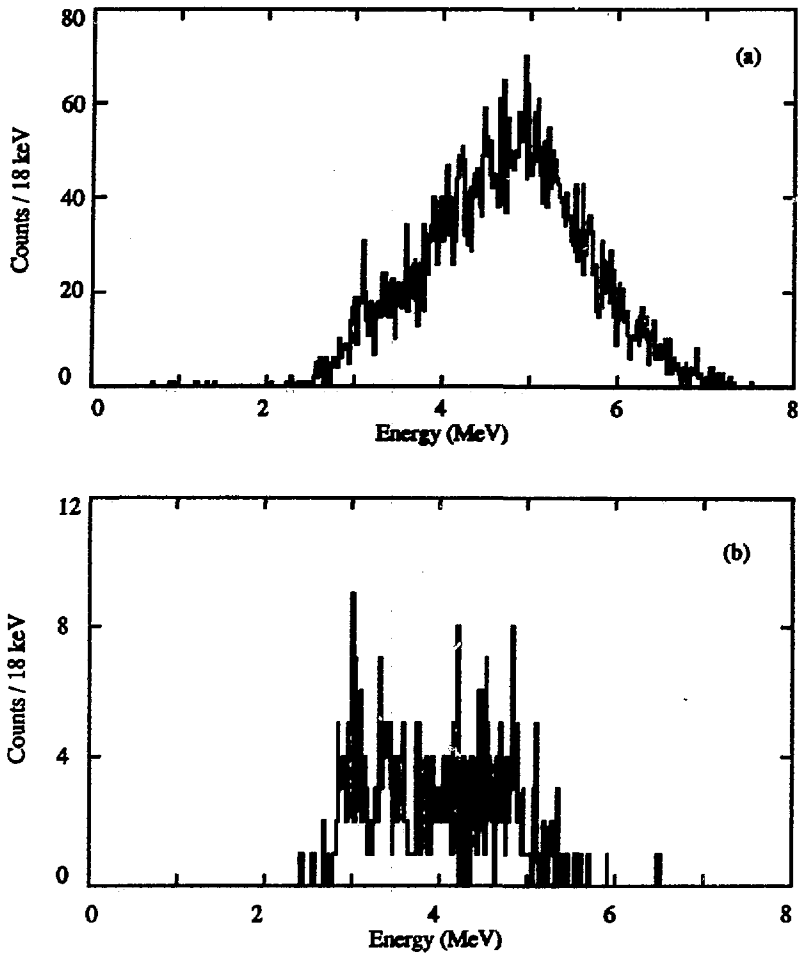

Figure 6.5. Delayed proton spectra for ^{150}Tm; (a) proton singles spectrum and (b) positron coincident proton spectrum.

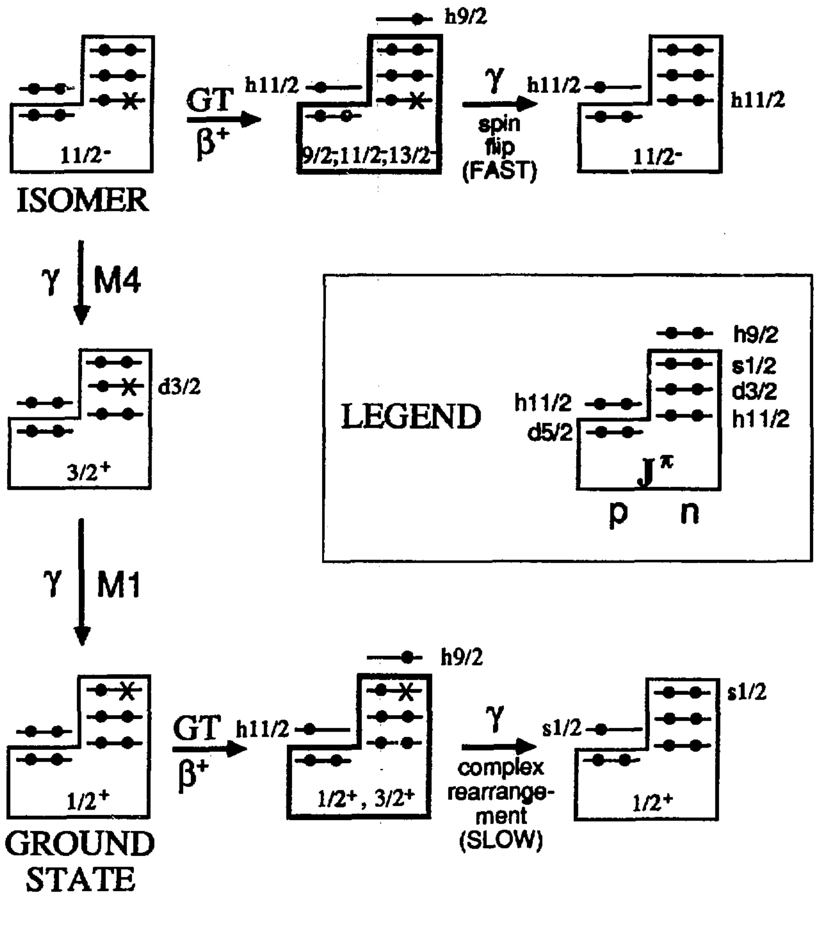

Figure 6.6. Schematic shell model representation of the decay of even Z, N=81 nuclei. The states shown in bold are at excitation energies of ~4-5 MeV in the emitter. Proton emission from the low-spin excited states dominates due to the slow gamma-decay channel associated with these states.

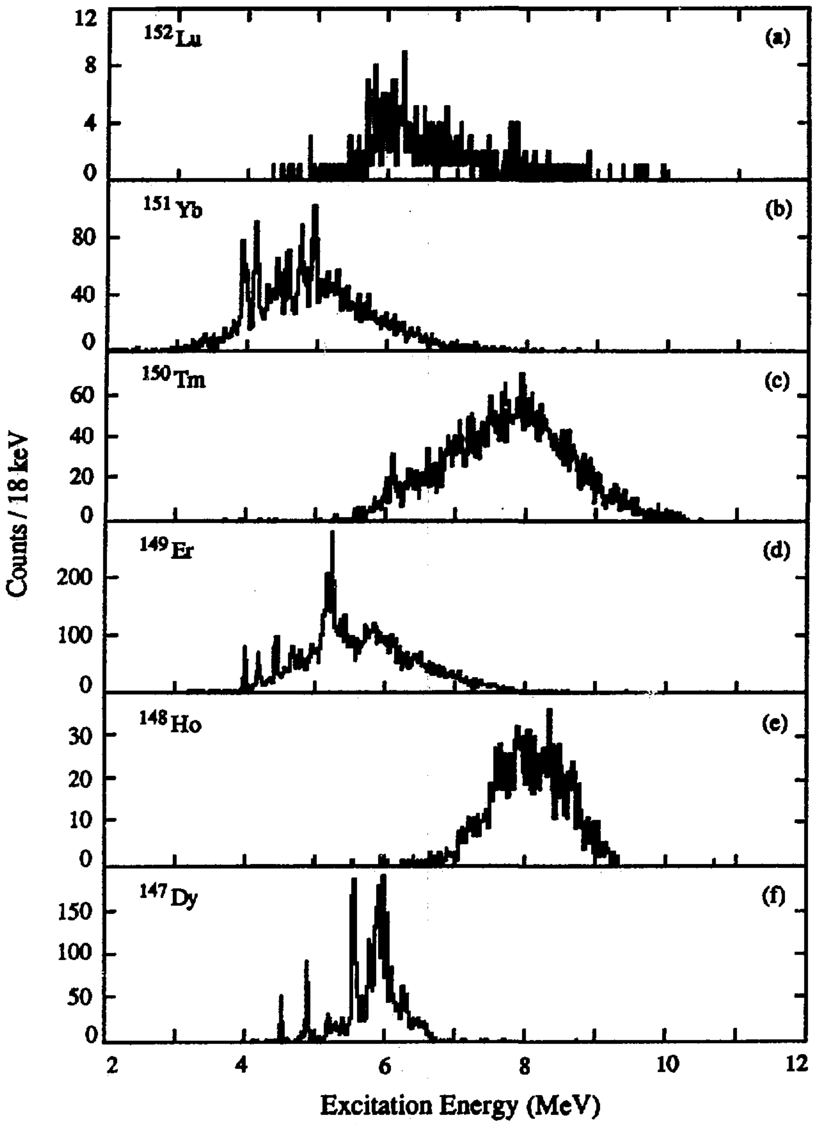

Figure 6.7. Delayed proton spectra of N=81 precursors as a function of excitation energy in the emitter. Proton separation energies were taken from [Lir76].

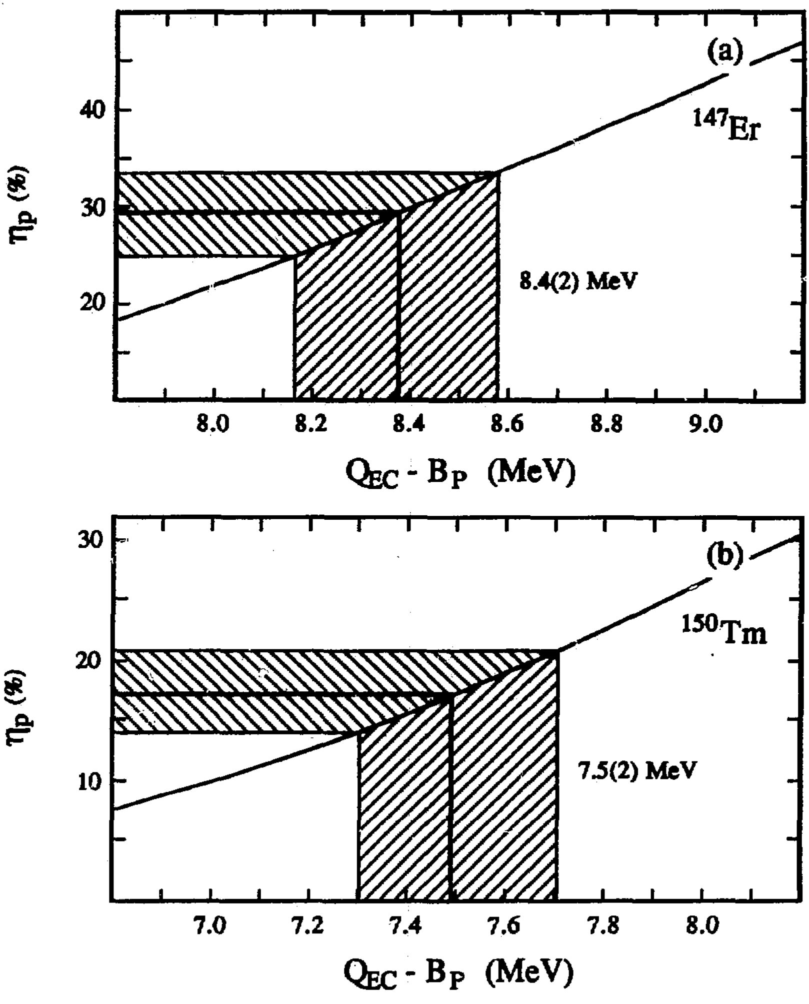

Figure 6.8. Graphs used to determine Q_{EC}-B_P from the ratio of positron coincident to total proton intensity for (a) ^{147}Er and (b) ^{150}Tm.

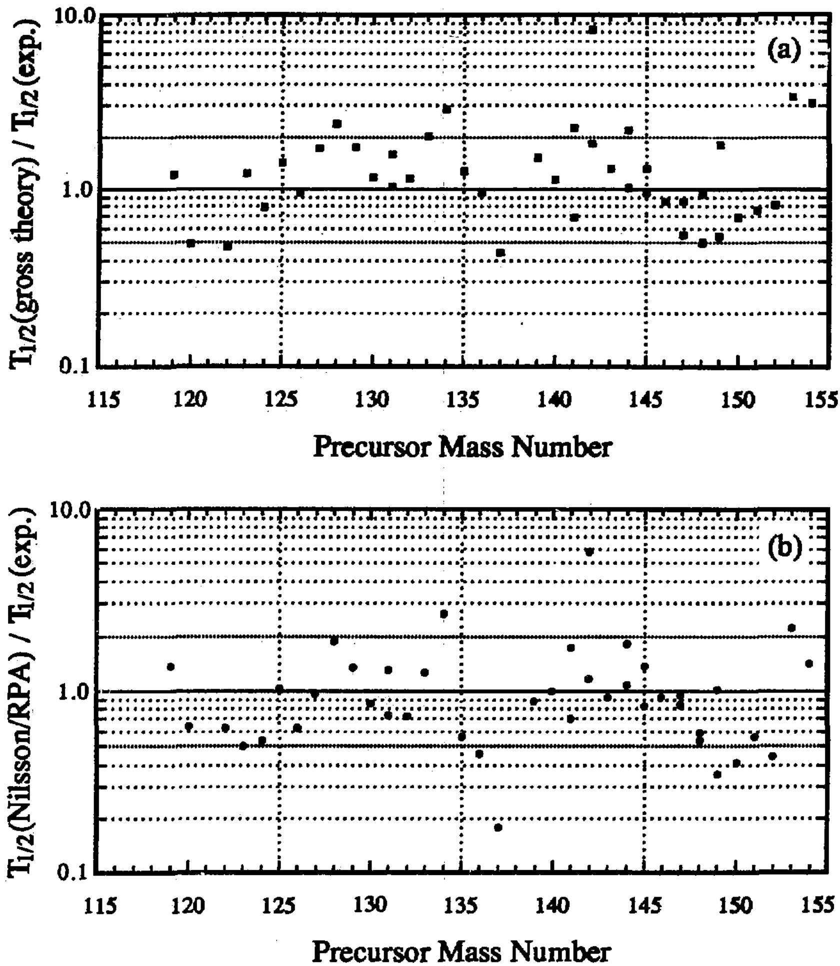

Figure 6.9. Comparison between experimental half-lives and predicted half-lives from (a) the gross theory of beta decay and (b) from Nilsson/RPA beta-strength function calculations for the delayed proton precursors listed in Tables 4.2 and 5.2.

REFERENCES

[Ako88] Y.A. Akovali, K.S. Toth, A.L. Goodman, J.M. Nitschke, P.A. Wilmarth, D.M. Moltz, M.N. Rao, and D.C. Sousa, "Single-Particle States in ^{151}Tm and ^{151}Er; Systematics of Neutron States in N=83 Nuclei", to be published.

[Alk82] G.D. Alkhazov, K.A. Mezilev, Yu.N. Novikov, V.N. Panteleyev, A.G. Polyakov, V.P. Afanasyev, N. Ganbaatar, K.Ya. Gromov, V.G. Kalinnikov, J. Kormicki, A. Latuszynski, A. Potempa, J. Sieniawski, F. Tarkanyi, and Yu.V. Yushkevich, Z. Phys. A 305, 185 (1982).

[Alk83] G.D. Alkhazov, K.A. Mezilev, Yu.N. Novikov, N. Ganbaatar, K.Ya. Gromov, V.G. Kalinnikov, A. Potempa, E. Sieniawski, and F. Tarkanyi, Z. Phys. A 310, 247 (1983).

[Alk86] G.D. Alkhazov, L.H. Batist, A.A. Bykov, V.D. Wittmann, and S.Yu. Orlov, in *Proceedings of the International Symposium on Weak and Electromagnetic Interactions in Nuclei, Heidelberg, July 1-5 1986,* edited by H. Klapdor (Springer-Verlag, Berlin and Heidelberg, 1986) p 239.

[Bar63] R. Barton, R. McPherson, R.E. Bell, W.R. Frisken, W.T. Link, and R.B. Moore, Can. J. Phys. 41, 2007 (1963).

[Bar73] G.A. Bartholomew, E.D. Earle, A.J. Ferguson, J.W. Knowles, and M.A. Lone, Adv. Nucl. Phys. 7, 229 (1973).

[Bec69] F.D. Becchetti, Jr., and G.W. Greenlees, Phys. Rev. 182, 1190 (1969).

[Bec87] E.M. Beck, F.S. Stephens, J.C. Bacelar, M.A. Deleplanque, R.M. Diamond, J.E. Draper, C. Duyar, and R.J. McDonald, Phys. Rev. Lett. 58, 2182 (1987).

[Bel86] R. A. Belshe and M. K. Lee, Nucl. Instrum. and Methods in Phys. Res. A253, 65 (1986).

[Bel87a] R. A. Belshe, EVA Reference Manual, Engineering Division Report No. 3062, Lawrence Berkeley Laboratory (1987).

[Bel87b] R. A. Belshe, SUSIE Reference Manual, Engineering Division Report No. 3061, Lawrence Berkeley Laboratory (1987).

[Bér87] R. Béraud, A. Charvet, R. Duffait, A. Emsallem, J. Genevey, A. Gizon, M. Meyer, N. Redon, and D. Rolando-Eugio, in Ref. [Tow87] p. 445.

[Bér88] R. Béraud, R. Duffait, A. Emsallem, M. Meyer, N. Redon, D. Rolando-Eugio, D. Barnéoud, J. Blachot, J. Genevey, and A. Gizon, in *Third International Conference on Nucleus Nucleus Collisions, Saint-Malo, France, June 6-11, 1988*, edited by C. Estève, C. Grégoire, D. Guerreau, and B. Tamain (Centre de Publications de l'Université de Caen, Caen Cedex, France, 1988) p. 3.

[Bil87] J. Billowes, K.P. Lieb, J.W. Noé, W.F. Piel, Jr., S.L. Rolston, G.D. Sprouse, O.C. Kistner, F. Christancho, Phys. Rev. C 36, 974 (1987).

[Bis88] P.J. Bishop, M.J. Godfrey, A.J. Kirwan, P.J. Nolan, D.J. Thornley, J.M. O'Donnell, R. Wadsworth, D.J.G. Love, and L. Goettig, J. Phys. G: Nucl. Phys. 14, 995 (1988).

[Bog75] D.D. Bogdanov, A.V. Demyanov, V.A. Karnaukhov, and L.A. Petrov, Yad. Fiz. 21, 233 (1975) [Sov. J. Nucl. Phys. 21, 123 (1975)].

[Bog77] D.D. Bogdanov, A.V. Demyanov, V.A. Karnaukhov, L.A. Petrov, A. Plohocki, V.G. Subbotin, and J.Voboril, Nucl. Phys. A275, 229 (1977).

[Bog78a] D.D. Bogdanov, A.V. Demyanov, V.A. Karnaukhov, L.A. Petrov, and J.Voboril, Nucl. Phys. A303, 145 (1978).

[Bog78b] D.D. Bogdanov, A.V. Demyanov, V.A. Karnaukhov, M. Nowicki, L.A. Petrov, J.Voboril, and A. Plochocki, Nucl. Phys. A307, 421 (1978).

[Bro84] R. Broda, Y.H. Chung, P.J. Daly, Z.W. Grabowski, J. McNeill, R.V.F. Janssens, and D.C. Radford, Z. Phys. A 316, 125 (1984).

[Cab83] M.D. Cable, J. Honkanen, R.F. Parry, S.H. Zhou, Z.Y. Zhou, and J. Cerny, Phys. Rev. Lett. 50, 404 (1983).

[Cam57] A.G.W Cameron, Can. J. Phys. 35, 666 (1957).

[Cer70] J. Cerny, J.E. Esterl, R.A. Gough, and R.G. Sextro, Phys. Lett. 33B, 284 (1970).

[Cer77] J. Cerny and J.C. Hardy, Ann. Rev. Nucl. Sci. 27, 333 (1977).

[Cha85] A. Charvet, T. Ollivier, R. Béraud, R. Duffait, A. Emsallem, N. Idrissi, J. Genevey, and A. Gizon, Z. Phys. A 321, 697 (1985).

[Con74] J. Conrad, R. Repnow, E. Grosse, H. Homeyer, E. Jaeschke, and J.P. Wurm, Nucl. Phys. A234, 157 (1974).

[CRN70] Proceedings of the International Conference on the Properties of Nuclei Far from the Region of Beta-Stability, Leysin, Switzerland, 1970, CERN Rep. 70-30 (1970).

[CRN76] Proceedings of the Third International Conference on Nuclei Far from Stability, Cargèse, Corsica, 1976, CERN Rep. 76-13 (1976).

[CRN81] Proceedings of the Fourth International Conference on Nuclei Far from Stability, Helsingør, Denmark, 1981, CERN Rep. 81-09 (1981).

[Dal78] P.J. Daly, P. Kleinheinz, R. Broda, A.M. Stefanini, S. Lunardi, H. Backe, L. Richter, R. Willwater, and F. Weik, Z. Phys. A 288, 103 (1978).

[Dil73] W. Dilg, W. Schantl, H. Vonach, and M. Uhl, Nucl. Phys. A217, 269 (1973).

[Duk70] C.L. Duke, P.G. Hansen, O.B. Nielsen, and G. Rudstam, Nucl. Phys. A151, 609 (1970).

[Eks77] C. Ekström, S. Ingelman, G. Wannberg, and M. Skarestad, Nucl. Phys. A292, 144 (1977).

[Elm78] T. Elmroth, E. Hagberg, P.G. Hansen, J.C. Hardy, B. Jonson, H.L. Ravn, and P. Tidemand-Petersson, Nucl. Phys. A304, 493 (1978).

[Fae84] T. Faestermann, A. Gillitzer, K. Hartel, P. Kienle, and E. Nolte, Phys. Lett. 137B, 23 (1984); in *Proceedings of the Seventh International Conference on Atomic Masses and Fundamental Constants, AMCO7*, edited by O. Klepper (Darmstadt, FRG, 1984) p. 177.

[Fir88] R.B. Firestone, J.M. Nitschke, P.A. Wilmarth, K. Vierinen, J. Gilat, K.S. Toth, and Y.A. Akovali, "Decay of $^{149}Er^{g+m}$ by positron and delayed proton emission, and electron capture", to be published.

[For66] *Nuclides Far Off the Stability Line, Lysekil, Sweden, 1966*, edited by W. Forsling, C.J. Herrlander, and H. Ryde (Almqvist & Wiksell, Stockholm, 1967).

[Gar78] U. Garg, T.P. Sjoreen, and D.B. Fossan, Phys. Rev. Lett. 40, 831 (1978).

[Gar79] U. Garg, T.P. Sjoreen, and D.B. Fossan, Phys. Rev. C 19, 217 (1979).

[Gen77] J. Genevey-Rivier, A. Charvet, G. Marguier, C. Richard-Serre, J. D'Auria, A. Huck, G. Klotz, A. Knipper, and G. Walter, Nucl. Phys. A283, 45 (1977).

[Gen87] J. Genevey, A. Gizon, N. Idrissi, B. Weiss, R. Béraud, A. Charvet, R. Duffait, A. Emsallem, M. Meyer, T. Ollivier, and N. Redon, in Ref [Tow87] p. 419.

[Gil65] A. Gilbert and A.G.W. Cameron, Can. J. Phys. 43, 1446 (1965).

[Gil87] J. Gilat, J.M. Nitschke, P.A. Wilmarth, K. Vierinen, and R.B. Firestone, in Ref. [Tow87] p. 463.

[God87] M.J. Godfrey, P.J. Bishop, A. Kirwan, P.J. Nolan, D.J. Thornley, D.J. Unwin, D.J.G. Love, and A.H. Nelson, J. Phys. G: Nucl. Phys. 13, 1165 (1987).

[Goe87] L. Goettig, W. Gelletly, C.J. Lister, R. Moscrop, B.J. Varley, and R. Wadsworth, Nucl. Phys. A464, 159 (1987).

[Gol66] V.I. Goldanskii, Ann. Rev. Nucl. Sci. 16, 1 (1966).

[Gov71] N.B. Gove and M.J. Martin, Nucl. Data Tables 10, 205 (1971).

[Gui82] S.Z. Gui, G. Colombo, and E. Nolte, Z. Phys. A 305, 297 (1982).

[Han73] P.G. Hansen, Adv. Nucl. Phys. 7, 159 (1973).

[Han79] P.G. Hansen, Ann. Rev. Nucl. Sci. 29, 69 (1979).

[Har72] J.C. Hardy, Nucl. Data Tables 11, 327 (1972).

[Har74] J.C. Hardy, in *Nuclear Spectroscopy and Reactions*, edited by J. Cerny (Academic, New York, 1974) Vol. C, p. 417.

[Har76] J.C. Hardy, J.A. MacDonald, H. Schmeing, H.R. Andrews, J.S. Geiger, R.L. Graham, T. Faestermann, E.T.H. Clifford, and K.P. Jackson, Phys. Rev. Lett. 37, 133 (1976).

[Har81] J.C. Hardy, in Ref. [CRN81] p. 217.

[Har82] J.C. Hardy, Phys. Lett. 109B, 242 (1982).

[Har87] J.C. Hardy and E. Hagberg, "Beta-delayed Proton and Alpha Emission", in *Particle Emission from Nuclei*, edited by M. Ivascu and D. Poenaru (CRC Press, Cleveland, to be published). Reprint courtesy of AECL, Chalk River, Ontario, Canada.

[Hau84] P.E. Haustein, in *Proceedings of the Seventh International Conference on Atomic Masses and Fundamental Constants, AMCO7*, edited by O. Klepper (Darmstadt, FRG, 1984) p. 413.

[Hof84] S. Hofmann, Y.K. Agarwal, P. Armbruster, F.P. Heßberger, P.O. Larson, G. Münzenberg, K. Poppensieker, W. Reisdorf, J.R.H. Schneider, and H.J. Schött, in *Proceedings of the Seventh International Conference on Atomic Masses and Fundamental Constants, AMCO7*, edited by O. Klepper (Darmstadt, FRG, 1984) p. 184.

[Hof87] S. Hofmann, "Proton Radioactivity", in *Particle Emission from Nuclei*, edited by M. Ivascu and D. Poenaru (CRC Press, Cleveland, to be published).

[Hor72a] P. Hornshøj, K. Wilsky, P.G. Hansen, B. Jonson, and O.B. Nielson, Nucl. Phys. A187, 599 (1972).

[Hor72b] P. Hornshøj, K. Wilsky, P.G. Hansen, B. Jonson, and O.B. Nielson, Nucl. Phys. A187, 609 (1972).

[Hor81] D. Horn, G.R. Young, C.J. Lister, and C. Baktash, Phys. Rev. C 23, 1047, (1981).

[Jac70] K.P. Jackson, C.U. Cardinal, H.C. Evans, N.A. Jelly, and J. Cerny, Phys. Lett. 33B, 281 (1970).

[Joh70] C.H. Johnson and R.L. Kernell, Phys. Rev. C 2, 639 (1970).

[Joh79] C.H. Johnson, A. Galonsky, and R.L. Kernell, Phys. Rev. C 20, 2052 (1979).

[Jon76] B. Jonson, E. Hagberg, P.G. Hansen, P. Hornshøj, and P. Tidemand-Petersson, in Ref [CRN76] p. 277.

[Jul80] R. Julin, J. Kantele, M. Luontama, A. Passoja, P. Kleinheinz, and J. Blomqvist, Phys. Lett. 94B, 123 (1980).

[Kar63] V.A. Karnaukhov, G.M. Ter-Akopian, and V.G. Subbotin, in *Proceedings of the Third Conference on Reactions between Complex Nuclei, Asilomar, 1963*, edited by A. Ghiorso, R.M. Diamond, and H.E. Conzett (University of California Press, 1963) p. 434.

[Kar67] V.A. Karnaukhov and G.M. Ter-Akopian, Ark. Fys. 36, 419 (1967).

[Kar73] V.A. Karnaukhov, D.D. Bogdanov, and L.A. Petrov, Nucl. Phys. A206, 583 (1973).

[Kar74] V.A. Karnaukhov, Fiz. El. Chast. Atom. Yad. 4, 1018 (1973) [Sov. J. Part. Nucl. 4, 416 (1974)].

[Kar75] V.A. Karnaukhov, Nukleonika 19, 425 (1975).

[Ker84] A. Kerek, T. Lönnroth, K. Honkanen, E. der Mateosian, and P. Thieberger, Z. Phys. A 317, 169 (1984).

[Ker87a] B.D. Kern, R.L. Mlekodaj, G.A. Leander, M.O. Kortelahti, E.F. Zganjar, R.A. Braga, R.W. Fink, C.P. Perez, W. Nazarewicz, and P.B. Semmes, Phys. Rev. C 36, 1514 (1987).

[Ker87b] B.D. Kern, G.A. Leander, R.L. Mlekodaj, H.K. Carter, M.O. Kortelahti, E.F. Zganjar, R.A. Braga, R.W. Fink, C.P. Perez, P.B. Semmes, and W. Nazarewicz, in Ref. [Tow87] p. 441.

[Kir77] R. Kirchner, O. Klepper, G. Nyman, W. Reisdorf, E. Roeckl, D. Schardt, N. Kaffrell, P. Peuser, and K. Schneeweiss, Phys. Lett. 70B, 150 (1977).

[Kle82] O. Klepper, Y. Batsch, S. Hofmann, R. Kirchner, W. Kurcewicz, W. Reisdorf, E. Roeckl, D. Schardt, and G. Nyman, Z. Phys. A 305, 125 (1982).

[Kle85] P. Kleinheinz, B. Rubio, M. Ogawa, M. Piiparinen, A. Plochocki, D. Schardt, R. Barden, O. Klepper, R. Kirchner, and E. Roeckl, Z. Phys. A 323, 705 (1985).

[Kor87] M. Kortelahti, E.F. Zganjar, R.L. Mlekodaj, B.D. Kern, R.A. Braga, R.W. Fink, and C.P. Perez, Z. Phys. A 327, 231 (1987).

[Kru84] J. Krumlinde and P. Möller, Nucl. Phys. A417, 419 (1984).

[Lac84] M. Lach, J. Styczen, R. Julin, M. Piiparinen, H. Beuscher, P. Kleinheinz, and J. Blomqvist, Z. Phys. A 319, 235 (1984).

[Lei73] J.R. Leigh, K. Nakai, K.H. Maier, F. Pühlhofer, F.S. Stephens, and R.M. Diamond, Nucl. Phys. A213, 1 (1973).

[Lir76] S. Liran and N. Zeldes, At. Data Nucl. Data Tables 17, 431 (1976).

[Lis85] C.J. Lister, B.J. Varley, R. Moscrop, W. Gelletly, P.J. Nolan, D.J.G. Love, P.J. Bishop, A. Kirwan, D.J. Thornley, L. Ying, R. Wadsworth, J.M. O'Donnell, H.G. Price, and A.H. Nelson, Phys. Rev. Lett. 55, 810 (1985).

[Lun86] S. Lunardi, F. Soramel, W. Starzecki, W. Meczynski, R. Julin, M. Lach, A. Ercan, and P. Kleinheinz, Z. Phys. A 324, 433 (1986).

[Mac65] R.D. Macfarlane and A. Siivola, Phys. Rev. Lett. 14, 114 (1965).

[Mak86] A. Makishima, M. Adachi, H. Taketani, and M. Ishii, Phys. Rev. C 34, 576 (1986).

[Map79] C. Maples and J. Sivak, IEEE Trans. Nucl. Sci. NS-26, 4409 (1979).

[Mar76] M.A.J. Mariscotti, H. Beuscher, W.F. Davidson, R.M. Lieder, A. Neskakis, and H.M. Jäger, Z. Phys. A 279, 169 (1976).

[Mar87] J.P. Martin, V. Barci, H. El-Samman, A. Gizon, J. Gizon, B. Nyakó, W. Klamra, F.A. Beck, T. Byrski, and J.C. Merdinger, Z. Phys. A 326, 337 (1987).

[Mat85] G.J. Mathews and R.A. Ward, Rep. Prog. Phys. 48, 1371 (1985).

[Mol81] J.D. Molitoris and J.M. Nitschke, Nucl. Instrum. and Methods 186, 659 (1981).

[Mol87] D.M. Moltz, J.E. Reiff, J.D. Robertson, T.F. Lang, and J. Cerny, in Ref [Tow87] p. 749.

[Nag81] Y. Nagai, J. Styczen, M. Piiparinen, P. Kleinheinz, D. Bazzacco, P.v. Brentano, K.O. Zell, and J. Blomqvist, Phys. Rev. Lett. 47, 1259 (1981).

[Nit76] J.M. Nitschke, Nucl. Instrum. and Methods 138, 393 (1976).

[Nit83a] J.M. Nitschke, Nucl. Instrum. and Methods 206, 341 (1983).

[Nit83b] J.M. Nitschke, M.D. Cable, and W.-D. Zeitz, Z. Phys. A 312, 265 (1983).

[Nit84] J.M. Nitschke, P.A. Wilmarth, P.K. Lemmertz, W.-D. Zeitz, and J.A. Honkanen, Z. Phys. A 316, 249 (1984).

[Nit87] J.M. Nitschke, P.A. Wilmarth, J. Gilat, P. Möller, and K.S. Toth, in Ref. [Tow87] p. 697.

[Nit88] J.M. Nitschke, P.A. Wilmarth, J. Gilat, K.S. Toth, and F.T. Avignone III, Phys. Rev. C 37, 2694 (1988).

[Nol82a] E. Nolte, G. Colombo, S.Z. Gui, G. Korschinek, W. Schollmeier, P. Kubik, S. Gustavsson, R. Geier, and H. Morinaga, Z. Phys. A 306, 211 (1982).

[Nol82b] E. Nolte, S.Z. Gui, G. Colombo, G. Korschinek, and K. Eskola, Z. Phys. A 306, 223 (1982).

[Nol82c] E. Nolte, G. Korschinek, and Ch. Setzensack, Z. Phys. A 309, 33 (1982).

[Oll85] T. Ollivier, R. Béraud, A. Charvet, R. Duffait, A. Emsallem, M. Meyer, N. Idrissi, A. Gizon, and J. Tréherne, Z. Phys. A 320, 695 (1985).

[Pau87] E.S. Paul, S. Shi, C.W. Beausang, D.B. Fossan, R. Ma, W.F. Piel, Jr., N. Xu, and P.K. Weng, Phys. Rev. C 36, 2380 (1987).

[Per63] F.G. Perey, Phys. Rev. 131, 745 (1963).

[Red86] N. Redon, T. Ollivier, R. Béraud, A. Charvet, R. Duffait, A. Emsallem, J. Honkanen, and M. Meyer, Z. Phys. A 325, 127 (1986).

[Rou69] J. T. Routti and S. G. Prussin, Nucl. Instr. and Meth. 72, 125 (1969).

[Sch79] D. Schardt, R. Kirchner, O. Klepper, W Reisdorf, E. Roeckl, P. Tidemand-Petersson, G.T. Ewan, E. Hagberg, B. Jonson, S. Mattsson, and G. Nyman, Nucl. Phys. A326, 65 (1979).

[Sch81] D. Schardt, T. Batsch, R. Kirchner, O. Klepper, W. Kurcewicz, E. Roeckl, and P. Tidemand-Petersson, Nucl. Phys. A368, 153 (1981).

[Sch83] D. Schardt, Computer code DELPA, private communication (1983).

[Sch84a] D. Schardt, P.O. Larsson, R. Kirchner, O. Klepper, V.T. Koslowsky, E. Roeckl, K. Rykaczewski, K. Zuber, N. Roy, P. Kleinheinz, and J. Blomqvist, in *Proceedings of the Seventh International Conference on Atomic Masses and Fundamental Constants, AMCO7*, edited by O. Klepper (Darmstadt, FRG, 1984) p. 222.

[Sch84b] D. Schardt, P.O. Larsson, R. Kirchner, O. Klepper, V.T. Koslowsky, E. Roeckl, K. Rykaczewski, P. Kleinheinz, and K. Zuber, in *Proceedings of the Seventh International Conference on Atomic Masses and Fundamental Constants, AMCO7*, edited by O. Klepper (Darmstadt, FRG, 1984) p. 229.

[Sch87] D. Schardt, R. Barden, R. Kirchner, O. Klepper, A. Plochocki, E. Roeckl, P. Kleinheinz, M. Piiparinen, B. Rubio, K. Zuber, C.F. Liang, P. Paris, A. Huck, G. Walter, G. Marguier, H. Gabelmann, and J. Blomqvist, in Ref. [Tow87] p. 477.

[See75] P.A. Seeger and W.M. Howard, Nucl. Phys. A238, 491 (1975).

[Smi85] P.J. Smith, D.J. Unwin, A. Kirwan, D.J.G. Love, A.H. Nelson, P.J. Nolan, D.M. Todd, and P.J. Twin, J. Phys. G: Nucl. Phys. 11, 1271 (1985).

[Sta87] W. Starzecki, S. Lunardi, F. Soramel, G. de Angelis, J. Styczen, P. Kleinheinz, K. Zuber, R. Julin, W. Meczynski, B. Rubio, A. Facco, F. Scarlassara, W. Urban, H. Güven, M. Morando, A.M. Stefanini, M. Lach, C. Signorini, W. Gast, G. Fortuna, and S. Beghini, Jülich Annual Report, 1986 (1987) p. 24.

[Sty83] J. Styczen, M. Piiparinen, Y. Nagai, P. Kleinheinz, D. Bazzacco, J. Eberth, and J. Blomqvist, Z. Phys. A 312, 149 (1983).

[Tak73] K. Takahashi, M. Yamada and T. Kondoh, At. Data Nucl. Data Tables 12, 101 (1973).

[Tak88] K. Takahashi, private communication (1988).

[Tid85] P. Tidemand-Petersson, R. Kirchner, O. Klepper, E. Roeckl, D. Schardt, A. Plochocki, and J. Zylicz, Nucl. Phys. A437, 342 (1985).

[Tod84] D.M. Todd, R. Aryaeinejad, D.J.G. Love, A.H. Nelson, P.J. Nolan, P.J. Smith, and P.J. Twin, J. Phys. G: Nucl. Phys. 10, 1407 (1984).

[TOI78] *Table of Isotopes, 7th Edition*, edited by C.M. Lederer and V.S. Shirley (John Wiley & Sons, New York, 1978).

[Tot79] K.S. Toth, C.R. Bingham, D.R. Zolnowski, S.E. Cala, H.K. Carter, and D.C. Sousa, Phys. Rev. C 19, 482 (1979).

[Tot82] K.S. Toth, D.M. Moltz, Y.A. Ellis-Akovali, C.R. Bingham, M.D. Cable, R.F. Parry, and J.M. Wouters, Phys. Rev. C 25, 667 (1982).

[Tot84a] K.S. Toth, D.M. Moltz, E.C. Schloemer, M.D. Cable, F.T. Avignone III, and Y.A. Ellis-Akovali, Phys. Rev. C 30, 712 (1984).

[Tot84b] K.S. Toth, D.M. Moltz, E.C. Schloemer, M.D. Cable, F.T. Avignone III, and Y.A. Ellis-Akovali, in *Proceedings of the Seventh International Conference on Atomic Masses and Fundamental Constants, AMCO7*, edited by O. Klepper (Darmstadt, FRG, 1984) p. 237.

[Tot85] K.S. Toth, Y.A. Ellis-Akovali, F.T. Avignone III, R.S. Moore, D.M. Moltz, J.M. Nitschke, P.A. Wilmarth, P.K. Lemmertz, D.C. Sousa, and A.L. Goodman, Phys. Rev. C 32, 342 (1985).

[Tot86] K.S. Toth, Y.A. Ellis-Akovali, J.M. Nitschke, P.A. Wilmarth, P.K. Lemmertz, D.M. Moltz, and F.T. Avignone III, Phys. Lett. 178B, 150 (1986).

[Tot87a] K.S. Toth, D.C. Sousa, J.M. Nitschke, and P.A. Wilmarth, Phys. Rev. C 35, 310 (1987).

[Tot87b] K.S. Toth, D.C. Sousa, J.M. Nitschke, and P.A. Wilmarth, Phys. Rev. C 35, 620 (1987).

[Tot87c] K.S. Toth, J. Gilat, J.M. Nitschke, P.A. Wilmarth, K. Vierinen, and F.T. Avignone III, Phys. Rev. C 36, 826 (1987).

[Tot87d] K.S. Toth, J.M. Nitschke, P.A. Wilmarth, Y.A. Ellis-Akovali, D.C. Sousa, K. Vierinen, D.M. Moltz, J. Gilat, and N.M. Rao, in Ref. [Tow87] p. 718.

[Tot88] K.S. Toth, D.C. Sousa, J.M. Nitschke, and P.A. Wilmarth, Phys. Rev. C 37, 1196 (1988).

[Tow87] *Proceedings of the Fifth International Conference on Nuclei Far From Stability, Rosseau Lake, Ontario, Canada, 1987*, edited by I.S. Towner (AIP Conference Preceedings, New York, 1988).

[Tru84] J.W. Truran, Ann. Rev. Nucl. Sci. 34, 53 (1984).

[Tur87] R. Turcotte, H. Dautet, S.K. Mark, N. de Takacsy, E. Hagberg, V.T. Koslowsky, J.C. Hardy, H. Schmeing, and X.J. Sun, in Ref. [Tow87] p. 473.

[Vie88a] K.S. Vierinen, J.M. Nitschke, P.A. Wilmarth, R.B. Firestone, and J. Gilat, "Decay of Neutron Deficient Eu, Sm, and Pm Isotopes near the Proton Drip Line", to be published.

[Vie88b] K.S. Vierinen, A.A. Shihab-Eldin, J.M. Nitschke, P.A. Wilmarth, R.M. Chasteler, R.B. Firestone, and K.S. Toth, Phys. Rev. C 38, 1509 (1988).

[Wad87a] R. Wadsworth, A. Kirwan, D.J.G. Love, Y-K. Luo, J-Q. Zhong, P.J. Nolan, P.J. Bishop, M.J. Godfrey, R. Hughes, A.N. James, I. Jenkins, S.M. Mullins, J. Simpson, D.J. Thornley, and K.L. Ying, J. Phys. G: Nucl. Phys. 13, L207 (1987).

[Wad87b] R. Wadsworth, J.M. O'Donnell, D.L. Watson, P.J. Nolan, P.J. Bishop, D.J. Thornley, A. Kirwan, and D.J.G. Love, J. Phys. G: Nucl. Phys. 13, 205 (1987).

[Wad88] R. Wadsworth, J.M. O'Donnell, D.L. Watson, P.J. Nolan, A. Kirwan, P.J. Bishop, M.J. Godfrey, D.J. Thornley, and D.J.G. Love, J. Phys. G: Nucl. Phys. 14, 239 (1988).

[Wap87] A.H. Wapstra, G. Audi, and R. Hoekstra, At. Data Nucl. Data Table 39, 281 (1988).

[War75] D. Ward, H. Bertschat, P.A. Butler, P. Colombani, R.M. Diamond, and F.S. Stephens, Phys. Lett. 56B, 139 (1975).

[Wil80] J. Wilson, S.R. Faber, P.J. Daly, I. Ahmad, J. Borggreen, P. Chowdhury, T.L. Khoo, R.D. Lawson, R.K. Smither, and J. Blomqvist, Z. Phys. A 296, 185 (1980).

[Wil85] P.A. Wilmarth, J.M. Nitschke, P.K. Lemmertz, and R.B. Firestone, Z. Phys. A 321, 179 (1985).

[Wil86] P.A. Wilmarth, J.M. Nitschke, R.B. Firestone, and J. Gilat, Z. Phys. A 325, 485 (1986).

[Wil88] P.A. Wilmarth, J.M. Nitschke, K. Vierinen, K.S. Toth, and M. Kortelahti, Z. Phys. A 329, 503 (1988).

[Win72] W. G. Winn, H. H. Gutbrod and M. Blann, Nucl. Phys. A188, 423 (1972).

[Yin86] K.L. Ying, P.J. Bishop, A.N. James, A.J. Kirwan, D.J.G. Love, T.P. Morrison, P.J. Nolan, D.C.B. Watson, K.A. Connell, A.H. Nelson, and J. Simpson, J. Phys. G: Nucl. Phys. 12, L211 (1986).